ON THE MODELING OF THE EFFECTIVE THERMAL CONDUCTIVITY OF PARTICULATE COMPOSITES AND THE INFLUENCE OF BUILDING POROSITY ON THE SHIELDING OF BLAST WAVES

A Thesis

presented to

the Faculty of Engineering

at Notre Dame University-Louaize

In Partial Fulfillment

of the Requirements for the Degree of

Masters of Science in Civil Engineering

by

NANCY DIB

JULY 2022

Notre Dame University - Louaize
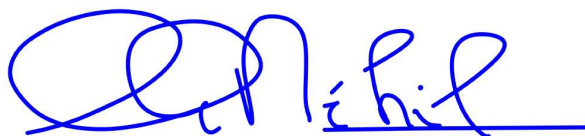
Faculty of Engineering

Department of Civil and Environment Engineering

We hereby approve the thesis of

Nancy Dib

Candidate for the degree of Master of Sciences in Civil Engineering

Signature

_____

Dr. Gérard-Philippe Zéhil   Supervisor, Chair

Signature

Digitally signed by Sam Rigby
DN: cn=Sam Rigby, o, ou,
email=sam.rigby@shef.ac.uk,
c=GB
Date: 2022.06.22 11:06:46
+01'00'

_____

Dr. Samuel Rigby   Committee Member

Signature

_____

Dr. Talal Salem   Committee Member

Acknowledgements

I first wish to thank my advisor Dr. Gérard-Philippe Zéhil for his guidance and support throughout my time as a graduate student at NDU. Dr. Zéhil, thank you for your care, your patience, your encouragement and for getting the best out of me while always responding to my questions, queries and graduate student needs. I have been extremely lucky to have an advisor who cares so much about his students both on the personal and professional levels. You are a role model!

I also wish to express my deepest gratitude to Dr. Samuel Rigby for his careful review of my research proposal and my research work, for his valuable insight and constructive feedback.

I am grateful to Dr. Talal Salem as well for his continued support throughout my stay in the department of Civil and Environmental Engineering, for being part of my thesis committee and for facilitating my access to the department's computer lab.

My gratitude extends to everyone in the Faculty of Engineering who contributed to the enhancement of my graduate student experience at NDU, especially Ms. Jeannette Elias whose kindliness and care made my stay more comfortable, Dr. Sary Malak who shared some of his experience in the industry, Dr. Ghassan Kraidy who let me use his office computer, Dr. Najib Metni for believing in me and supporting my application to the program and Dr. Michel El Hayek for his kind advising during the application process.

My thanks also go to my peers at NDU, especially Ms. Dalia Falah and Mr. Mohamad Kazma, for their friendliness and support.

I finally wish to thank my friends and my family for all their love and encouragement.

Contents

List of Figures

List of Tables

Abstract

The main and overarching objective of this research endeavor is to devise data-driven soft modeling tools that can provide fast, fairly accurate and computationally efficient predictions for: (1) the thermal conductivity of particulate composites (PC), and (2) the level of shielding provided by a porous structure from a high-yield explosion. The computational tools developed in this work constitute cheaper and faster alternatives to the relatively large and cumbersome numerical simulations or experimental testing campaigns that would otherwise be needed to make predictions of comparable accuracy.

Accurate and computationally efficient predictive models for the effective thermal conductivity of composites are needed to accelerate the design of new materials with improved properties and behavior. The predictive capabilities of previously developed models for thermal conductivity of PCs apply to limited ranges of component properties and proportions. Furthermore, existing material models that account for particle contiguity and filler-matrix thermal contact resistance fail to distinguish between those two effects. In the first part of this work, two novel and complementary predictive models for the effective thermal conductivity of two-phase isotropic PCs are derived: (i) a simple yet efficient analytical model for non-contiguous filler particles, and (ii) a generalized semi-analytical model accounting for both filler particle contiguity and thermal resistance at the filler-matrix interface. The latter model is powered by a thermal conduction grid solver that allows the incorporation of an unlimited number of elements and components to match increasingly complex particulate composite material configurations and behaviors. The models proposed match previously published experimental data fairly well. The grid model is further leveraged to relate the effective thermal conductivity to filler particle size and size distribution. It is found that the formation of filler conduction chains is favored by well-graded particle size distributions.

Numerous and complex interactions occur between a blast wave originating from a high-yield explosion and the typical elements of a dense urban topography. Fairly accurate predictions of the blast loads experienced by structures in such context can be only achieved through relatively large, potentially cumbersome and computationally expensive numerical simulations. Although many existing works address certain effects resulting from blast-structure interactions, their scopes are mostly limited to small-scale partially-confined explosions affecting a few buildings or streets. Furthermore, only few studies touch on the effect of building porosity on the propagation of blast waves, while none focuses on the specific influence of a building's porosity on its shielding effect. The second part of this work develops and implements a set of high-cost high-fidelity numerical simulations to explore the influence of building porosity on the shielding effect. A rich manifold of numerical solutions is thus obtained, including the overpressure and the specific impulse over virtual facades shielded by buildings of different porosity, located at various standoff distances from a large explosive charge. A suitable scaling and modeling approaches including regression and machine learning techniques are then applied to the numerical dataset to devise simplified, yet more general data-driven surrogate tools that can provide fast and fairly accurate estimates of the blast wave shielding capacity of porous buildings. Those tools can contribute in guiding design engineers through the process of evaluating blast loads behind porous structures. This study also contributes to furthering the current state of knowledge regarding the propagation of blast waves in and around porous buildings. In general, the shielding effect wanes as the standoff distance to the charge, or the distance behind the shielding structure, increases. Also generally, the lower the building porosity, the longer the path taken by the wave and the more the rise to peak overpressure is delayed. It is also observed for instance that the intensity of a blast wave behind a highly porous structure can in fact increase. This counter-intuitive outcome is attributed to a local channeling of the wave inside the building floors between the parallel slabs and side-walls.

Chapter 1

General introduction

The modeling of physical or biological phenomena, whether occurring naturally or artificially induced – including the behavior of materials and structures subjected to different types of loading in various conditions – is a subject of constant need and interest. Indeed, models are typically developed to replicate such phenomena virtually, at reduced costs and with sufficient accuracy, for the purpose of performing predictions, exploring alternatives, or designing suitable solutions to existing needs, while meeting certain requirements and satisfying constraints, including those resulting from sustainable development goals. An ideal model would hence perform perfectly accurate predictions at no cost, and in zero time. This is not possible, unfortunately, and although the constant progress in information storage and computing technologies, and the resulting increase in computational power and resources available facilitate the development and implementation of more sophisticated modeling approaches, a suitable compromise must always be found between modeling costs and prediction accuracy.

The pursuit of more development while simultaneously reducing its environmental footprint and addressing the consequences of climate change are associated with the constant and pressing need to develop safer and more efficient, resilient, environmental-friendly and sustainable practices, processes, materials, tools, structures, transportation vehicles and systems, etc. The latter clearly relies on design optimization, which often requires generating many forward predictions under varying design parameters. This

highlights the need to develop and constantly improve efficient modeling tools, to make cheaper, faster and more accurate predictions. A prominent approach in pursuing this goal is to resort to the development of simplified modeling techniques, which essentially rely on thoughtful and judicious reductions of model complexity to improve efficiency while maintaining prediction accuracy.

When physical or biological phenomena or behaviors are governed by relatively simple processes, analytical solutions can typically be determined and leveraged to make accurate predictions in limited time. In other cases, approximate analytical solutions can often be derived following suitable simplifications of the underlying processes, such as neglecting certain secondary aspects or dynamics of the problem at hand that would have little impact on its solution. For example, analytical expressions modeling the brittle thermal-cracking behavior of cylindrical and spherical shells encapsulating inclusions were developed by Zéhil (2019) and Zéhil (2020). To this aim, the author considered constant circumferential stresses in the cracked region assuming small crack openings, which led to simple governing differential equations that were solved in closed form. The analytical models proposed matched the actual behavior of the materials, estimated from more cumbersome, significantly costlier and more time consuming high-fidelity numerical simulations, fairly well. In the same vein, Zéhil and Gavin (2013a) proposed two simplified approaches to estimate the rolling resistance of rigid spheres on a viscoelastic material. Both approaches are based on the validated assumption that the contribution of surface friction to the rolling resistance is negligible. In the first approach, the rolling sphere is conceptually divided, along the width of the contact surface assumed perfectly centered and circular, into a set of cylinders whose individual rolling resistances are computed in two dimensions. The total rolling resistance is estimated as the sum of the rolling resistances incurred by each of the cylinders. In the second approach, the rolling resistance is expressed as a function of the Fourier series coefficients of the normal contact stress, neglecting the effect of viscoeslacticity on the latter. The approaches proposed by the authors provide accurate and fast predictions of the rolling resistance as an alternative to the challenging and computationally expensive task of modeling the viscoelasctic

material and solving the contact problem at its interface (Zéhil & Gavin, 2013b, 2013c, 2014a, 2014b).

When the governing equations of the problem at hand are such that deriving an exact or even an approximate analytical solution is impracticable, it is often possible to design high-fidelity numerical models to resolve the governing equations and make accurate predictions. Numerical models of this kind can however be complex, cumbersome and/or computationally intensive, which often motivates resorting to numerical model simplifications, including the removal of secondary or smaller-scale features – such as holes, fillets, rounds, pockets, etc. that can degrade mesh quality and undermine simulation efficiency – while only retaining significant and effective features and constraints. For instance Zhu and Menq (2002) presented an approach to simplify the geometry of a boundary representation (BREP) model by automatically removing unnecessary fillets and rounds. A model's size and/or dimensionality can often be reduced by also leveraging potential symmetries. Local static or adaptive mesh refinement (AMR) techniques can furthermore be applied, including in time-dependent simulations. AMR approaches, in particular, dynamically identify model regions requiring a higher precision discretization and temporarily refine the mesh as needed in such regions, instead of doing so over the whole domain and throughout the entire simulation time. Such approaches can often achieve a higher level of accuracy at a limited computational cost. Berger and Oliger (1984) developed one of the first AMR algorithms for hyperbolic partial differential equations. When applied to one and two dimensional problems, this algorithm resulted in a similar level of accuracy as that of a uniformly refined mesh for one fourth and one sixth of the computational time, respectively.

In many cases however, the leveraging of all possible featural and numerical simplifications proves insufficient to bring the model's performance to a suitable level. This has led researchers to explore alternative soft modeling approaches such as regression and machine learning techniques.

In regression-based modeling, a model of analytical or network form is devised by fitting a set of parameters to experimental data, or alternatively, to data generated using

more sophisticated approaches, such as high-fidelity numerical simulations. The parameters of the regression model are typically determined by minimizing the discrepancy between the model's predictions and the target data. This is typically achieved using suitable optimization techniques, such as gradient descent, back-propagation and Tabu Search (TS) methods. For instance, Dib and Zéhil (2021) proposed both analytical and semi-analytical models to predict the effective thermal conductivity (ETC) of contiguous and non-contiguous particulate composites, with and without thermal contact resistance, based on the properties and proportions of their constituents. The models' parameters were determined by fitting the models to manifolds of high-fidelity numerical solutions or experimental data. The models were deemed accurate over wide ranges of material properties and fractions. Pannell et al. (2019) conducted a set of computational fluid dynamics (CFD) simulations measuring the peak specific impulse generated on plane surfaces located at various distances close-in to a spherical explosive charge. The authors noted that the spatial distribution of the peak specific impulse over the plane surfaces followed a bell-shaped pattern. A non-linear regression technique was thus applied to determine the parameters of a fitted Gaussian function in terms of the scaled distance to the charge. Metaheuristic optimization approaches such as Tabu search (TS) can be used to practically select a combination of analytical expressions (or monomials) that best fits target data. Unlike other local search methods, TS can avoid entrapment in suboptimal regions of the solution space, such as 'flat areas' and local minima, by implementing a set of search rules such as: (i) vetoing previously encountered potential solutions to avoid cycling, (ii) favoring the exploration of promising regions of the search space, and (iii) executing disruptive search measures (e.g. resets) if and when the search is caught in a plateau or a local optimum. For example, Zéhil et al. (2020) followed a TS approach to determine a suitable analytical expression combining monomials selected from a predefined set, for the best prediction of the homogenized elastic behavior of inclusion-modified concrete mixtures from their component properties and proportions. The search was conducted based on data generated using high fidelity finite element simulations accounting for randomness in the spatial distributions of aggregates and inclusions. The TS

model's predictions were compared to those generated by other analytical models of linear, quadratic and exponential forms and by an Artificial Neural Network (ANN), derived by the same authors. All simplified models matched the numerical data fairly well.

Artificial Neural Networks (ANN), Support Vector Regressions (SVR), and Physics Guided Neural Networks (PGNN) are examples of machine learning techniques that are successfully used to model many processes, phenomena and behaviors, including in the various fields of engineering. An ANN is a computational model, inspired by the brain's neural network, consisting of neurons (nodes) connected by weighted links and activation functions. An ANN typically comprises an input layer, an output layer and one or more intermediate (hidden) layers. The number of nodes in the input and output layers is determined by the number of inputs and outputs, respectively, while the number of hidden nodes, the type of activation functions, the weights and the biases are determined through learning and training methods (Awad & Khanna, 2015a). In SVRs the relationship between the inputs and the outputs is represented by a hyperplane characterized by support vectors. The hyperplane is surrounded by an insensitive region, called the ϵ-tube, over which the predictions are not penalized as they lie less than ϵ away from the target data. The optimal hyperplane minimizes the prediction error subject to regularization. The latter is a constraint limiting the model's complexity determined from the magnitude of the hyperplane's parameters (Awad & Khanna, 2015b). Non-linear regression problems can also be addressed using an SVR by transforming the training set of data into a higher dimensional space, known as the kernel space, where the relationships can be represented linearly. As opposed to a classical ANN, a Physics Guided Neural Network (PGNN) typically leverages some preliminary knowledge of the governing physics of a particular phenomenon to improve the model's reliability and robustness, while avoiding the overfitting of small data sets. To this aim, a physics-based loss function is typically added to the learning objective of the neural network to insure that the model's predictions do not only show high accuracy on the target data but also conform to the underlying physics that have generated them.

Machine learning approaches have been used extensively to devise simplified predic-

tive models in different areas of engineering. For instance, Shahmansouri et al. (2021) designed a three-layer ANN to efficiently predict the compressive strength of modified Geopolymer Concrete (GPC) in which the ground granulated blast-furnace slag (GGBS) is partially replaced by silica fume (SF) and natural zeolite (NZ). The ANN, trained on experimental data, takes the concrete age, the NaOH concentration, the contents of SF, NZ and GGBS as inputs, and provides accurate predictions of the compressive strength with a correlation coefficient R of 0.98. Pasolli et al. (2011) used the support vector regression technique to estimate the soil's moisture content based on microwave data acquired through a scatterometer. Their SVR model provided greater estimation accuracy than an ANN, trained on the same set of data, while being three times faster to train. Dennis et al. (2021) trained a five-layer ANN to predict the peak specific impulse resulting from an explosive charge at specific locations in a confined space. The ANN was trained on a set of numerical solutions generated by a validated high-fidelity computational tool. A PGNN was recently developed by R. Zhang et al. (2020) to predict the structural displacement response of buildings to an earthquake, based on the ground's acceleration. The PGNN was trained to minimize the prediction error while conforming to the equations of motion. Li et al. (2021) trained several PGNNs to predict the displacement field of elastic square plates under different loading conditions: (i) in-plane nonuniform stretching, (ii) in-plane uniaxial central-hole tension, (iii) out-of-plane bending under uniform load, and (iv) buckling under in-plane uniaxial compressive load. The authors investigated the use of loss functions incorporating either the residuals of the governing equation and boundary conditions, or the total potential energy in the plate. The PGNNs trained using either of the loss functions provided satisfactory predictions that were fairly close to those generated by high-fidelity finite elements simulations.

To further reduce the size and complexity of simplified models while facilitating and expediting both their design and their training, model order reduction techniques, such as Principal Component Analysis (PCA), Sensitivity Analysis (SA) and Proper Generalized Decomposition (PGD) can be applied, often beforehand, to reduce the dimensionality of the problem. In PCA, the set of input variables is transformed into uncorrelated

'principal' components of decreasing variance. A highest-variance subset of principal components can thus be retained to reduce the number of inputs and hence the model's complexity. The review conducted by Jolliffe and Cadima (2016) provides insights into PCA and its variants. A recent example of practical use of PCA to enhance a soft modeling approach in the field of structural engineering corresponds to the work of Koo et al. (2021). The authors identified eight relevant predictor features of the shear strength of reinforced concrete beams with transverse reinforcement, including web width, shear-span to depth ratio, concrete compressive strength, tensile reinforcement depth, yield strength and ratio, and transverse reinforcement yield strength and ratio. PCA was used to decorrelate the predictor features before feeding all the principal components into an ANN that was trained to predict the shear strength. The ANN performed better than the analytical expressions provided in building codes within the range of the training dataset.

Sensitivity analysis (SA) encompasses a wide variety of techniques whose main objective is to evaluate the relative impact of individual or collective changes in input parameter on a model's outputs. Disregarding those inputs of marginal influence on model predictions can potentially result in significant local or global model order reduction. SA includes 'local' methods concerned in assessing a model's sensitivity to relatively small deterministic changes incurred by the input parameters in the neighborhood of a particular point in the model input space. Conversely, 'global' SA methods essentially rely on the assignment of probabilistic distributions to the input parameters, considered as random variables, to derive the resulting probability distributions of the model's outputs. The review conducted by Borgonovo and Plischke (2016) provides an overview of the most commonly used SA methods.

Proper generalized decomposition (PGD) is an iterative numerical resolution strategy that circumvents the curse of dimensionality by using a separated representation of the unknown solution fields, thus transforming a full-scale multidimensional model into a sequence of simplified models of lower dimensionality whose predictions are more readily determined. This transformation is practically achieved by expressing the quantity of interest as a sum of products of functions, each dependent on one input variable (Chinesta et

al., 2011). The function products (monomials) are determined sequentially, by consecutive 'enrichment' of the global expansion. At every iteration, an additional monomial, i.e. product of single variable enrichment functions, is added to those previously determined in the expansion. The latter is then plugged into the weak form of the original model determined by the full-scale governing partial differential equations, and processed taking into consideration the single-variable dependency of each enrichment function and the boundary conditions, to generate a sequence of simpler integral forms in each enrichment function. The latter are then solved progressively, one at a time, assuming the others are constant, using a greedy algorithm. As opposed to PCA and SA, PGD is an 'a priori' method that does not require any knowledge of the solution. A recent example of practical application of PGD in the modeling of the behavior of construction materials was presented by Ghnatios et al. (2021). The authors used PGD to formulate a simplified model predicting the torque incurred during a vane test performed on a cement paste. The model accounted for the material properties of the cement paste and the rotational speed of the vane as extra (input) coordinates. It was then used iteratively to identify the material properties of a cement paste from experimental vane test results.

The various simplified modeling approaches discussed above are outlined and categorized in Figure 1.1. These can be leveraged individually, or combined, depending on the nature of the problem at hand, to achieve optimal model size and performance.

In this thesis model simplification techniques are implemented in two particular research works: one addressing the generalized modeling of the effective thermal conductivity of particulate composites, and the other pertaining to the prediction of blast loads on structures in an urban environment. Those are presented in Chapters 2 and 3 of the thesis, respectively. Numerical simplification, regression and machine learning techniques are leveraged in both research works, which are introduced briefly herein:

Generalized modeling of the effective thermal conductivity of particulate composites

To accelerate the design of novel, better performing composite materials, simple, reliable and computationally efficient models are needed to predict the effective properties of the projected composite from those of its constituents. Forward model speed and
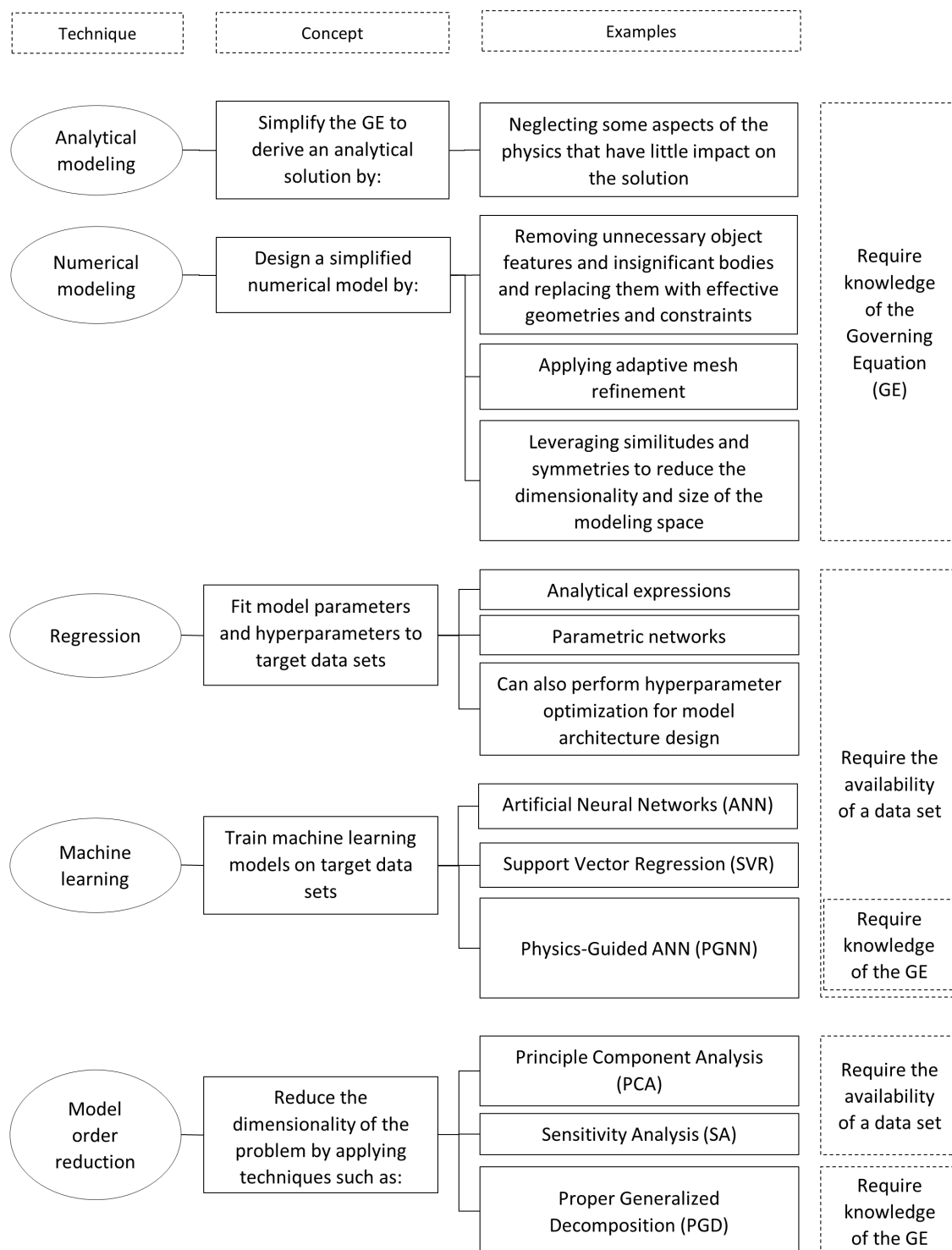
Figure 1.1: Examples and classification of simplified modeling techniques.

accuracy are indeed crucial, especially for the resolution of inverse problems and the implementation of optimization schemes involving recursive forward predictions. Several simplified modeling approaches have been proposed to predict the effective thermal

conductivity (ETC) of particulate composites (PC); however, existing models apply in relatively narrow ranges of constituents properties and proportions, while many fail to account simultaneously for the potential contiguity between inclusion particles and for the thermal resistance across contact interfaces. Novel, simple yet generalized, fairly accurate and computationally efficient predictive tools for the ETC of PC, including analytical, parametric network and machine learning models addressing these shortcomings are devised in Chapter 2. The parametric network models proposed, in particular, rely on judicious simplifying assumptions pertaining to the path followed by the flow of thermal power. Conventional regression techniques are utilized to train the proposed models on either experimental data or over a rich manifold of numerical solutions generated using high-cost high-fidelity finite elements simulations.

Influence of building porosity on the shielding of blast waves

Due to the numerous and complex physical interactions occurring between a blast-wave generated by a high-yield explosion and the various elements of a typical urban topography, including shielding, channeling and confinement effects, reliable predictions of potential blast loads on structures in a city can only be obtained from large numerical models at high computational costs (Remennikov & Rose, 2005; Rose & Smith, 2002; P. D. Smith et al., 2004). To design safe and blast-resilient structures, engineers currently resort to typical design manuals for conservative estimates of blast loads in simple configurations, or to heavy and time-consuming numerical simulations, otherwise. Better alternatives are thus clearly needed for design purposes, but also to enable the quick and reliable assessment of expected damages in the aftermath of an explosion – such as that which occurred in Beirut on August 4, 2020 – to rapidly scale an appropriate relief effort. Research efforts are thus targeted towards providing fast and accurate predictions of the intensity of blast loads in complex setups. Chapter 3 of this thesis contributes, in this context, to a better understanding of the effect of the porosity of structures on their shielding potential, including the development of simplified modeling tools that engineering practitioners can rely on to account for such. A computational study is first designed and conducted using validated numerical tools to evaluate the intensity of a blast wave

behind buildings of different porosity levels, located at various standoff distances from a high-yield explosive charge. Specific model simplification techniques are developed and implemented to improve both the accuracy and the computational efficiency of the numerical simulations run. Data-driven surrogate predictive tools, including analytical and machine learning models are then developed and trained on a previously determined manifold of numerical solutions to produce fast estimates of the intensity of blast waves behind porous structures.

Chapter 2

Generalized modeling of the effective thermal conductivity of particulate composites

2.1 Introduction and background

More efficient and sustainable materials are continuously developed in almost every industry. For instance, in the traditional construction industry, a wide variety of novel inclusion materials are incorporated to concrete mixtures to achieve various objectives, such as reducing weight or permeability, improving sound or thermal insulation, and increasing ductility or strength (e.g. Himo et al., 2019; Khoury et al., 2016; Matar & Zéhil, 2019; Zéhil & Assaad, 2019; Zéhil et al., 2020; Zéhil & Saba, 2018). More generally, lighter, stiffer, stronger, cheaper and more environmental friendly structural composites are constantly sought through both experimental and computational means (e.g. Assaad et al., 2018; Zéhil, 2016, 2019, 2020). In the electronics industry, electrically insulating materials with high thermal conductivity are desired for heat dissipation in packaging (Tekce et al., 2007). With this purpose in mind, Weidenfeller et al. (2004) studied the effect of combining Polypropylene (PP), a good insulator, with magnetite, barite, talc,

copper, strontium ferrite and glass fibers fillers to enhance the thermal conductivity of the composite.

To accelerate the design of novel composites with enhanced thermal properties, it is crucial to evaluate the effective thermal conductivity κ_{eff} of the projected material from that of its components, with sufficient precision and speed. This highlights the need to develop accurate and computationally efficient models for such. One of the first analytical models for the homogenized (electric) conductivity of particulate composites (PC) was introduced by Maxwell (1954). The model is based on the far field theory applied to a dispersed phase in a continuous medium: the electric potential is evaluated at a location far from the center of a sphere placed in a homogenized medium of different resistivity. Because the model relies on the assumption that the distance between inclusion particles is large compared to their radius, it performs best when their volume fraction is small. Levy (1981) later modified the Maxwell-Eucken equation to yield consistent results when applied symmetrically to the components. This was achieved by introducing an additional term, function of the ratio of the thermal conductivities of the constituents. Another commonly used approach to the modeling of the effective thermal conductivity is based on the electric circuits analogy: i.e. phases are arranged in series, in parallel or following a combination of both (e.g. Deissler & Boegli, 1958). Alternatively, models based on the effective medium theory (EMT) consider a random mixture of phases surrounded by a homogeneous medium whose properties are those of the mixture (e.g. Landauer, 1952).

Various models were developed further and applied to the effective thermal conductivity of porous materials, by considering air-filled voids as particulate inclusions. For example, Carson et al. (2005) found that the effective thermal conductivity of an internally porous material is bounded above by the Maxwell model and below by the EMT model, while that of an externally porous material is bounded above by the EMT model and below by the Maxwell model. Gong et al. (2014) also applied the effective medium theory to porous materials, treating all phases as spheres dispersed in a uniform medium of thermal conductivity κ_m. They derived a simple algebraic equation which, when κ_m is varied, identifies with five previous models: the EMT model, the two Maxwell-Eucken

equations and the traditional parallel and series models. J. Wang et al. (2006) among others developed several models for porous materials based on a combination of two or more of the EMT model, the Maxwell-Eucken models and the parallel/series models, selected depending on the physical characteristics of the composite. Ma et al. (2003) designed a model for the effective thermal conductivity of fractal porous media using Ohm's law applied to a self-similar circuit architecture inspired by the Sierpinski carpet. The effect of radiative properties on the effective thermal conductivity of porous materials was also studied both experimentally and numerically. For instance, Fang et al. (2017) considered the contribution of both radiation and thermal contact resistance in the numerical modeling of the effective thermal conductivity of Silica aerogel composites. In particular, it was found that the Rosseland approximation can be used in the case of optically thick aerogel composites. On the other hand, H. Zhang et al. (2017) estimated that, at high temperature, the radiative effects estimated according to the Rosseland equation can contribute to up to 12% of the effective thermal conductivity of polyurethane foams.

Research attempting to develop new models or improve existing models for the homogenized thermal conductivity of particulate composites is still relevant today. M. Chen et al. (2002) assumed the existence of a generic function mapping component properties and volume fractions into the effective thermal conductivity. Based on the "strong indifference principle" (to how the inclusion materials are partitioned) the former was identified to the result of applying the same mapping to the matrix material and small-sized inclusions only, and then recursively to the previously homogenized fraction and the larger inclusions. Driving the above to the limit corresponding to a minute volume fraction of small-sized inclusions ("weak indifference principle") resulted in a simple analytical expression matching a set of direct numerical simulations conducted by the authors, fairly well. J. Wang et al. (2008) proposed a new "structural" model for co-continuous phases (CC), developed using three different approaches: a mathematical derivation based on the Maxwell–Eucken model, a thermal field method and the average field approximation. The CC model can be simply expressed in terms of the traditional series and parallel models. Recently, Rong et al. (2019) trained an artificial neural network (ANN) to predict

the effective thermal conductivity from a set of (2D) cross-section images. The model's accuracy depends on the number of cross-sections retained and their directionality.

Experimental studies have shown that, in some cases, models applying to dispersed inclusions in a continuous phase fail to accurately predict the effective thermal conductivity of the composite (H. Chen et al., 2016; Gao et al., 2015). Such models only depend on the thermal conductivities of the components and their proportions, and hence do not account for a potential thermal resistance at the particle-matrix interface, or possible contact between contiguous particles. Indeed, depending on material properties, shapes, size-distributions, structures and proportions, neighboring filler particles can touch each other and form thermal bridges, significantly influencing the effective thermal conductivity of the composite (Boudenne et al., 2004; H. Chen et al., 2016; Gao et al., 2015; Jin et al., 2015; Krupa & Chodák, 2001; Tekce et al., 2007; W. Zhou et al., 2007b). In such cases, understanding and modeling these effects is also necessary for prediction accuracy. In this vein, Tekce et al. (2007) noted that inclusions shape in copper-filled polyamide composites influences thermal conductivity. Three shapes of copper inclusions were considered: spherical, flat and fibrous. The fiber-filled composites had the highest thermal conductivity followed by those with flat inclusions, while round inclusions resulted in the lowest conductivity. The authors attributed their findings to possible contact between inclusions, arguing that fibers are more likely to interact to form thermal bridges inside the composite. Weidenfeller et al. (2004) explored the influence of magnetite, barite, talc, copper, strontium ferrite and glass fiber fillers on the thermal conductivity of polypropylene. Interestingly, the authors found that the highest effective conductivity was not achieved with the most conductive filler but with talc, which has a moderate thermal conductivity, but a specific microstructure favoring high connectivity between inclusions. Several studies seem to agree on the fact that mixing conductive inclusions of different sizes typically leads to a higher effective thermal conductivity, as small particles fill the gaps between the larger particles, resulting in a higher packing density (Bae et al., 2000; H. Chen et al., 2016; W. Zhou et al., 2007b). However, there is more controversy regarding the potential effect of particle size on the effective conductivity. Krupa and Chodák (2001) followed

by W. Zhou et al. (2007a) found that the effective thermal conductivity decreases with conductive inclusions of increasing size, while Boudenne et al. (2004) and by Gao et al. (2015) noted the opposite.

Lumped parameter models were developed to account for the formation of conductive chains. For instance, Agari and Uno (1986) combined the traditional parallel and series models into a more general expression comprising two lumped parameters, typically fitted to experimental data, to account for: (i) the formation of thermal chains due to particle contiguity, and (ii) the crystallinity of the matrix. Hsu et al. (1995) proposed analytical expressions for the stagnant thermal conductivity of two and three-dimensional spatially-periodic media, also accounting for contact between particles. The authors relied on the electric circuit analogy to partition an elementary volume element (EVE), comprising one inclusion particle with contacting extensions, into a combination of simple parallel and series models. The size of the extensions was considered as a lumped parameter characterizing particle contiguity/contact, and determined by fitting the model to experimental data.

An interfacial thermal resistance occurring at the filler-matrix interface can affect the equivalent thermal conductivity of the composite significantly (e.g. Fang et al., 2017; He et al., 2020; Yang et al., 2014; F. Zhou & Cheng, 2014). Studies have shown that this effect is often dependent on the surface area of the filler particles: smaller particles typically result in a larger interfacial area and hence in more resistance, to the flow of heat. For example, W. Zhou et al. (2007b) studied the effect of the Al_2O_3 filler size on Silicone rubber composites. They observed that larger particle sizes resulted in higher effective thermal conductivities, partially attributing this effect to a smaller interfacial area.

Several analytical models were derived to account for interfacial resistance. Hasselman and Johnson (1987) extended the traditional series model and those previously developed by Lord Rayleigh (1892) and Maxwell (1954) to this aim. Nan et al. (1997) developed another model with interfacial resistance, based on the effective medium theory and taking into consideration the aspect ratio of ellipsoidal particles. The Maxwell model was extended by Xu et al. (2016b) using a potential mean field theory applied to

a continuous matrix and filler while incorporating an interfacial resistance between filler particles. Following a significantly different approach, Xu et al. (2016a) also derived a model similar to that of Agari and Uno (1986), hence providing useful statistical interpretations of its lumped parameters reflecting both the interconnectivity and the interfacial resistance between particles. By analogy to electric circuits, Kim et al. (2009) developed an effective thermal conductivity model that accounts for particle contiguity and interfacial contact resistance. To this aim, contiguous but non-overlapping inclusions of parallelepipedic shape were randomly generated in a 3D matrix. The simulated domain was then meshed with a lattice of cubic thermal resistance elements, while an additional thermal contact resistance was also added at the interface between matrix and particle elements. Recently, Yan et al. (2020) designed and trained an artificial neural network to predict the effective thermal conductivity of UO_2-SiC composites based on their structural characteristics including mean grain area, mean particle area and particle fraction, determined on 2D cross-sections, in addition to interfacial resistance. The model is also used to infer the structural characteristics of a UO_2-SiC composite based on its effective thermal conductivity.

Existing models for the effective thermal conductivity of particulate composites are most accurate in limited ranges of component properties and proportions. For instance, the Maxwell (1954) model is characterized by a good predictive ability when the volume fraction of inclusions is relatively small. Alternatively, the model developed by M. Chen et al. (2002) works best when the thermal conductivity of the dispersed phase is small relative to that of the matrix. Other existing material models accounting for particle contiguity and thermal contact resistance do not make a clear distinction between these two separate effects (Xu et al., 2016b). On another note, it is essential to perform fast forward predictions to accelerate computationally intensive optimization schemes typically used to explore novel composites with improved properties. Hence, there is a persisting need to develop computationally efficient composite material models that are also applicable over wider ranges of relative material properties and proportions.

Two novel and complementary predictive models for the effective thermal conductiv-

ity of two-phase isotropic particulate composites are derived in this chapter: (i) a simple and computationally efficient analytical model for a non-contiguous dispersed phase, and (ii) a more comprehensive semi-analytical model factoring in potential filler particle interactions and a thermal resistance at the interface between phases. Based on the terminology adopted in M. Wang and Pan (2008), these models fall under the categories of 'analytical basic' and 'analytical network' models. Such models are widely preferred in practice for the excellent compromise they can achieve between: (a) simplicity and high computational efficiency on one hand, and (b) satisfactory prediction accuracy on the other hand, including in cases where the discrete phase is randomly distributed (e.g. Khan et al., 2019). The second 'grid' model relies on a generalized thermal conduction grid solver algorithm that can incorporate as many thermal elements and components as necessary to closely replicate the material constitution and hence better match the observed behavior of particulate composites. The material models proposed are initially calibrated to a high-fidelity manifold of numerical solutions constructed from a set of three-dimensional finite element simulations. Their performance is assessed by comparison to other relevant models. A proposed instance of the grid model is also used to match existing experimental data and contribute to filling the knowledge gap regarding the influence of filler particle size on the effective thermal conductivity of composites.

2.2 Summary of relevant existing particulate composites models retained

The performances of the models developed in this chapter will be compared to those of: (i) an artificial neural network (developed in section 2.4), the Maxwell (1954), the Levy (1981) and the M. Chen et al. (2002) analytical models, in the case of non-contiguous inclusion particles, and (ii) the Hsu et al. (1995), the Agari and Uno (1986) and the Xu et al. (2016b) models, otherwise. The Agari and Uno (1986) model can be considered the same as the model developed by Xu et al. (2016a) because of their similar expressions. The Hasselman and Johnson (1987) and the Nan et al. (1997) models are not considered

in this work as these do not account for contact between inclusion particles. Table 2.1 lists the analytical expressions of κ_{eff} for the various models retained. The volume fraction of inclusions is denoted by v_f, while $\lambda = \kappa_I/\kappa_M$ corresponds to the ratio of the thermal conductivity of the inclusion material (index I) to that of the matrix material (index M). The parameter C_1 in the Agari and Uno (1986) model relates to the crystallinity of the matrix, while parameter C_2 accounts for filler particle contiguity. The lumped parameter c in the Hsu et al. (1995) model corresponds to the lateral size of inclusion material extensions representing the contact between particles, while parameter R_e in the Xu et al. (2016b) model designates the interfacial contact resistance.

Model	Equation
Maxwell (1954)	$$\frac{\kappa_{eff}}{\kappa_M} = \frac{2 + \lambda - 2(1-\lambda)v_f}{2 + \lambda + (1-\lambda)v_f}$$
Levy (1981)	$$\frac{\kappa_{eff}}{\kappa_M} = \frac{2 + \lambda - 2(1-\lambda)F}{2 + \lambda + (1-\lambda)F}$$ $$\sigma = (1-\lambda)^2((1+\lambda)^2 + \lambda/2)^{-1}$$ $$F = \frac{1}{2}\left(2/\sigma - 1 + 2v_f - \sqrt{(2/\sigma - 1 + 2v_f)^2 - 8v_f/\sigma} \right)$$
M. Chen et al. (2002)	$$1 = \left((1-v_f)\frac{\kappa_M - \kappa_I}{\kappa_{eff} - \kappa_I} \right)^3 \frac{\kappa_{eff}}{\kappa_M}$$
Agari and Uno (1986)	$$\log(\kappa_{eff}) = v_f C_2 \log(\kappa_I) + (1-v_f)\log(C_1\kappa_M)$$
Hsu et al. (1995)	$$\frac{\kappa_{eff}}{\kappa_M} = 1 - \gamma_a^2 - 2\gamma_c\gamma_a + 2\gamma_c\gamma_a^2 + \gamma_c^2\gamma_a^2\lambda$$ $$+ \frac{\gamma_a^2 - \gamma_c^2\gamma_a^2}{1 - \gamma_a + \gamma_a\lambda^{-1}} + \frac{2(\gamma_c\gamma_a - \gamma_c\gamma_a^2)}{1 - \gamma_c\gamma_a + \gamma_c\gamma_a\lambda^{-1}}$$ $$v_f = \left(1 - 3\gamma_c^2\right)\gamma_a^3 + 3\gamma_c^2\gamma_a^2$$ $$\gamma_c = c/a \text{ and } \gamma_a = a/L$$
Xu et al. (2016b)	$$\kappa_{eff} = \frac{1}{4}(3v_f(\kappa_{se} - \kappa_M) + (2\kappa_M - \kappa_{se})$$ $$+ \sqrt{(3v_f(\kappa_{se} - \kappa_M) + 2\kappa_M - \kappa_{se})^2 + 8\kappa_{se}\kappa_M})$$ $$\frac{1}{\kappa_{se}} = \frac{1}{\kappa_I} + R_e$$

Table 2.1: Review summary of relevant PC models retained.

2.3 Numerical manifold of solutions for non-contiguous particulate composites

This section explores numerically the effective thermal conductivity of a composite material comprising non-contiguous particulate inclusions embedded in a continuous matrix, with no thermal contact resistance at the inclusion-matrix interface. To this aim, a square elementary volume element of the composite containing one inclusion is studied, in conditions of macroscopically unidirectional heat conduction.
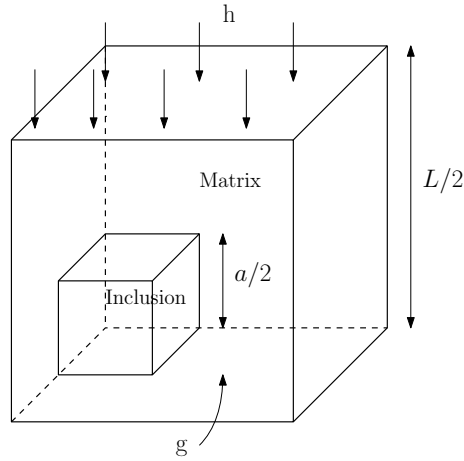
Figure 2.1: Finite element model representing $1/8^{th}$ of the elementary volume element.

Taking advantage of symmetry, a three-dimensional finite elements (FE) model representing $1/8^{th}$ of the elementary volume element (Figure 2.1) is implemented on the commercial software Abaqus. The model consists of a cube of side $L/2$, representing the matrix, containing a cubic inclusion of side $a/2$. The volume fraction of the inclusion, $v_f = (a/L)^3$, is varied by changing the value of a, while L is set to 60 units of length (ul). The domain is meshed using 20-node quadratic hexahedral serendipity elements. The finite element model is used to evaluate the effective thermal conductivity κ_{eff} of the homogenized material, in steady-state, under the following boundary conditions: the lateral walls of the domain are insulated and a constant entering heat flux h is prescribed uniformly across the upper boundary while the lower boundary is maintained at a fixed temperature g. Applying Fourier's law of thermal conduction to the homogenized mate-

rial yields:

$$\kappa_{eff} = \frac{hL}{2\left(\bar{u} - g\right)},$$ (2.1)

where $\bar{u}$ designates the temperature at the upper boundary. The latter is estimated by averaging nodal temperatures across the upper boundary of the model, specifically:

$$\bar{u} = \frac{16}{3L^2} \sum_e j_e \left(\sum_{n \in \eta_d^e} u_n - \frac{1}{4} \sum_{n \in \eta_c^e} u_n \right),$$ (2.2)

where e represents the top-surface element number, j_e the Jacobian of element e, u_n is the temperature at node n, while η_c^e and η_d^e designate corner and edge element node sets, respectively.

Following a thorough convergence analysis, an element size of $1 \times 1 \times 1$ ul^3 is retained across all the domain, for volume fractions $v_f < 0.65$. When $v_f \in [0.65, 0.90]$, the domain representing the matrix becomes narrower, which requires refining its mesh to an element size of $0.5 \times 1 \times 1$ ul^3. For $v_f > 0.90$, the mesh needs to be refined further to $0.1 \times 2 \times 2$ ul^3 in the matrix, while a consistent element size of $2 \times 2 \times 2$ ul^3 is found to be sufficient in the inclusion. In all cases, convergence is verified by a less than 0.04% change in κ_{eff}, relative to a twice coarser mesh.

The finite element model is used as a reference to constitute a manifold of numerical solutions for the effective thermal conductivity of non-contiguous particulate composites: κ_{eff} is determined by running simulations with various ratios $\lambda = \kappa_I/\kappa_M$ and for various inclusion volume fractions $v_f = (a/L)^3$. The dataset constituted is shown in Figure 2.2.

2.4 Artificial neural network model

A set of shallow artificial neural network models (ANN) are fitted to the manifold of numerical solutions developed in section 2.3. Each ANN comprises one input layer taking v_f and $\log(\lambda)$ as inputs, one intermediate layer consisting of a variable number n_h of hidden neurons ($3 \leq n_h \leq 9$), and a single-neuron output layer returning the network's prediction $Y = \log(\kappa_{eff}/\kappa_M)$. A two-component input $\mathbf{X} = \langle v_f, \log(\lambda) \rangle^T$ is first offset
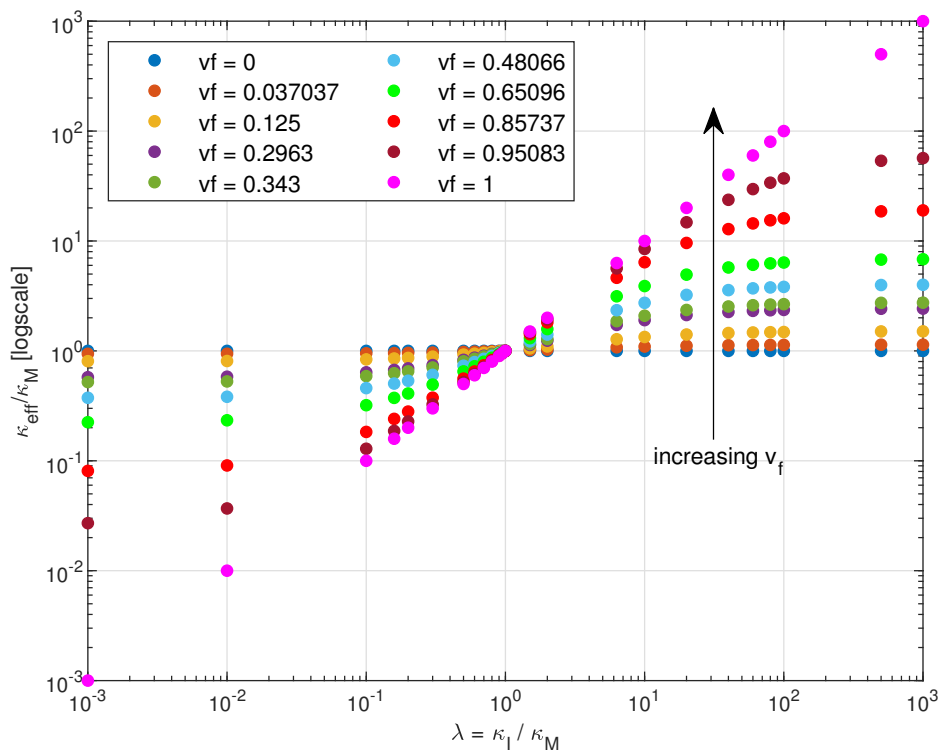
(a) versus λ
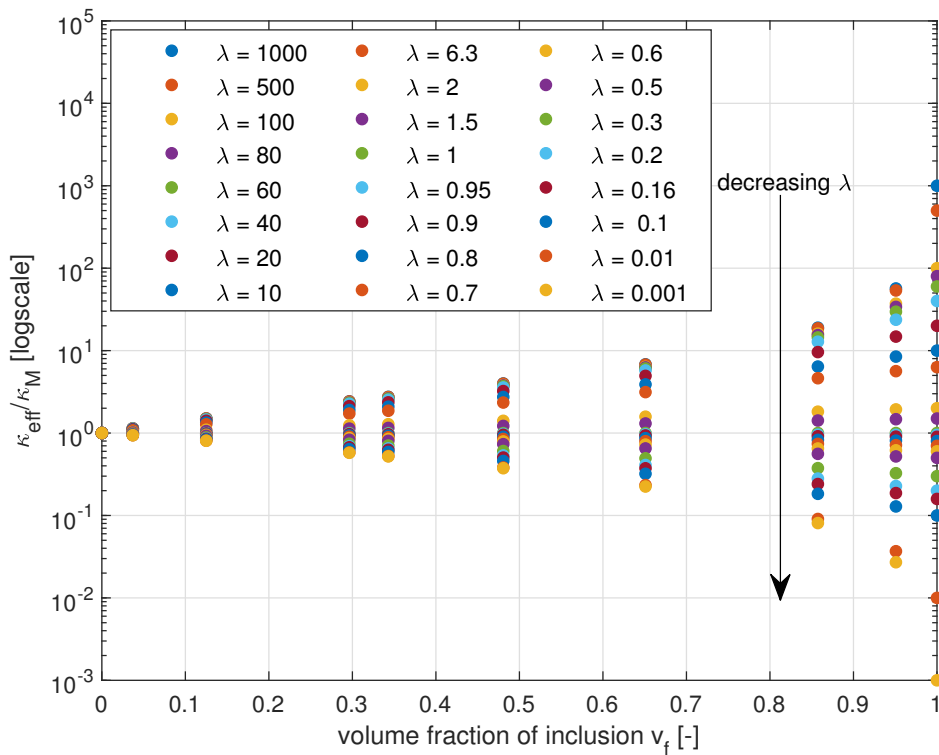
(b) versus v_f

Figure 2.2: The numerical manifold of data points.

and scaled to yield a pre-processed input-vector $\mathbf{X}_1$ whose components are between -1 and 1:

$$\mathbf{X}_1 = 2\frac{\mathbf{X} - \mathbf{X}_{min}}{\mathbf{X}_{max} - \mathbf{X}_{min}} - 1, \tag{2.3}$$

were $\mathbf{X}_{min}$ and $\mathbf{X}_{max}$ contain the minimum and maximum input values, respectively. The hidden layer then transforms $\mathbf{X}_1$ into a column-vector $\mathbf{A}_1$ of size n_h, as follows:

$$\mathbf{A}_1 = h\left(\mathbf{W}_1\mathbf{X}_1 + \mathbf{B}_1\right), \tag{2.4}$$

where the n_h-component column-vector $\mathbf{B}_1$ contains the biases of the hidden neurons, $\mathbf{W}_1$ is a matrix of size $n_h \times 2$ containing the weights applied by each of the hidden neurons to each of the two inputs in $\mathbf{X}_1$ and $h(.)$ is the sigmoid symmetric transfer function given by:

$$h\left(\mathbf{Z}\right) = \frac{2}{1 + e^{-2\mathbf{Z}}} - 1. \tag{2.5}$$

The single-neuron output layer transforms vector $\mathbf{A}_1$ into a scalar output A_2:

$$A_2 = \mathbf{W}_2\mathbf{A}_1 + B_2, \tag{2.6}$$

where the scalar B_2 corresponds to the bias of the output neuron and $\mathbf{W}_2$ is an n_h-component row-vector containing the weights applied by the output neuron to each of the components of $\mathbf{A}_1$. The scalar $A_2 \in [-1, 1]$ is finally post-processed (i.e. reverse offset and scaled) to yield the final scalar output Y:

$$Y = \frac{A_2 + 1}{2}\left(Y_{max} - Y_{min}\right) + Y_{min}, \tag{2.7}$$

where Y_{min} and Y_{max} are the minimum and maximum target values, respectively.

The ANNs' parameters (i.e. weights and biases) are fitted to the data using the Bayesian Regularization algorithm implemented in the commercial software Matlab. To this aim, the data is randomly split into a training set (84%) and a testing set (16%). The training algorithm minimizes the Mean Squared Error (MSE) between the target values

$Y_t^{(i)}$ in the training set and the corresponding ANN model predictions $Y_m^{(i)}$:

$$\text{MSE} = \frac{1}{N_{tr}} \sum_{i=1}^{N_{tr}} \left(Y_t^{(i)} - Y_m^{(i)}\right)^2, \tag{2.8}$$

where N_{tr} is the number of training examples. After training, the MSE is also evaluated on the testing set, while the Mean Relative Error (MRE) is determined on the entire data of size N:

$$\text{MRE}(\%) = 100 \times \frac{1}{N} \sum_{i=1}^{N} \left| \frac{Y_t^{(i)} - Y_m^{(i)}}{Y_t^{(i)}} \right|. \tag{2.9}$$

Hidden neurons n_h	3	4	5	**6**	7	8	9
MSE (training set)	6.10^{-2}	4.10^{-2}	3.10^{-3}	$\mathbf{2.10^{-3}}$	8.10^{-4}	4.10^{-4}	3.10^{-4}
MSE (testing set)	4.10^{-2}	2.10^{-2}	6.10^{-3}	$\mathbf{3.10^{-3}}$	4.10^{-3}	4.10^{-3}	6.10^{-3}
MRE (global set)	15.95%	11.23%	4.14%	**2.86%**	2.30%	1.65%	1.66%

Table 2.2: Model errors for ANNs comprising three to nine hidden neurons.

Table 2.2 summarizes model errors for each of the seven ANN models trained. The MSE on the testing set drops monotonically as the number of hidden nodes is increased from three to six. It then grows as the size of the hidden layer becomes larger and the model starts over-fitting the manifold. Clearly, the ANN comprising six hidden neurons best fits the data with an MRE of 2.86% and it is thus retained here. This choice is supported further by the fact that the model's performance on the training set generalizes best to the testing set, since the MSE has the same order of magnitude on both sets. The 25 fitted parameters of the ANN model retained are as follows:

$$\mathbf{B_1} = \begin{bmatrix} 0.8460 & 13.4619 & 14.9909 & -0.0986 & -0.2562 & -0.6630 \end{bmatrix}^T,$$

$$\mathbf{B_2} = 0.2327,$$

$$\mathbf{W_1} = \begin{bmatrix} -0.0171 & -10.7680 & -12.6451 & 1.3555 & 0.4030 & 0.1595 \\ -1.1126 & -2.8152 & 2.6729 & 3.3934 & 0.6890 & 0.9605 \end{bmatrix}^T,$$

$$\mathbf{W_2} = \begin{bmatrix} 4.5701 & -0.4336 & 0.4199 & 0.0578 & -1.9568 & 6.6388 \end{bmatrix}.$$

2.5 Analytical model for non-contiguous particulate composites

2.5.1 Model derivation

A careful observation of the manifold of numerical solutions generated using the finite element model presented in section 2.3 reveals a clear trend in the relationship between κ_{eff} and v_f, at fixed λ, while a different trend governs the dependency of κ_{eff} on λ, at fixed v_f. The latter is well related by a rational function of the form:

$$\frac{\kappa_{eff}}{\kappa_M} = \frac{(1+b)}{(1+a)} \frac{(\lambda+a)}{(b\lambda+1)},$$

(2.10)

where a and b are primary (internal) parameters depending on v_f. Evaluating a and b at the various volume fractions reveals that these are also well fitted by rational expressions of the form:

$$a = p\frac{1-v_f}{1+v_f/q}, \text{ and}$$

(2.11)

$$b = (1/p)\frac{1-v_f}{1+v_f/r},$$

(2.12)

where p, q and r correspond to three global (external) parameters characterizing the "non-contiguous model" (NC) derived here. Fitting the NC model globally to the numerical manifold yields $p = 2.1443$, $q = 0.3577$ and $r = 2.6009$. Figure 2.3 superimposes the NC model predictions to the numerical manifold. Clearly, the model fits the data excellently.

2.5.2 NC model performance and validation

The performance of the NC model is evaluated by comparison to the ANN (from section 2.4), the Maxwell, the Levy and the Chen et al. models, based on the manifold of data points generated in section 2.3. To this aim, a percent relative error (RE) is calculated
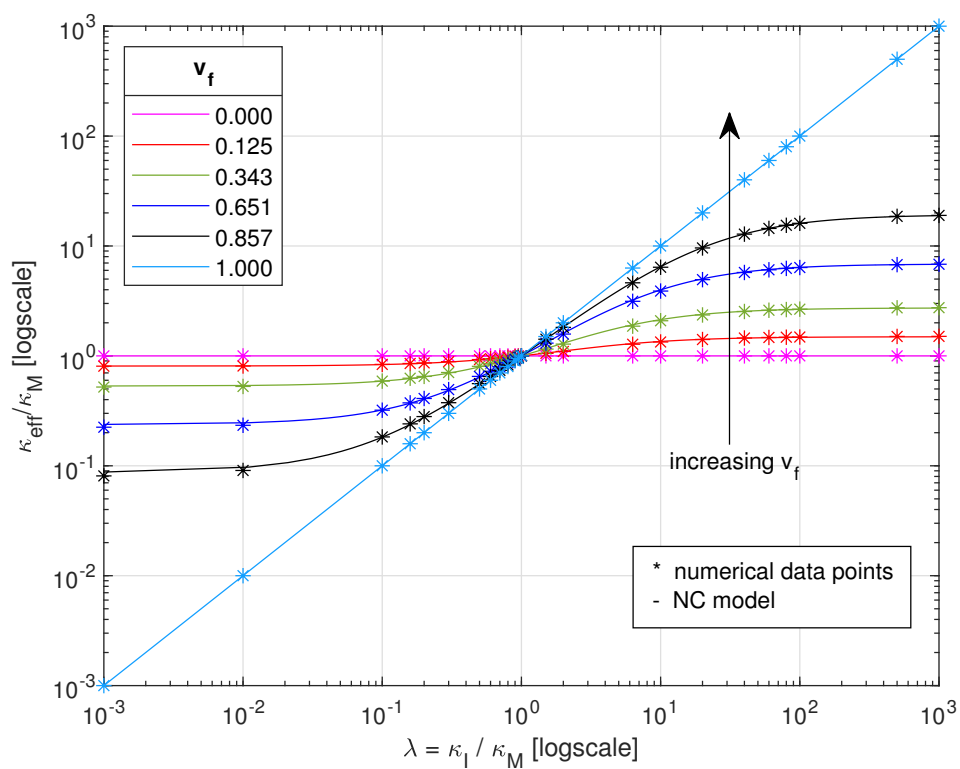
(a) versus λ
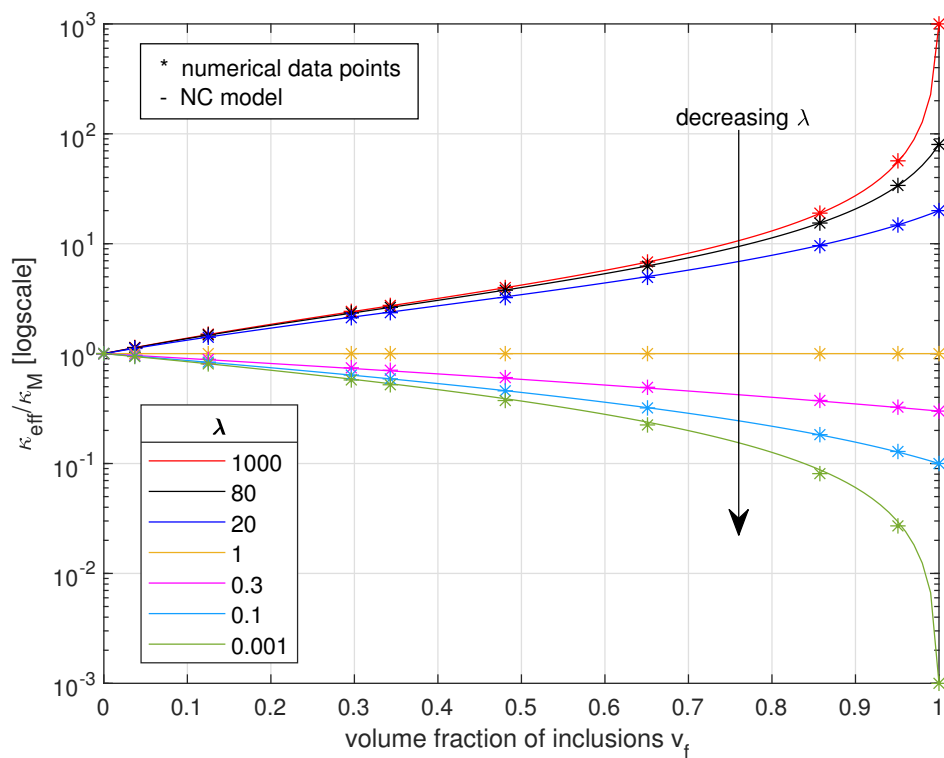
(b) versus v_f

Figure 2.3: NC model predictions superimposed to the numerical manifold of data points.

at each data point for the five models:

$$\text{RE} = 100 \times \frac{Y_t^{(i)} - Y_m^{(i)}}{Y_t^{(i)}}, \tag{2.13}$$

where $Y_t^{(i)}$ and $Y_m^{(i)}$ correspond to the ith target data point and the corresponding model prediction, respectively. Maximal model errors are plotted versus λ in Figure 2.4. Clearly, the NC model outperforms the others. Even though the Chen et al. and the Levy models perform best when λ is close to one, these diverge significantly from the manifold for $\lambda < 0.1$ and $\lambda > 10$. The Maxwell model performs better than the NC model in the limited range corresponding to $0.3 < \lambda < 10$. The performance of the ANN model follows the same trend as that of the NC model but with higher values of the RE. Table 2.3 clarifies further the ranges of validity of the NC model corresponding to various levels of precision. Errors greater than 5% are only seen for $\lambda \leq 0.01$ in the case of $v_f > 0.65$.
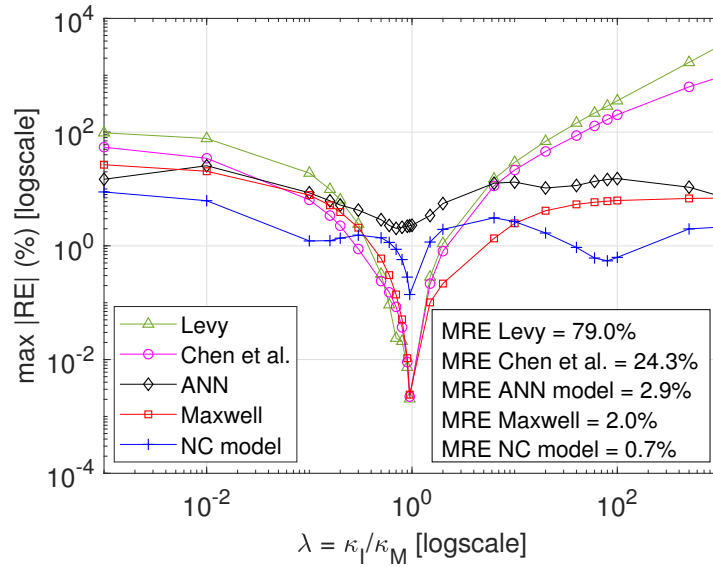
Figure 2.4: NC model's performance compared to the models from Maxwell (1954), Levy (1981), M. Chen et al. (2002) and to the ANN model from section 2.4.

Maximum | RE |	Validity range	
	Lower bound	Upper bound
9%	$\leq 10^{-3}$	$\geq 10^3$
5%	$\sim 2(10^{-2})$	$\geq 10^3$
3%	$\sim 4(10^{-2})$	$\geq 10^3$

Table 2.3: Validity ranges of the NC model corresponding to various precision thresholds.

The MRE (equation 2.9) is also determined to assess the overall performance of the models. The NC model has an MRE of 0.7%, while that of the Maxwell model (2.0%) and the ANN model (2.9%) are almost three and four times larger, respectively. The Chen et al. and the Levy models have significantly larger MREs of 24.3% and 79.0%, respectively. The superior accuracy of the NC model combined to its closed-form analytical simplicity and computational efficiency gives it a clear edge on the other models, including in the resolution of inverse problems.

The Maxwell, the ANN and the NC models are also compared to experimental data from Sundstrom and Lee (1972) corresponding to polystyrene and polyethylene filled with particulate inclusions made from various materials. The models' predictions are superimposed to the experimental data points for glass-filled polystyrene and polyethylene in Figures 2.5(a) and 2.5(b), respectively. In the case of the polystyrene-glass composite ($\lambda = 6.5$), the NC model outperforms the Maxwell and the ANN models significantly, with an MRE of 1.49%, versus 3.89% for the Maxwell model and 4.44% for the ANN model. In the case of polyethylene ($\lambda = 3.0$) the NC model and the Maxwell model perform equally well with MREs of 0.85% and 0.75% respectively, while the ANN model's MRE of 2.97% is roughly four times larger. It is interesting to note that the performance of the models drops with other fillers of increasing thermal conductivity (Sundstrom & Lee, 1972). This can be attributed to the contiguity effect being enhanced further at larger values of λ.

2.6 Thermal conduction grid model (TCG) for contiguous particulate composites

2.6.1 Grid solver algorithm

The size of an elementary volume element (EVE) in a particulate composite of periodic structure corresponds to the spatial period L. By analogy to electric circuits, the EVE is modeled as a combination of elements of homogeneous thermal conductivities, arranged
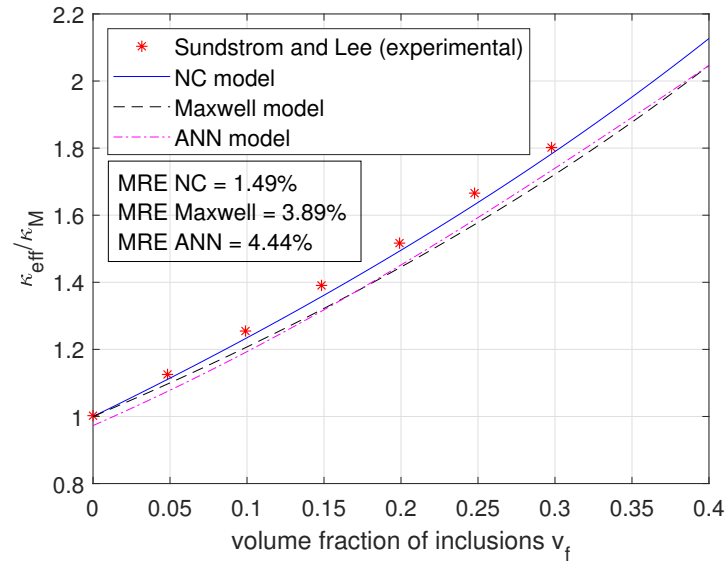
(a) Glass-filled polystyrene $\lambda = 6.5$
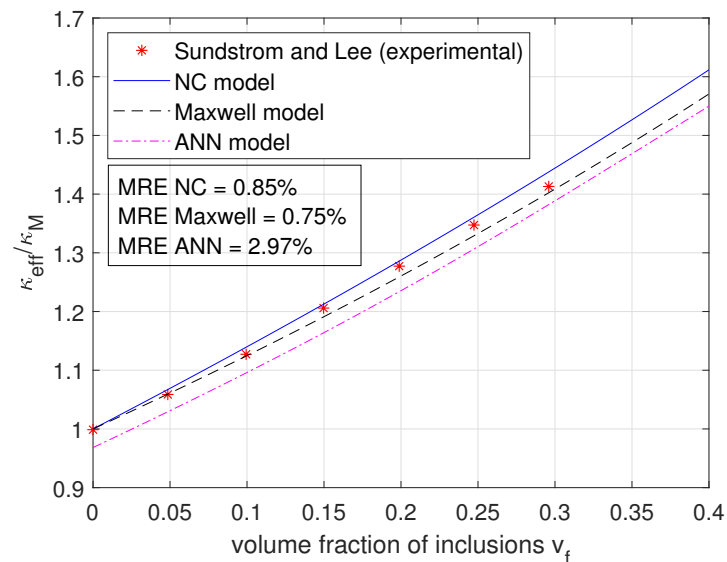
(b) Glass-filled polyethylene $\lambda = 3.0$

Figure 2.5: NC model validation on experimental data for glass-filled composites from Sundstrom and Lee (1972).

in parallel and/or in series, to reproduce an idealized version of the composite's structure. For example, the EVE can be modeled as two blocks in parallel, one corresponding to a matrix element while the other comprises a matrix element and an inclusion element, placed in series. An analytical expression of such model (referred to as the "Ps" model)

is given by:

$$\frac{\kappa_{eff}}{\kappa_M} = \left(1 - v_f^{2/3}\right) + \frac{\lambda v_f^{2/3}}{\left(1 - v_f^{1/3}\right)\lambda + v_f^{1/3}}.$$ (2.14)

Alternatively, the EVE can be modeled as two blocks in series, one corresponding to a matrix element while the other comprises a matrix element and an inclusion element, placed in parallel. This alternative "Sp" model is characterized by:

$$\frac{\kappa_{eff}}{\kappa_M} = \frac{\left(1 - v_f^{2/3}\right) + \lambda v_f^{2/3}}{1 + (\lambda - 1)\left(1 - v_f^{1/3}\right)v_f^{2/3}}.$$ (2.15)

More generally, the EVE can be subdivided into additional blocks and elements of various spatial orientations, depending on the need to better match the effective thermal-conduction behavior of certain multiphase composites, which might also comprise voids and/or contiguous particles. Furthermore, additional elements might be needed to simulate interfacial thermal contact resistances between different phases. This can constitute a thermal-conduction "grid" of significant complexity that is not readily amenable to analytical formulation. A general grid-solver algorithm is hence developed here, to determine the effective thermal conductivity of the composite, regardless of network intricacy and size.

In the thermal-conduction grid model, elements are connected through nodes. Each element e is characterized by its length L_e, its cross-sectional area A_e, its thermal conductivity κ_e, and its delimiting nodes. The flow of thermal power $\hat{q}_e$ through element e is given by:

$$\hat{q}_e = \left(\frac{\kappa_e A_e}{L_e}\right)\Delta T_e,$$ (2.16)

where ΔT_e corresponds to the difference between the temperature at the origin and that at the extremity of the element. The unknown temperatures T_i at nodes i are determined by solving a system of equations expressing the balance of power at the same nodes, i.e.

$$\sum_{e \in \eta_i}\left(\frac{\kappa_e A_e}{L_e}\right)(T_e - T_i) + \hat{q}_i^o = 0,$$ (2.17)

where η_i designates the set of elements connected to node i, T_e is the temperature at the far end of element e, and $\hat{q}_i^o$ is an external source of power prescribed at node i. In the context of the direct 'stiffness' method, the components of the local element 'stiffness' matrix $\boldsymbol{k}^e$ and the global 'force' vector $\boldsymbol{F}$ are given by

$$k_{ab}^e = \left(\frac{\kappa_e A_e}{L_e} \right) (-1)^{a+b}; \quad (a,b) \in \{1,2\}^2, \text{ and} \tag{2.18}$$

$$F_i = \sum_{e \in \eta_i} \left(\frac{\kappa_e A_e}{L_e} \right) g_e + \hat{q}_i^o, \tag{2.19}$$

respectively, where g_e designates the temperature at the far end of element e if this temperature is prescribed, or zero otherwise.

To simulate a macroscopically unidirectional heat conduction process, a constant flow of thermal power is applied to the upper boundary of the $1/8^{th}$ elementary volume element, while the lower boundary is maintained at a fixed temperature. The effective thermal conductivity resulting from the thermal conduction grid model hence writes:

$$\kappa_{eff} = \frac{2\hat{q}}{L \Delta T}, \tag{2.20}$$

where $\hat{q}$ is the prescribed flow of thermal power at the grid's input node and ΔT is the difference between the temperature at the grid's input node, determined by the grid solver, and that prescribed at the grid's output node.

The grid solver algorithm can be used to simulate any three-dimensional network comprising an arbitrary number of discrete thermal conduction elements. Elements of different orientation and material properties can be used to model multiphase composites. Thermal contact resistances at the interfaces between phases can also be represented by special elements characterized by a unit length, a cross-sectional area corresponding to that of the interface and a thermal conductivity set equal to the interfacial thermal contact conductance h_c. Figure 2.6 illustrates the modeling and simulation process on a two-dimensional example of a three-phase contiguous particulate composite comprising two discrete phases (or inclusions) of thermal conductivities κ_{I_1} and κ_{I_2}, and one continuous

phase (or matrix) of thermal conductivity κ_M. The composite is also characterized by a finite thermal contact conductance h_c at the interface between phases I_1 and M.
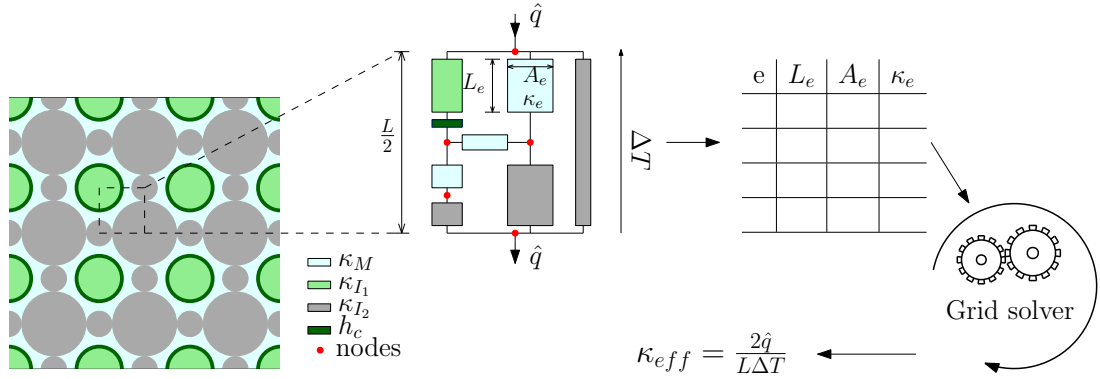
Figure 2.6: Modeling and simulation process using the thermal conduction grid solver.

Two instances of the thermal conduction grid model (TCG) are developed in the following sections: one representing a two-phase particulate composite with non-contiguous inclusions (TCG1), and another addressing the case of contiguous particles with a thermal contact resistance at the filler-matrix interface (TCG2).

2.6.2 Example model for two-phase PC with non-contiguous inclusions (TCG1)

A particular instance "TCG1" of the TCG model is developed here for a two-phase particulate composite with non-contiguous filler particles. The TCG1 model is derived by adding transverse elements to the Ps model (section 2.6.1), to better reproduce transverse heat exchanges between the longitudinal blocks in parallel, as illustrated in Figure 2.7. The length L_e, the cross-sectional area A_e, and the thermal conductivity κ_e of each element e, are listed in Table 2.4. The parameter p tunes the effective depth d of the rectangular cross-sections of the horizontal matrix elements 5, 6, 7 and 8. This depth is expressed as $d = p(L - a)/2$, where a and L correspond to the size of the cubic inclusion and that of the EVE, respectively.

An analytical expression of the TCG1 model is also derived and verified using the grid solver algorithm. The effective thermal conductivity is found to satisfy the following
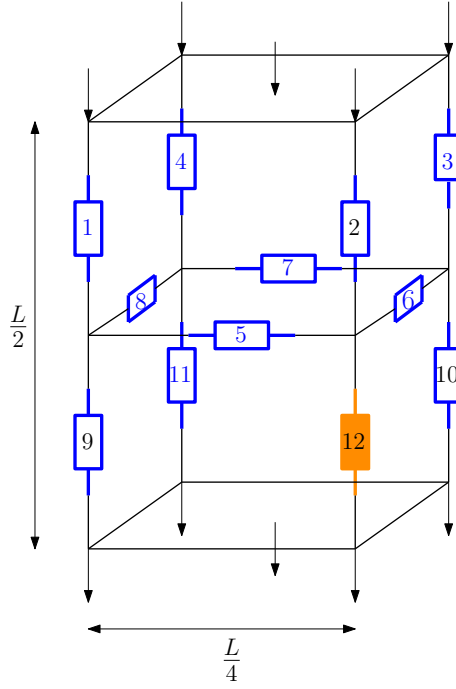
Figure 2.7: The TCG1 model - element 12 models the inclusion material.

expression:

$$\frac{\kappa_{eff}}{\kappa_M} = \frac{G + (1 + 10p - 16p^2)v_f + 2p(4p - 3)v_f^{4/3}}{G + 4p(1 - 6p)v_f + 8p^2(3v_f^{4/3} - v_f^{5/3})}, \tag{2.21}$$

where

$$G = A - Bv_f^{1/3} + Cv_f^{2/3},$$

$$A = (\lambda + 4p)(1 + 2p)/(\lambda - 1),$$

$$B = 2p(3 + 8p)/(\lambda - 1) + 1,$$

$$C = 8\lambda p^2/(\lambda - 1) - 6p,$$

with $\lambda = \kappa_I/\kappa_M$; $v_f = (a/L)^3$ being the volume fraction of the inclusion.

The TCG1 model is calibrated to the manifold of numerical solutions constructed in section 2.3. In this process, the parameter p is found to vary with λ. This dependency is well fitted by the rational function:

$$p = \frac{\alpha\lambda + \beta}{\lambda + (\alpha + \beta - 1)}, \tag{2.22}$$

where $\alpha = 2.6057$ and $\beta = 0.3122$.

Element e	1	2	3	4	5	6
L_e	$\frac{L-a}{2}$	$\frac{L-a}{2}$	$\frac{L-a}{2}$	$\frac{L-a}{2}$	$\frac{L}{4}$	$\frac{L}{4}$
A_e	$\frac{a(L-a)}{4}$	$\frac{a^2}{4}$	$\frac{a(L-a)}{4}$	$\frac{(L-a)^2}{4}$	$p\frac{a(L-a)}{4}$	$p\frac{a(L-a)}{4}$
κ_e	κ_M	κ_M	κ_M	κ_M	κ_M	κ_M

Element e	7	8	9	10	11	12
L_e	$\frac{L}{4}$	$\frac{L}{4}$	$\frac{a}{2}$	$\frac{a}{2}$	$\frac{a}{2}$	$\frac{a}{2}$
A_e	$p\frac{(L-a)^2}{4}$	$p\frac{(L-a)^2}{4}$	$\frac{a(L-a)}{4}$	$\frac{a(L-a)}{4}$	$\frac{(L-a)^2}{4}$	$\frac{a^2}{4}$
κ_e	κ_M	κ_M	κ_M	κ_M	κ_M	κ_I

Table 2.4: TCG1 model elements properties.

Maximum | RE |	Validity range	
	Lower bound	Upper bound
9%	$\sim 5(10^{-2})$	$\geq 10^3$
5%	10^{-1}	50
3%	~ 0.16	~ 12

Table 2.5: Validity ranges of the TCG1 model corresponding to various precision thresholds.
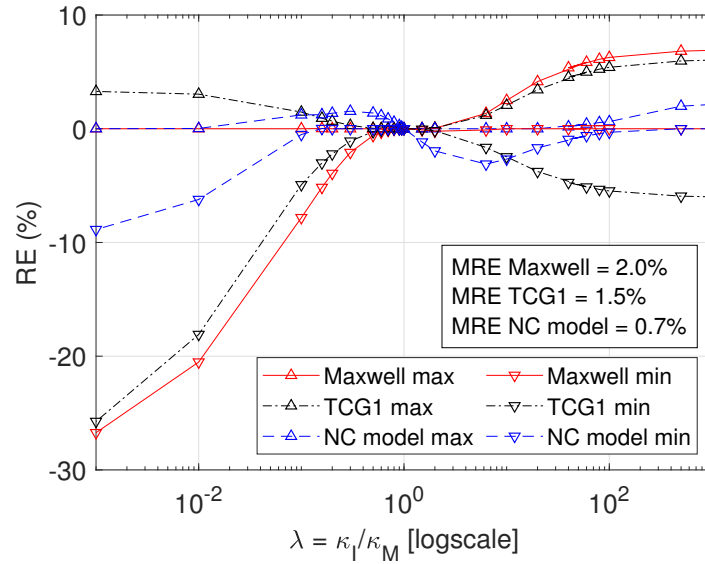
Figure 2.8: Percent relative errors of the TCG1, the Maxwell and the NC models. The error varies with v_f and lies between the extremal values shown, for each model.

The performance of the TCG1 model is measured against that of the Maxwell model and the NC model, over the manifold of numerical solutions. Figure 2.9 compares the predictions of the three models for $\lambda = 0.1$ and $\lambda = 80$. Extremal values of the percent

relative error calculated at each data point for the three models is also shown versus λ in Figure 2.8, while Table 2.5 clarifies further the ranges of validity of the TCG1 model corresponding to various precision thresholds. The NC model performs the best in its field (i.e. non-contiguous PCs) with an MRE of 0.7% followed by 1.5% for the TCG1 model and 2.0% for the Maxwell model. It is interesting to note that, although the parameter p was calibrated to the manifold of numerical data points, it can alternatively be fitted to any set of experimental data.
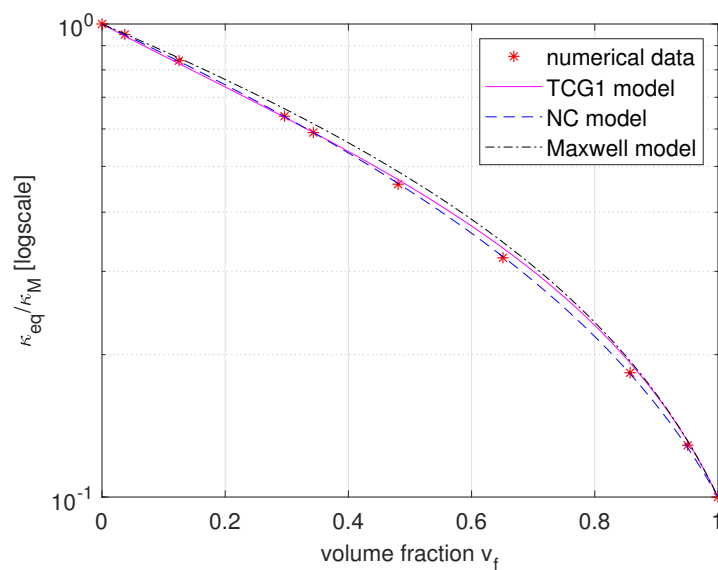
(a) $\lambda = 0.1$
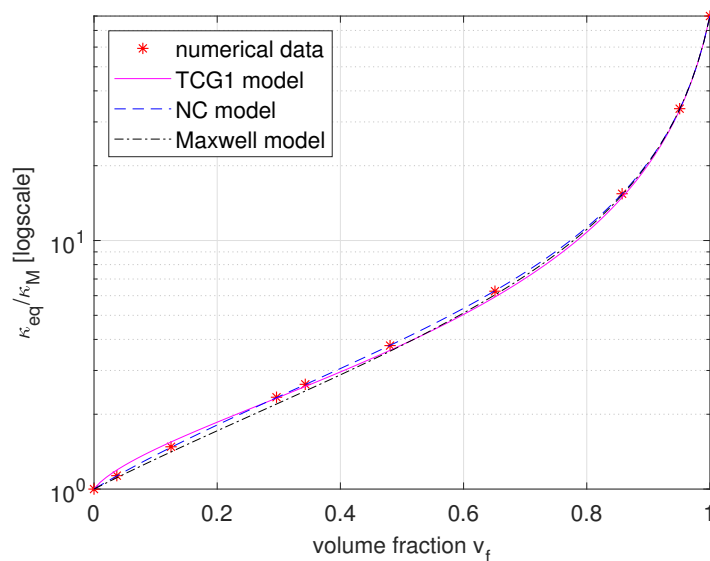
(b) $\lambda = 80$

Figure 2.9: Comparing the TCG1, the Maxwell and the NC models.

2.6.3   Example model for two-phase PC with contiguous inclusions and thermal contact resistance (TCG2)

Design

Another instance (TCG2) of the TCG model is developed here to illustrate the process of designing a thermal conduction grid network accounting for particle contiguity and for thermal contact resistance at the inclusion-matrix interface. Inspired by Hsu et al. (1995), element number 14 is added to the TCG1 model to relate the contact between particles. Both elements 12 and 14 correspond to the inclusion material. Element 14 is characterized by a length $L/2$ and a square cross-section of size $c/2 = (qa)/2$, where $q \leq 1$ is a lumped contact-surface parameter to be fitted to experimental data. The cross-sectional area of element 12 is also adjusted to $(a/2)^2 - (c/2)^2$ to account for that occupied by the additional contact element 14. In three dimensions, the resulting volume fraction of inclusion material in the model writes $v_f|_{\text{model}} = (a^3 + 3(L - a)c^2)/L^3$, which, for $c << a$ is approximately equal to $(a/L)^3$.

The thermal contact resistance at the inclusion-matrix interface is modeled by element 13 standing between inclusion-element 12 on one side and matrix-elements 2, 5 and 6 on the other side. Element 13 is given a unit length, a thermal conductivity h_c, and a cross-sectional area equal to that of element 12. The size of the particle is reflected by the parameter a while that of the EVE is approximated as $L \approx a/v_f^{1/3}$. The TCG2 model is represented in Figure 2.10, while its element properties are listed in Table 2.6.

The flow of heat through a contact interface between two phases is governed by the thermal contact conductance h_c (which depends on the contacting materials only) and by the contact area, characterized here by the parameter $q = c/a$, which is a function of the volume fraction. In particular $v_f = 0 \implies q = 0$, while q is expected to reach a maximum value at the largest packing density. The dependency of q on v_f is hence described by an analytical expression that is consistent with the above, i.e.

$$q = \gamma \left(1 - (1 - v_f)^{1/\delta} \right). \tag{2.23}$$
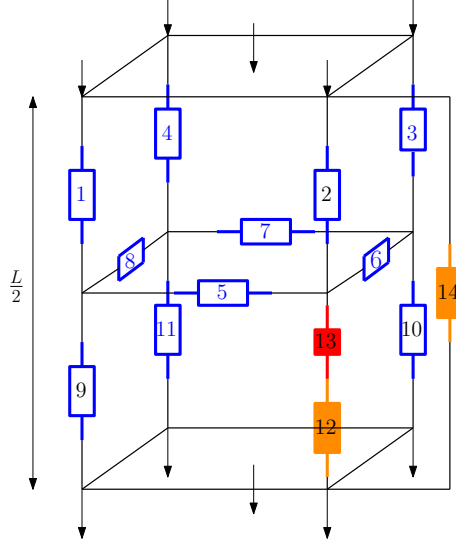
Figure 2.10: The TCG2 model. Elements 12 and 14 model the inclusion material, while element 13 represents a thermal contact conductance.

Element e	1	2	3	4	5	6	7
L_e	$\frac{L-a}{2}$	$\frac{L-a}{2}$	$\frac{L-a}{2}$	$\frac{L-a}{2}$	$\frac{L}{4}$	$\frac{L}{4}$	$\frac{L}{4}$
A_e	$\frac{a(L-a)}{4}$	$\frac{a^2(1-q^2)}{4}$	$\frac{a(L-a)}{4}$	$\frac{(L-a)^2}{4}$	$p\frac{a(L-a)}{4}$	$p\frac{a(L-a)}{4}$	$p\frac{(L-a)^2}{4}$
κ_e	κ_M	κ_M	κ_M	κ_M	κ_M	κ_M	κ_M

Element e	8	9	10	11	12	13	14
L_e	$\frac{L}{4}$	$\frac{a}{2}$	$\frac{a}{2}$	$\frac{a}{2}$	$\frac{a}{2}$	1	$\frac{L}{2}$
A_e	$p\frac{(L-a)^2}{4}$	$\frac{a(L-a)}{4}$	$\frac{a(L-a)}{4}$	$\frac{(L-a)^2}{4}$	$\frac{a^2(1-q^2)}{4}$	$\frac{a^2(1-q^2)}{4}$	$\frac{a^2q^2}{4}$
κ_e	κ_M	κ_M	κ_M	κ_M	κ_I	h_c	κ_I

Table 2.6: TCG2 model elements properties.

TCG2 model validation

The TCG2 model is tested on experimental data reported by Gao et al. (2015) for four mixtures of Al_2O_3-filled silicone-rubber composites, prepared with different size distributions of the filler particles. In the mixtures' designation d_x, the subscript x corresponds to the mean filler-particle size. The thermal conductivities reported are $\kappa_M = 0.15$ W/m.K for silicone rubber and $\kappa_I = 30$ W/m.K for Al_2O_3. Gao et al. noted that, at fixed volume fraction, a higher effective thermal conductivity is achieved by mixtures of higher mean particle-size. The authors fitted both the Agari and Uno (1986) and the Hsu et al. (1995) models to the experimental data. Changes in the parameters representing inter-particle

connectivity in those models drove the interpretation that more contact between inclusion particles is achieved in mixtures with higher mean particle-size.

		p	γ	δ	h_c	MRE %	CoV
Silicone rubber / Al$_2$O$_3$ (Gao et al., 2015)	d_3	0.085	0.261	0.581	$7.50(10^7)$	4.7	0.55
	d_{10}	0.148	0.248	0.450	$7.52(10^7)$	4.6	0.57
	d_{35}	0.398	0.270	0.482	$7.28(10^7)$	3.9	1.05
	d_{75}	2.580	0.320	0.586	$7.38(10^7)$	5.2	1.26
Polypropylene / Al (Boudenne et al., 2004)	A_1	0.007	0.165	0.983	$2.84(10^7)$	8.9	0.81
	A_2	0.007	0.225	1.000	$2.13(10^7)$	4.3	1.98
HDPE / Graphite (Krupa & Chodák, 2001)	EG	2.421	0.089	0.118	$2.50(10^8)$	3.0	1.01
	KS	1.527	0.093	0.083	$2.53(10^8)$	2.4	1.04
Polystyrene / Graphite (Krupa & Chodák, 2001)	EG	1.522	0.144	0.474	$8.34(10^7)$	2.6	1.01
	KS	2.887	0.173	0.471	$8.34(10^7)$	5.5	1.04

Table 2.7: TCG2 model parameters as fitted to experimental data from Gao et al. (2015), Boudenne et al. (2004) and Krupa and Chodák (2001).

Figures 2.11 and 2.12 compare the TCG2 model to relevant existing models over the experimental data reported in Gao et al. (2015). The mean relative errors reveal that globally, the TCG2 model provides a slight improvement over the previous models. The parameter $q = \gamma \left(1 - (1 - v_f)^{1/\delta}\right)$ of the TCG2 model is plotted against the volume fraction v_f in Figure 2.13, as fitted to each of the mixtures d_x in Figures 2.11 and 2.12 . Clearly, q is larger for mixtures presenting a larger mean particle-size. This is consistent with the fact that this lumped parameter relates to the contact area between filler particles. It is also in agreement with the conclusions of the Gao et al. study, although the latter retained a linear dependency of the parameter c (and thus q) on the volume fraction. The parameter h_c has approximately the same value for the four mixtures (Table 2.7), reflecting the thermal conductance at the interface between the silicon rubber and the Al$_2$O$_3$ particles. It is also interesting to note that, with the assumption that $v_f \approx (a/L)^3$, the relative error on the volume fraction is less than 3.9%.
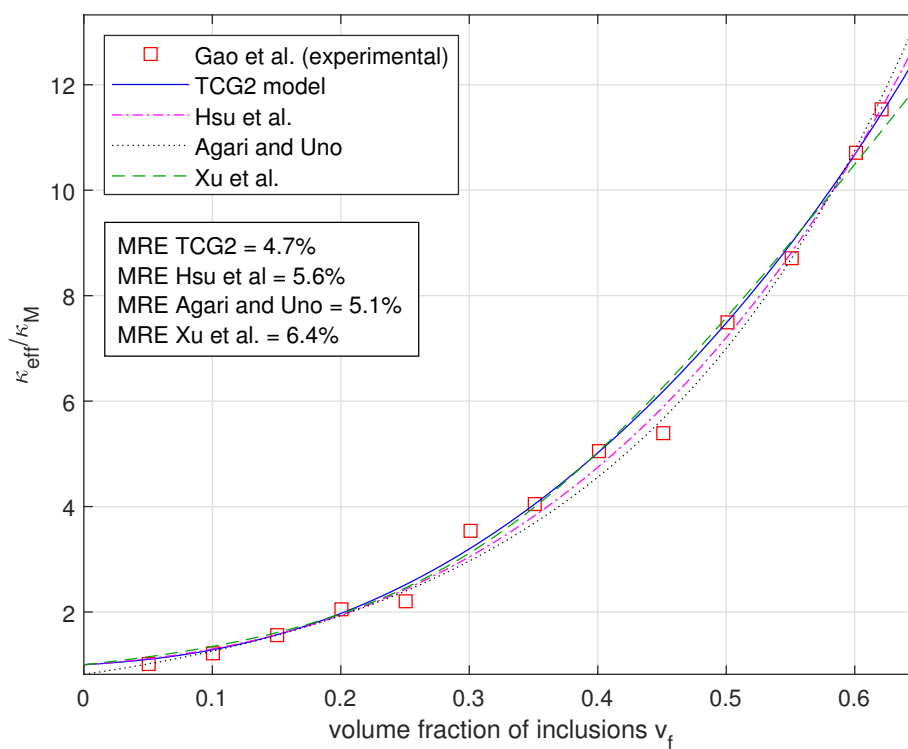
(a) $d = 3\mu$m
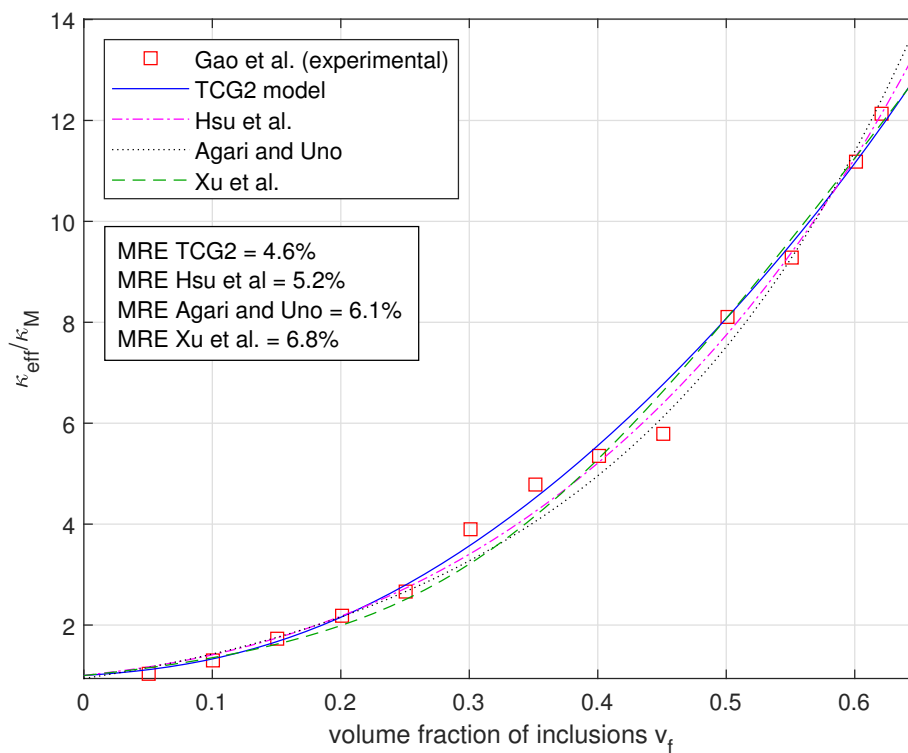
(b) $d = 10\mu$m

Figure 2.11: Models comparison over data for Al$_2$O$_3$-filled silicone-rubber composites (Gao et al., 2015) for $d = 3$ and $d = 10\mu$m .
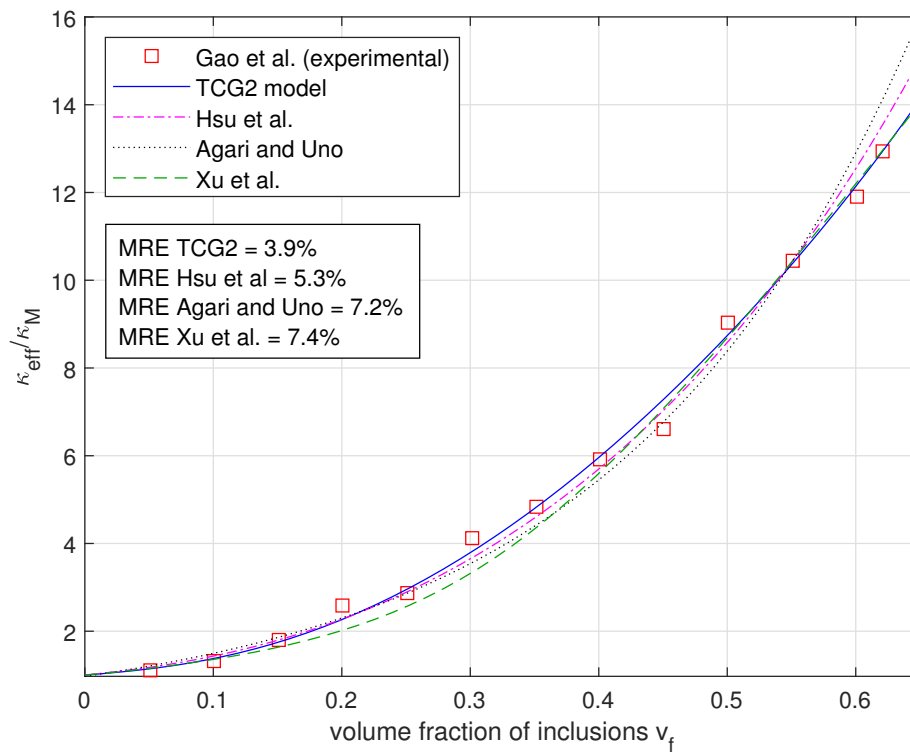
(a) $d = 35\mu\mathrm{m}$
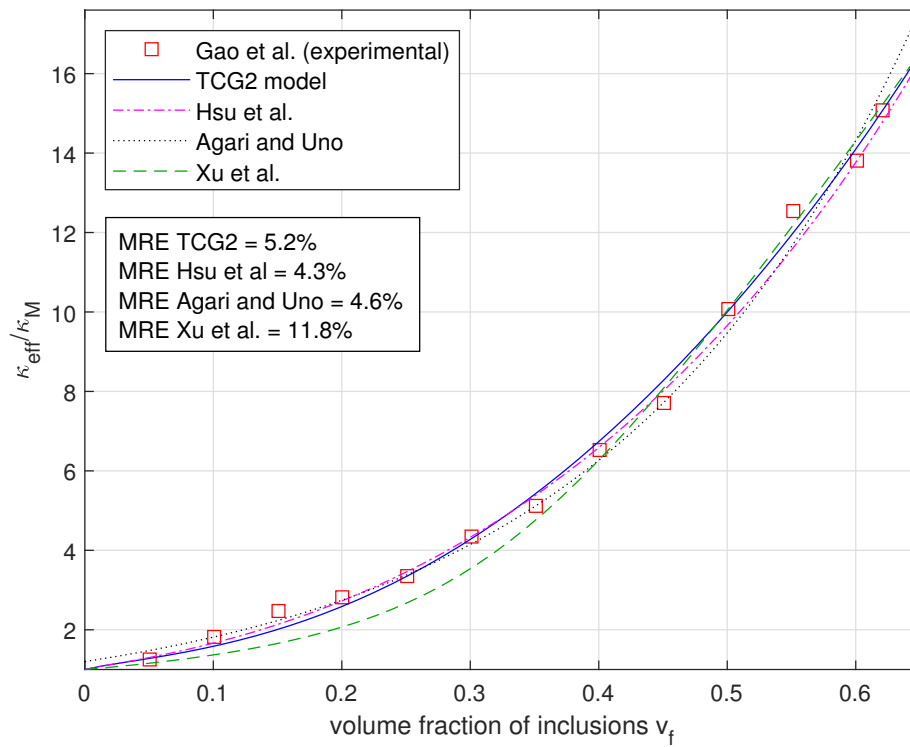
(b) $d = 75\mu\mathrm{m}$

Figure 2.12: Models comparison over data for Al_2O_3-filled silicone-rubber composites (Gao et al., 2015) for $d = 35$ and $d = 75\mu$m.
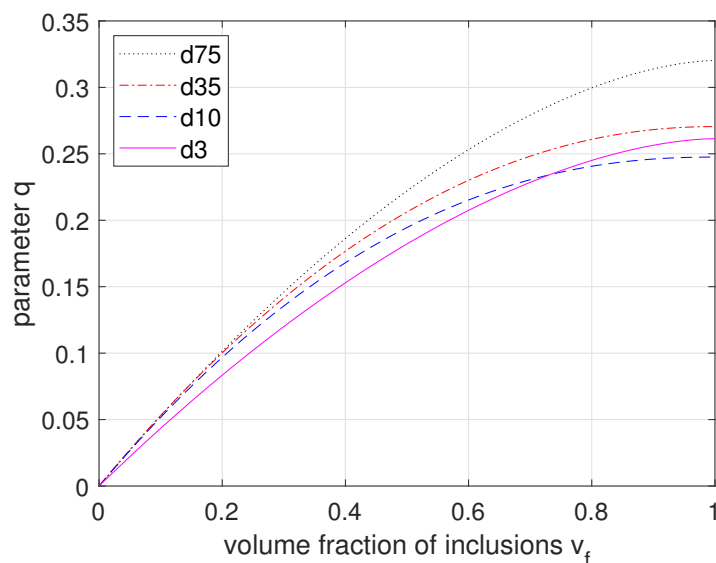
Figure 2.13: Parameter q versus v_f for the data fitted in Figures 2.11 and 2.12.

The TCG2 model is also tested on experimental data reported by Boudenne et al. (2004) and by Krupa and Chodák (2001). Boudenne et al. measured the effective thermal conductivity of Aluminum filled Polypropylene. The thermal conductivities of the components were taken as 237 W/m.K for Aluminum and 0.239 W/m.K for Polypropylene. Two mixtures made with Aluminum particles of type A_1 and A_2, of $8\,\mu$m and $44\,\mu$m mean particle-size respectively, were tested. The effective thermal conductivity was found to be larger for the mixture with the larger particles A_2. Krupa and Chodak tested the effective thermal conductivities of four mixtures made of high density polyethylene (HDPE) or polystyrene (PS), each filled with one of two grades of graphite, KS and EG, of small and large mean particle-size, respectively. The thermal conductivities of HDPE, PS and graphite were taken as 0.436, 0.167, and 208.3 W/m.K, respectively. Contrary to the results reported by Gao et al. and Boudenne et al., the effective thermal conductivity in the study of Krupa and Chodak was found to be larger in mixtures comprising smaller particles. The authors deduced that more conductive chains were formed in this case. The fitted parameter q of the TCG2 model is in agreement with the conclusions of both studies. At constant volume fraction, q is larger for the mixture with Aluminum particles A_2 in the Boudenne et al. study, and for the mixtures with graphite particles KS in the Krupta and Chodak study. The TCG2 model is compared to previous models over both sets of

experimental data in Figures 2.14 and 2.15. Clearly, the TCG2 model fits the data fairly well while showing slight improvement over the previous models. Table 2.7 recapitulates the TCG2 model parameters fitted to the various experimental data in Gao et al. (2015), Boudenne et al. (2004) and Krupa and Chodák (2001). The confidence intervals on h_c are however relatively large due to the small number of available data points and the limited effect of thermal contact resistance for the materials at hand.

On the influence of particle size-distribution

It can be reasonably argued that, within a range of filler particle sizes that are significantly larger than the sizes of individual atoms and molecules, in both the discrete and the continuous phases, the equivalent thermal conductivity measured on a statistically representative volume element of the composite is scale independent. In this context, applying a uniform scaling factor to all filler particles should not influence the thermal conductivity at the macroscale, including the extent to which contacting particles can form conductive or resistive networks. Previous studies have hinted to this argument (e.g. Krupa & Chodák, 2001; Sundstrom & Lee, 1972) while also arguing that particle shape and/or size-distribution can influence the formation of such networks significantly. This line of thought is also supported here by the behavior of parameter q in the TCG2 model. Indeed, for each of the three experimental studies reviewed in this section, at fixed volume fraction, the parameter q takes larger values when the TCG2 model is fitted to mixtures comprising more dispersed particle size-distributions, as reflected by their coefficient of variation (CoV). In this regard, Table 2.7 reveals significant correlations between the global (external) model parameters γ and δ (defining the primary/internal parameter q) and the CoV of the particle size-distribution (based on particle counts). Furthermore, in the case of Gao et al., the parameter δ is found to be correlated with the coefficient of curvature $C_c = D_{30}^2 / (D_{60} D_{10})$ ($x\%$ of the particles, by weight, are finer than D_x), while γ is correlated with the average particle size s. This is documented in Table 2.8 and illustrated in Figure 2.16.
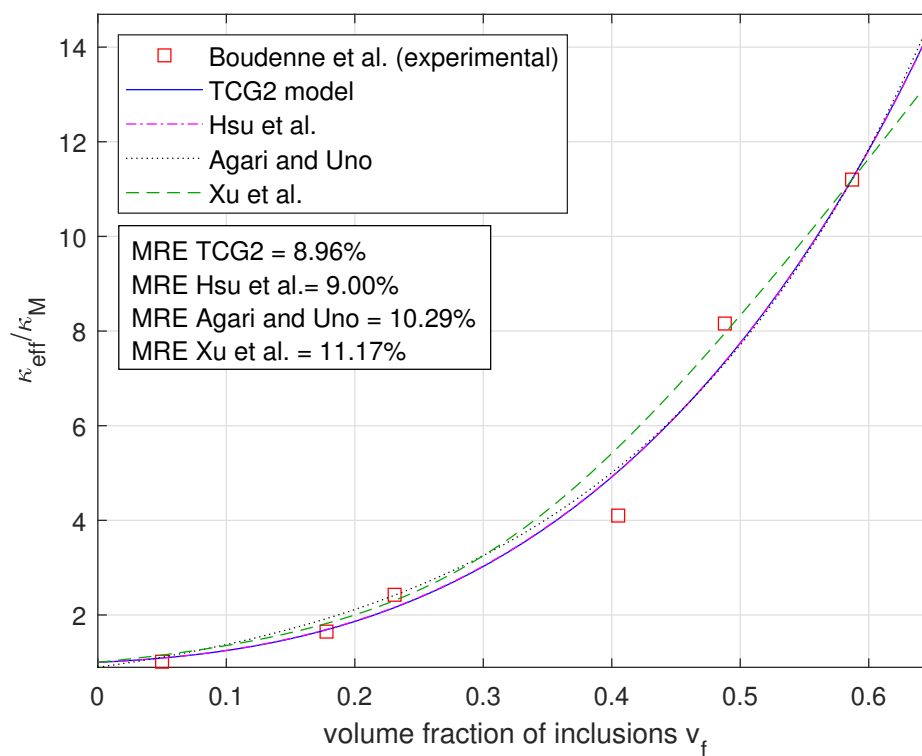
(a) A1 (small Al particles)
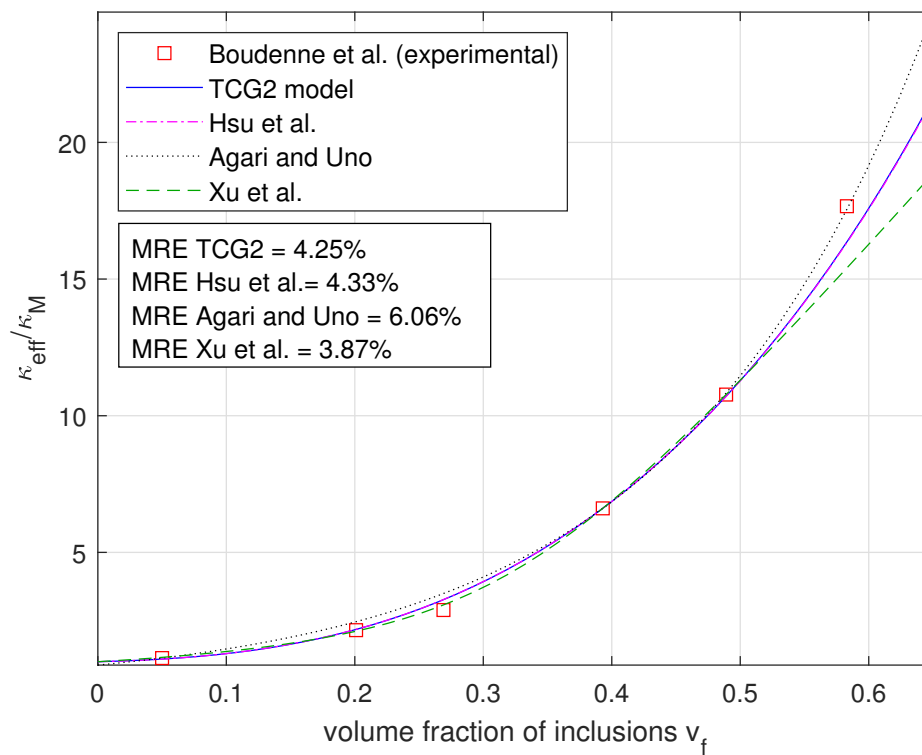
(b) A2 (large Al particles)

Figure 2.14:   Models comparison over data for Aluminum filled Polypropylene (Boudenne et al., 2004).
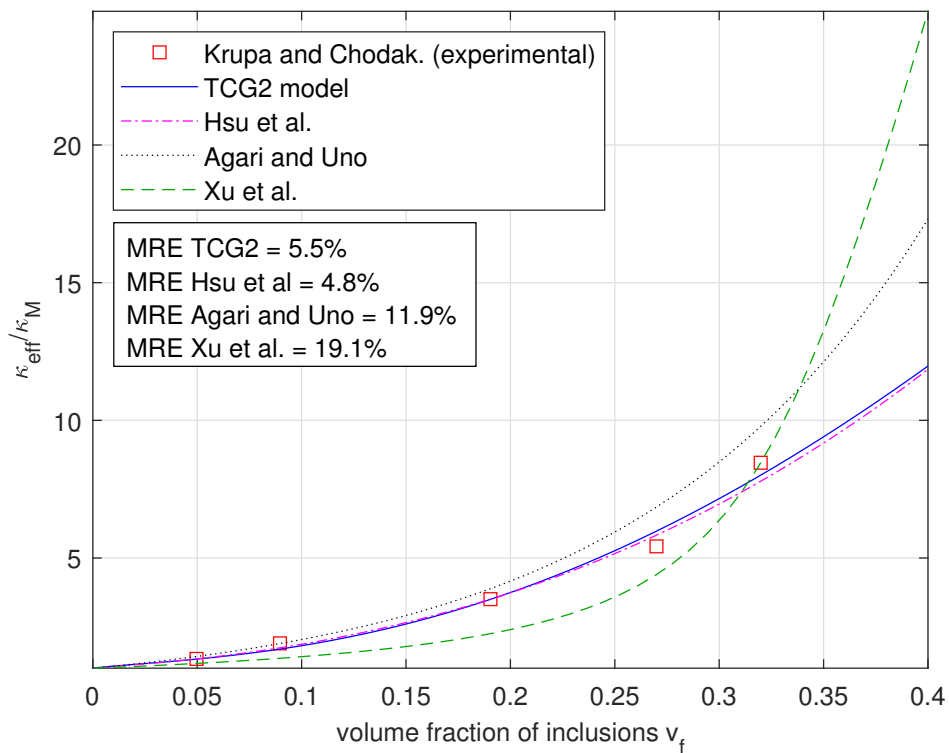
(a) KS (small graphite particles)
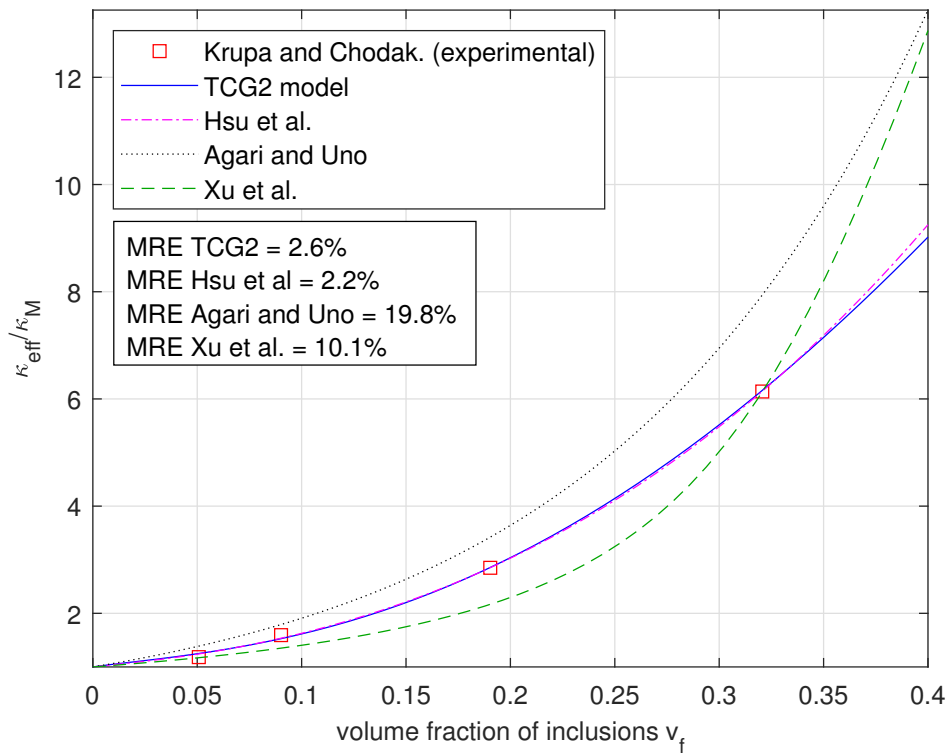
(b) EG (large graphite particles)

Figure 2.15: Models comparison over data for HDPE filled with graphite (Krupa & Chodák, 2001).

	Mix	γ	δ	C_c	mean size s (μm)
	d_3	0.261	0.581	0.8845	3
Gao et al.	d_{10}	0.248	0.450	0.9896	10
(2015)	d_{35}	0.270	0.482	0.9898	35
	d_{75}	0.320	0.586	0.9041	75

Table 2.8: Al$_2$O$_3$ size-distribution properties (Gao et al., 2015) and fitted TCG2 model parameters γ and δ.

(a) δ vs C_c
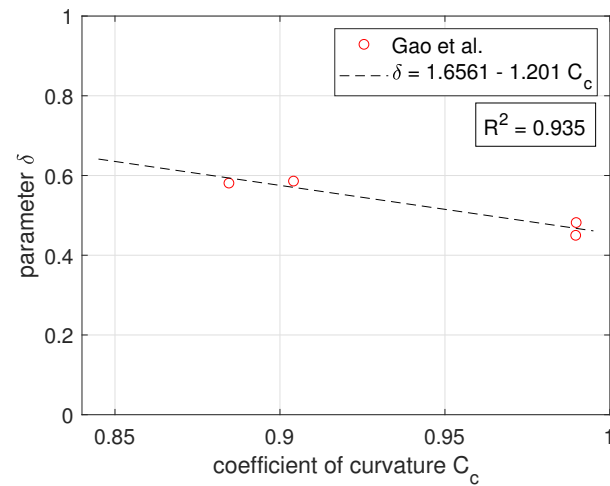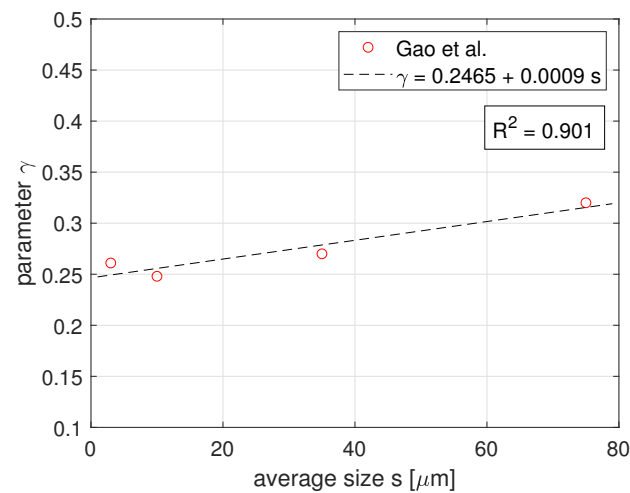
(b) γ vs average particle size

Figure 2.16: Correlation between TCG2 model parameters and size-distribution properties.

2.7 Conclusion

Two new material models were developed in this chapter to better estimate the effective thermal conductivity of two-phase isotropic particulate composites. The first is a simple

and highly efficient analytical model for a non-contiguous dispersed phase. This model matches a manifold of high-fidelity finite element solutions better than other existing models, over a wide range of phase properties and fractions. The model's accuracy was also verified on experimental data from the relevant literature. The second model proposed is powered by a general thermal grid solver. Although slightly more involved, it is also more comprehensive in that: (i) it accounts for particle contiguity and for thermal contact resistance at the filler-matrix interface, by means of clearly distinct model components, and (ii) it can incorporate more, or less, thermal elements and components, arranged as needed, to closely replicate specific material configurations, and hence better match the observed behavior of particulate composites. A particular instance of the grid solver model was developed explicitly, with three lumped parameters, to achieve a fairly close match with both: (i) the manifold of finite element solutions for well-dispersed filler particles and (ii) experimental data from the literature for composites with contiguous filler particles also presenting a thermal contact resistance at the filler-matrix interface. This instance also served to shed more light on the role played by the filler's size distribution in determining the effective thermal conductivity of the composite, as well-graded fillers can more readily form networks of contacting particles.

The new models proposed are fast and accurate over fairly broad validity ranges. With such properties, these are readily applicable in recursive schemes to model the behavior of particulate composites comprising more than two phases. Their high predictive capabilities and computational efficiencies can be leveraged in the field of computational materials science, such as in solving inverse problems to optimize homogenized material properties of interest. In this regard, it is interesting to mention that the models have already been retained in ongoing research works aiming to optimize the properties, size-distributions and volumetric proportions of phase-change material inclusions increasing the effective thermal mass of concrete mixtures, to improve the energy efficiency of future constructions.

Chapter 3

Influence of building porosity on the shielding of blast waves

3.1   Introduction and background

On August 4, 2020, a large quantity of ammonium nitrate exploded at the Beirut port, causing considerable losses at several kilometers from the explosion center, including significant damages to Beirut city structures and infrastructures, and the loss of many human lives. Previously, in 2015, a warehouse exploded in Tianjin's port causing hundreds of deaths and damaging tens of thousands households and businesses nearby (Huang & Zhang, 2015). Producing a quick, yet fairly accurate estimate of the amount of damage due to a large explosion is necessary to build and appropriately scale a suitable emergency response. This, however, requires an understanding of the blast wave propagation and its interactions with the structures in the city. On another note, producing more accurate predictions of blast loads in a complex urban environment is also instrumental to optimize the design of more resilient structures within safer and more sustainable urban layouts.

Empirical models and design manuals, such as the pressure-distance relationship provided by Gilbert F. and Kenneth J. (1985) or by Brode (1955), the graphical data provided by Kingery and Bulmash (1984), the CONWEP software (Hyde, 1988), or the TM5-1300

manual (TM5-1300, 1990) provide estimates of blast load parameters in a free field (un-obstructed) environment. Such estimates however do not apply in denser configurations, due to the interactions of the blast wave with the urban topography: the blast loads can be either enhanced or reduced by channeling, confinement and/or shielding (Gan et al., 2022). The physical complexity of such phenomena is such that the interactions of blast waves with natural or manmade obstacles, such as buildings and other structures, can only be studied experimentally and numerically.

Several numerical and experimental studies were conducted to better understand the confinement, channeling and shielding effects on the propagation of blast waves. For instance, Rose and Smith (2002) studied the effects of street width and buildings height on the enhancement of the positive and negative phase impulses measured along a street. Remennikov and Rose (2005) modeled numerically the detonation of a hemispherical charge at a close distance from two buildings, one shielded by the other. They found that such configuration would reduce the peak reflected overpressure measured at the ground level of the shielded building by a factor of 3.5, and the corresponding positive-phase specific impulse by a factor of 2.5. In another setup, the authors noted that the peak reflected overpressure and specific impulse measured on the facade of a building located at the far end of a T-junction, are greatly enhanced by the channeling of the wave along the incident street. In a more complex setting, P. D. Smith et al. (2004) studied experimentally and numerically the influence of areal density, defined as the ratio of the footprint area occupied by buildings in an array over the total area occupied by the array, on the level of shielding and/or channeling provided by domestic dwellings. It was found that, for the areal densities retained (17.9%, 22.0% and 28.6 %), the presence of an array of buildings between the explosive charge and a target wall reduces the integrated positive impulse along the wall by an average of 10%, while differences due to array density and configuration remained relatively small. This was attributed by the authors to the combined and integrated outcome of the competing effects of shielding and channeling.

In many research works evaluating shielding and channeling effects, including those previously discussed here, the structures interacting with the blast wave are modeled as

rigid blocks without openings, which amounts to neglecting the role of building porosity. Only few studies have accounted for the latter. For instance, P. D. Smith et al. (2003) studied the effect of building porosity, defined as the area of openings relative to the frontal area, on the strength of the blast wave measured along the street and inside the building. The authors found that, for a fixed value of street width, the impulse measured along the street drops as the porosity of the street's buildings increases. The effects of glazing and facade failure on the peak pressure and impulse measured inside the building were also explored. It was found that facade failure resulted in greater average porosity and led to larger overpressure time-histories inside the building. The presence of the rear and side walls did not affect the impulse measured inside the building significantly, due to the delay and attenuation of the reflected waves. Ram et al. (2016) studied the effect of internal geometry and initial conditions (incident pressure and impulse profile) on the specific impulse measured at the back wall of an isolated building. The peak impulse experienced on the back wall was not affected significantly by internal geometry, although the peak pressure and the pressure profile were. The authors related their findings to a previous study revealing a shock-wave filtration process corresponding to significant attenuation of high-frequency pressure fluctuations by stiff porous media (Ram & Sadot, 2015). Drazin (2018) studied the effect of building porosity on the confinement amplification factor in city streets of various widths. It was found that larger porosity reduces the impulse measured along the street, and hence, the confinement effect. Windows' alterations also affected the impulse measured inside the building. For instance, for a fixed porosity level, the impulse measured inside the building dropped as the number of windows increased.

Such outcomes of existing research works reveal the importance of considering building porosity when studying the propagation of blast waves in city streets. However, previous studies focus on the propagation of the blast wave inside the porous buildings and along their street, while these are restricted to relatively small explosive charges as compared to high-yield explosions, such as those that took place in Beirut and Tianjin.

This chapter explores the influence of the porosity of buildings on their shielding

potential, i.e. properties of the blast wave *behind* the building. A set of high-fidelity numerical simulations are designed to better characterize changes in the shielding effect resulting from building porosity variations, for a set of buildings of typical size in Beirut, located at various distances from a simulated high-yield explosion. More specifically, relative changes in incident overpressure and specific impulse averaged over virtual facades located at various distances behind a building are studied in relation to its porosity and to its standoff distance to the explosive charge.

3.2   Methods: setup and modeling approaches

3.2.1   Selection of explosive weight and buildings

To better characterize the influence of building porosity on the shielding of blast waves generated by high-yield explosions, an equivalent charge of 300 tonnes of TNT is retained as an average between various estimates proposed in the literature for the August 4, 2020 Beirut port explosion (Aouad et al., 2021; Dewey, 2021; Rigby et al., 2020; Temsah et al., 2021). For simplicity, the charge is considered hemispherical in shape and the ground fully reflective. A set of buildings of 20 m width, 15 m depth and 16.8 m height, with varying porosity, are placed, each building in isolation, at three standoff distances, 50 m (close-in or near field; 0.7 m/kg$^{\frac{1}{3}}$), 150 m (intermediate field; 2.2 m/kg$^{\frac{1}{3}}$) and 450 m (far field; 6.7 m/kg$^{\frac{1}{3}}$) from the center of the explosive charge. Inspired by the diverse architecture typical to the city of Beirut, four levels of porosity are retained:

(i) "Zero porosity" equivalent to a building with no openings.

(ii) "Low porosity" (Figure 3.1) equivalent to a six-story building characterized by a floor-height of 2.8 m, a facade porosity of 38% and internal walls perpendicular to the flow.

(iii) "Medium porosity" (Figure 3.2) equivalent to a four-story building characterized by a large floor-height of 4.2 m, large arcade openings with a facade porosity of 54% and a few internal columns (no internals walls).

(iv) "High porosity" (Figure 3.3) equivalent to a four-story building characterized by a large floor-height of 4.2 m, fully open front and back facades, and devoid of any internals partitions.

In each case, the peak averaged incident overpressure P_{avg} and averaged specific impulse I_{avg}, determined over virtual facades of 20×16.8 m² located at distances between 5 and 40 meters behind the building, at 5 m spacing, are compared to those measured at the same location in free field, i.e. when the building is not present.

(a) Perspective view.

(b) Facade elevation.

16.8 m

2.2 m

2.4 m

20 m

15 m

5 m

4 m

2 m

(c) Floor plan.
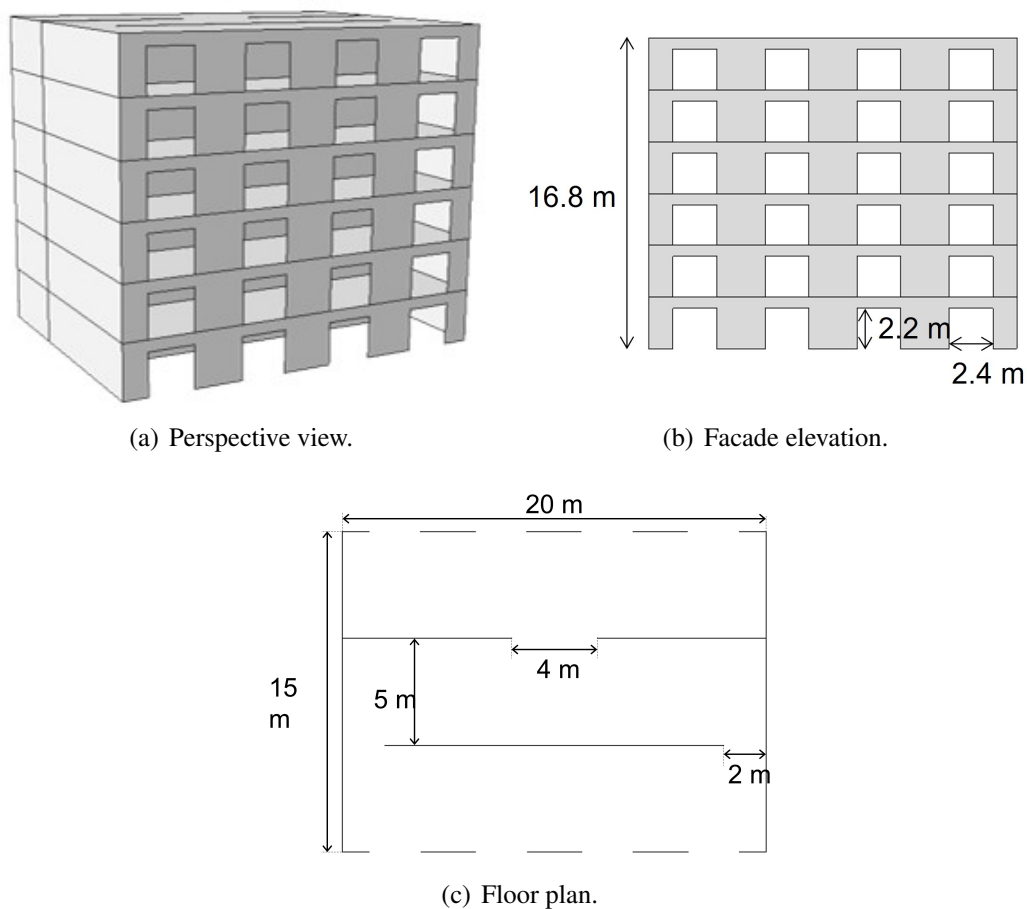
Figure 3.1: The "low-porosity" building model (facade porosity of 38%).

3.2.2 Numerical modeling

CEL model parameters

The buildings and the explosive charge are modeled on the commercial software Abaqus in the various configurations of building porosity and standoff distance retained. The

(a) Perspective view.

(b) Facade elevation.

(c) Floor plan.
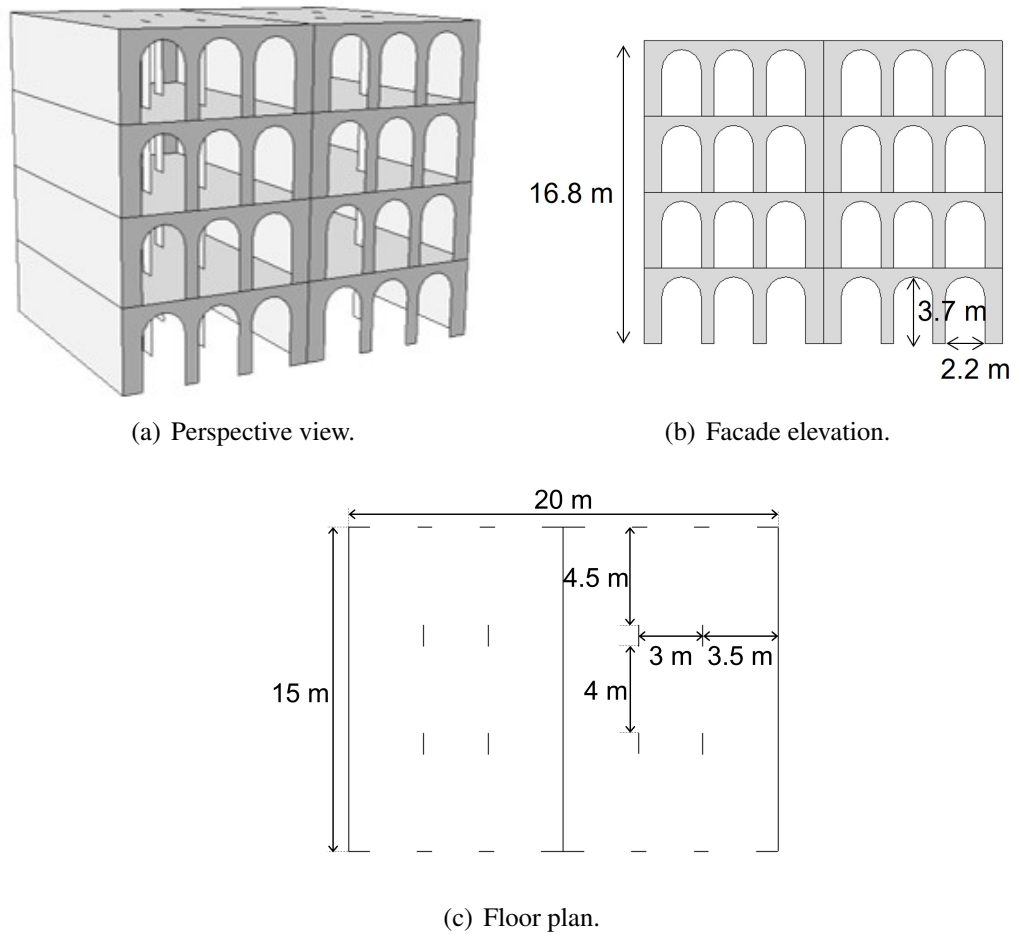
Figure 3.2: The "medium-porosity" building (facade porosity of 54%).
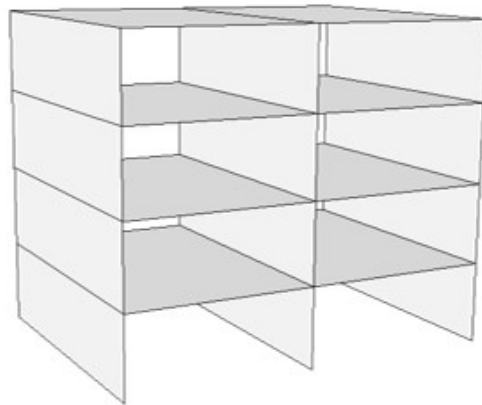
Figure 3.3: The "high-porosity" building (facade porosity of 100%).

buildings are discretized into Lagrangian finite elements, while Eulerian elements are used to model the air, and the explosive charge. Coupled Eulerian-Lagrangian (CEL) simulations are run in each case to characterize the influence of porosity on the shielding of the blast wave generated by the explosive charge. The air is modeled as an ideal gas

ρ_0 [kg/m³]	detonation speed [m/s]	A [GPa]	B [GPa]	ω	R_1	R_2	E_m [J/Kg]
1630	7070	454.86	10.119	0.25	4.5	1.5	4.779 E6

Table 3.1: The JWL parameters retained for the TNT charge (Giam et al., 2020).

whose pressure is governed by the behavioral law:

$$P = \rho_{air} RT, \tag{3.1}$$

where ρ_{air} is the density of air, R is the specific gas constant, and T is the temperature. The internal energy per unit mass e is given by:

$$e = C_v T = \frac{C_p}{\gamma} T, \tag{3.2}$$

where C_v and C_p are the specific heat at constant volume and constant pressure, respectively, and $\gamma = 1.4$. The standard properties of air are assumed as initial conditions, with $\rho_{air} = 1.2256$ kg/m³, $R = 287.05$, $P = 101,325$ Pa, and $C_p = 1$ kJ/kg/K. Because peak building displacements and velocities relative to air during the positive phase of the blast wave are small, the fluid-structure interaction can be neglected and the building can be considered as perfectly rigid (Kambouchev et al., 2007; Subramaniam et al., 2009). The TNT charge will be modeled in Abaqus using the Jones-Wilkins-Lee (JWL) equation of state relating the adiabatic expansion of detonation products:

$$P = A \left(1 - \frac{\omega \rho}{R_1 \rho_0} \right) e^{-R_1 \frac{\rho_0}{\rho}} + B \left(1 - \frac{\omega \rho}{R_2 \rho_0} \right) e^{-R_2 \frac{\rho_0}{\rho}} + \omega \rho E_m, \tag{3.3}$$

where ρ is the density of the detonation product and the parameters A, B, R_1, R_2, ω, E_m, and ρ_0 are user defined constants. This behavioral law was developed by Lee et al. (1968) and validated by comparison to experimental data. The parameters retained to model the explosive charge in the proposed work are listed in Table 3.1. This choice relies on a study conducted by Giam et al. (2020), to best match the CONWEP predictions at various standoff distances from the charge.

Material parameters and modeling approach validation

The JWL parameters retained are further validated on experimental data gathered by Tyas et al. (2011) for a hemispherical charge equivalent to 0.3 kg of TNT [1] detonated four meters away from a plain concrete block of $0.71 \times 0.675 \times 1.93$ m^3 (Figure 3.4).
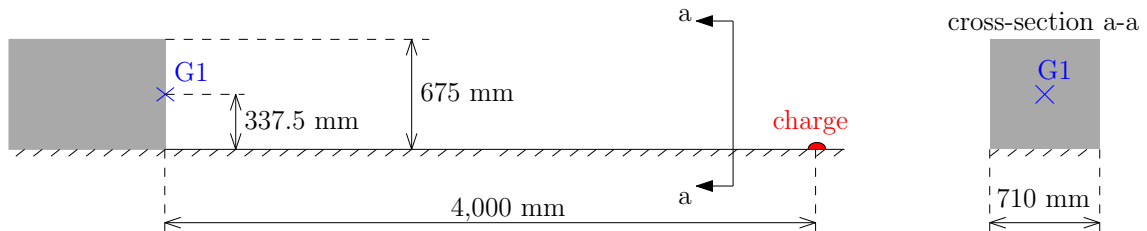
Figure 3.4: Experimental setup of Tyas et al. (2011).
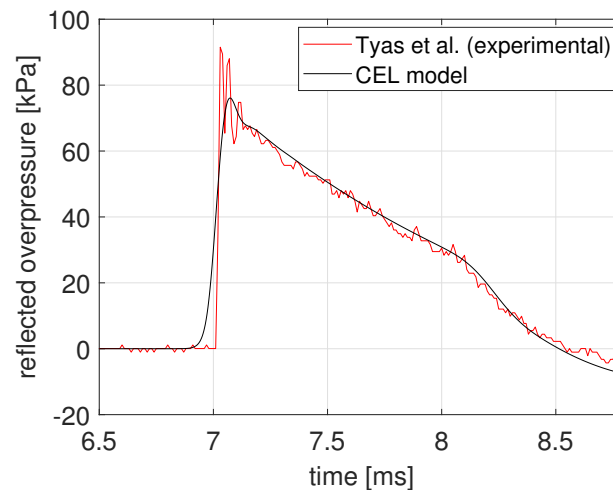
Figure 3.5: History of the reflected pressure at point G1 - numerical results superimposed to the experimental measurements.

The standoff corresponds to a scaled distance $Z = 6$ m/kg$^{\frac{1}{3}}$. Using symmetry, only one-half of the domain and one-quarter of the charge are modeled. A domain size of $1.2 \times 1.6 \times 5$ m^3, used to represent air, is meshed using 1 cm eight-node linear Eulerian brick elements. The concrete block is modeled using zero velocity boundary conditions (BC) in the directions normal to its external surfaces, which are furthermore set as no-inflow/outflow Eulerian boundaries. The same is applied on the surfaces representing the ground and on the surfaces of symmetry. 'Free' inflow and 'equilibrium' outflow Eulerian boundary conditions are prescribed over the remaining three surfaces. The 'equilibrium'

---

[1] 0.25 kg of PE4 assuming a TNT conversion factor of 1.2 in the far field (Rigby & Sielicki, 2015)

outflow boundary condition in Abaqus is used to represent the surface of an unbounded domain: it reduces spurious reflections by assuming that the stress is zero-order continuous across the element faces on the boundary (M. Smith, 2009). The reflected pressure-time history extracted from the numerical model at point G1, located at the center of the frontal surface of the block, is time shifted to align with the arrival time of the experimental blast wave and is superimposed to the experimental data in Figure 3.5. The numerical results are a close match to the experimental measurements, thus validating the modeling approach retained, including the JWL material model parameters.

3.2.3 Model size reduction at large standoff distances

To reduce the model's size and computational cost in the intermediate and far fields, the explosive charge is replaced by a velocity boundary condition, prescribed over a spherical boundary set closer to the building. The velocity-time profile prescribed at this input boundary is extracted from a separate free-air wave-propagation model in 1D, where the charge is represented explicitly using the JWL material law. The 1D wave-propagation model relies on spherical symmetry to represent an explosive charge of 600 tonnes of TNT - i.e. double the surface charge considering the ground as fully reflective (USDOE, 1980) - detonating in one sector of free air. The domain is meshed using a single row of hexahedral elements of size $D_e/1000$ in the radial direction, where D_e is the distance from the element to the center of the charge. Mesh convergence is confirmed by comparing the velocity measured at 110 m from the detonation point to that obtained using a larger element size of $D_e/500$ (Figure 3.6). The mesh size retained also aligns with that prescribed by Shin et al. (2015) and corresponding to the standoff distance divided by 500.

To verify the accuracy of this approach, the velocity-time profile extracted from the 1D wave-propagation model at a distance $L = 110$ m from the charge is prescribed over the input boundary of a reduced 1D model from which the part corresponding to a distance of less than L is removed (Figure 3.7). The overpressure measured at $L + \Delta L = 150$ m in the reduced 1D model is compared to that extracted from the original model, at the same location in Figure 3.8(a). The outcomes of the same procedure applied for $L = 390$ m

and $L + \Delta L$ = 450 m are shown in Figure 3.8(b). The pressure histories of the reduced 1D model match those of the original 1D model, which validates the modeling approach retained here.
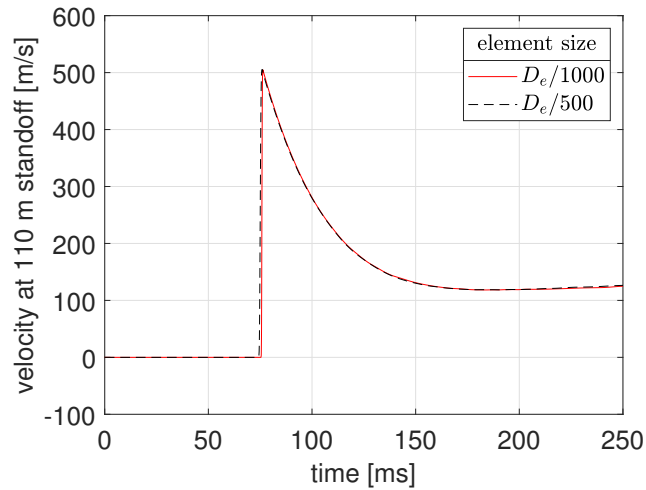
Figure 3.6: 1D free-air wave-propagation model mesh convergence.
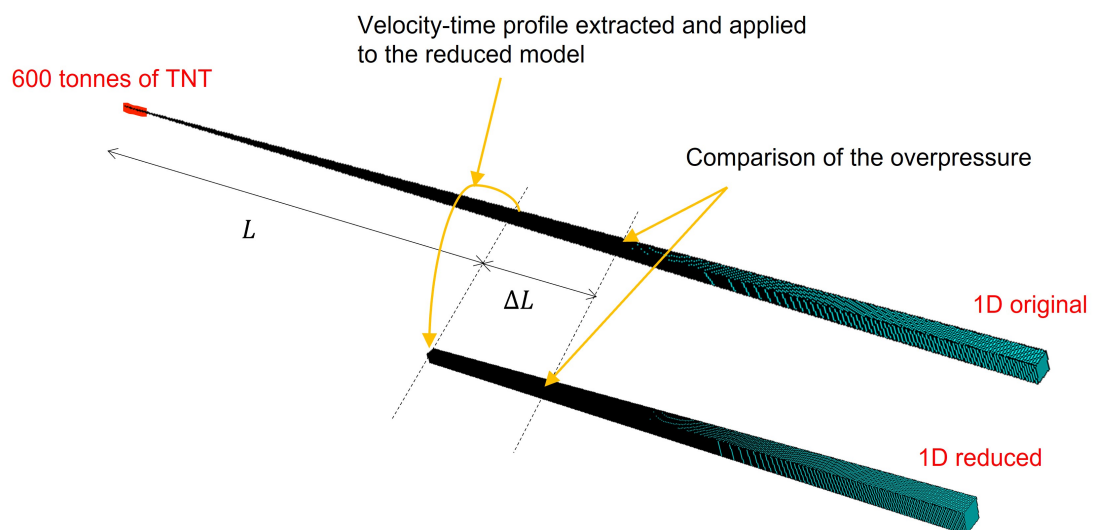
Figure 3.7: Spherically symmetrical free-air wave-propagation models in 1D for velocity boundary condition extraction and verification.
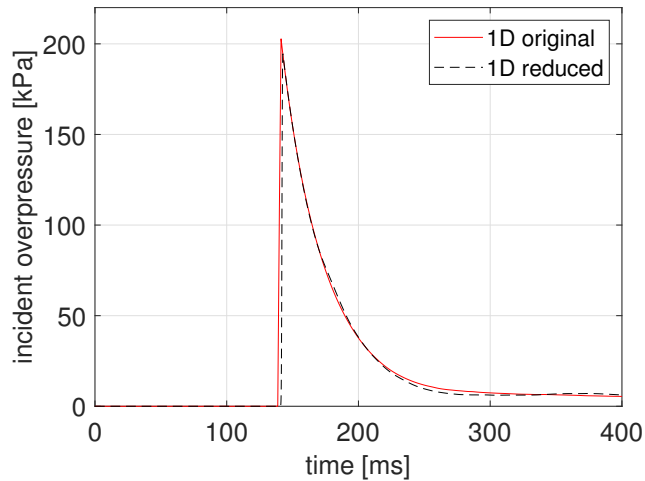
(a) Standoff distance of 150 m.
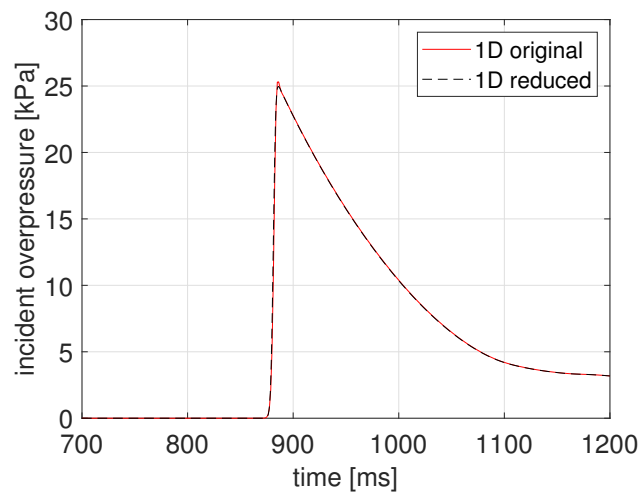
(b) Standoff distance of 450 m.

Figure 3.8: Overpressure histories from the original and the reduced 1D models at stand-off distances of (a) 150 m and (b) 450 m.

3.3   Exploring the effect of building porosity on the shielding of a blast wave

The validated modeling approaches are used to study the influence of building porosity on the propagation of the blast wave behind the structures. To this aim, fifteen main CEL simulations are run to characterize the incident overpressure and specific impulse behind the porous buildings exposed to the explosive surface charge equivalent to 300 tonnes of TNT. The peak average overpressure and specific impulse are determined, for the incident

wave, over virtual facades of 10×16.8 m^2 located 5, 10, 15, 20, 25, 30, 35 and 40 m behind the buildings. For each of the standoff distances considered, an adequate mesh size is selected to ensure convergence and a sufficiently large Eulerian domain is retained to avoid the effect of spurious reflections on the quantities of interest determined over the virtual facades.

3.3.1 Domain and mesh size retained in the far field

The model size reduction technique described in section 3.2.3 is applied to study the effect of building porosity on the propagation of the blast wave in the far field, at a standoff distance $D = 450$ m (equivalent to a scaled distance $Z = 6.7$ m/kg$^{\frac{1}{3}}$). To this aim, the velocity history is extracted from the 1D wave-propagation model at 390 meters from the center of the charge (Figure 3.9) and applied as a velocity boundary condition to a set of 3D models in the far field. In the latter, the structures are modeled at a distance of 60 m from the input boundary to prevent any spurious reflections potentially taking place on this boundary from altering the pressure determined over the virtual facades. It is interesting to note that the 'second' wave appearing in Figure 3.9 - at approximately 370 ms from the time of arrival of the first wave - is due to internal reflection of an inwardly-traveling expansion wave as it coalesces at the center of the charge (Rigby & Gitterman, 2016).
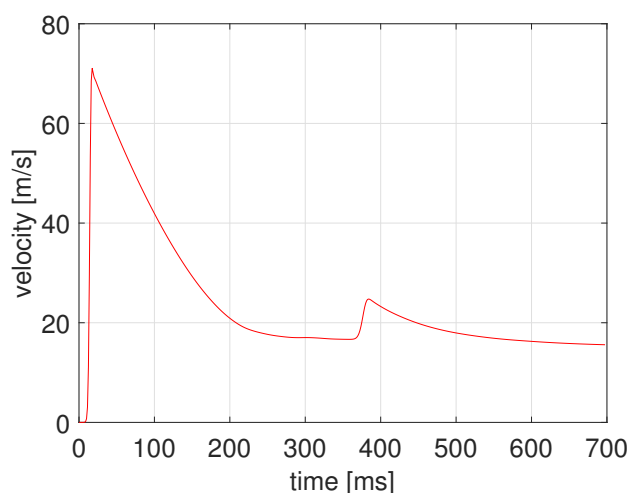
Figure 3.9: The velocity-field history at 390 m from the detonation point.

Figure 3.10 illustrates the modeling setup implementing buildings at 450 meters from

the detonation point: building location, virtual facades and domain boundaries are shown. Leveraging symmetry, half of the buildings are modeled and the domain representing air is considered as one quarter of a reduced pyramid of 200×200 m^2 base, 558 m height and apex located at the center of the charge, from which the part corresponding to a standoff distance of less than 390 m is removed. The size of the reduced domain is identified by the dimensions of its quarter base and the smallest distance between the input boundary and the output boundary i.e. $100 \times 168 \times 100$ m^3 for the domain illustrated in Figure 3.10. Specific Eulerian boundary conditions are applied to prevent the inflow/outflow of air through surfaces of symmetry, while an 'equilibrium' boundary condition is prescribed over the 'input' boundary upstream and the domain boundary downstream to reduce potential effects of spurious reflections.
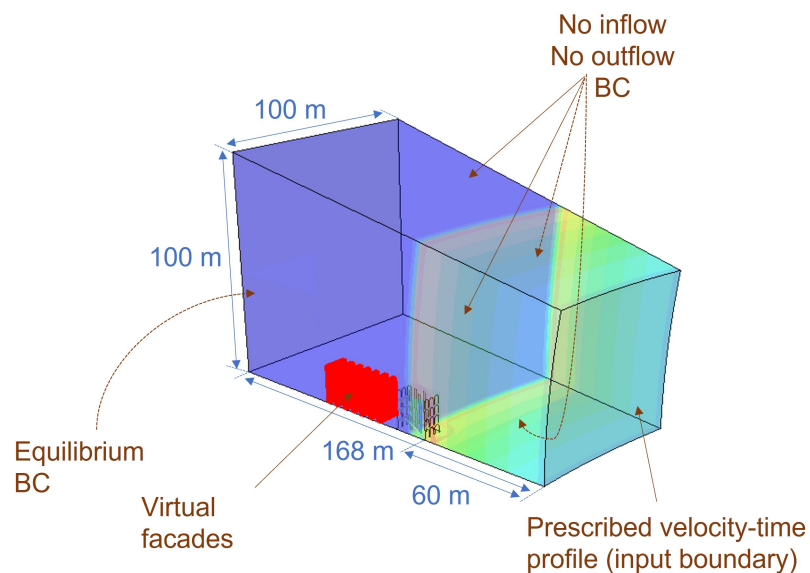
Figure 3.10: Modeling setup – 450 m standoff (far field).

(a) Side view of the whole domain.

(b) Refinement around the building.
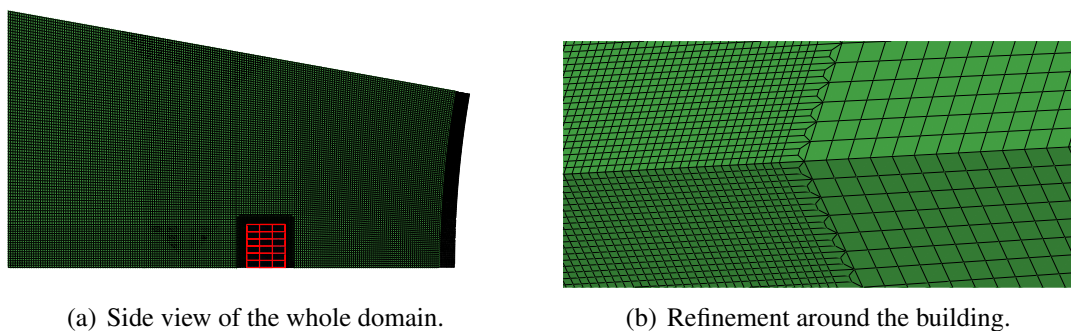
Figure 3.11: Illustration of the finite element mesh retained in the far field.

Four simulations are run for a domain of size $100 \times 168 \times 100$ m^3, meshed using hexahedral Eulerian elements of size 1.8, 1.5, 1.2, and 0.9 m in the regular region. Elements of one third the regular size are used around and inside the buildings to better capture the blast wave's behavior through the openings. Figure 3.11(a) shows an example of the whole domain meshed with 0.9 m elements in the regular region (and 0.3 m elements inside and around the building). Figure 3.11(b) corresponds to a detailed view of the mesh refinement showing transition elements designed following Parrish et al. (2008). A maximum simulation time-step of 2×10^{-4} seconds is prescribed.
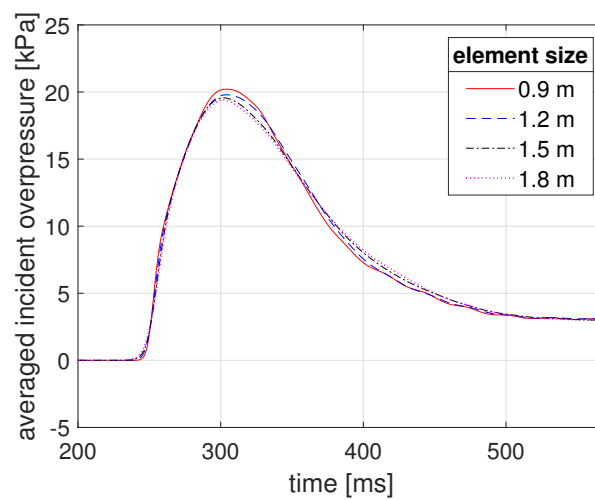
(a) Averaged incident overpressure.
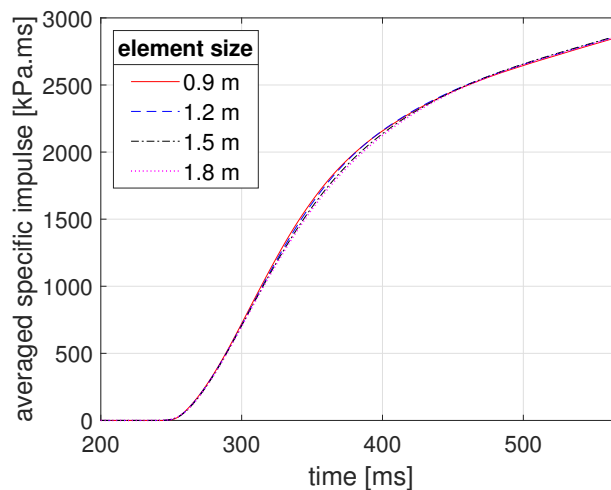
(b) Averaged specific impulse.

Figure 3.12: Mesh convergence analysis in the far field - (a) P_{avg} and (b) I_{avg} over the virtual facade located 10 m behind the building.

Figures 3.12(a) and (b) show, for the different mesh sizes retained, the averaged in-

cident overpressure P_{avg} and the averaged specific impulse I_{avg}, respectively, measured over the virtual facade located 10 m behind the low-porosity building. For all the virtual facades of interest, the difference in P_{avg} when the regular element size is decreased from 1.2 m to 0.9 m is less than 3.1%. The maximum difference drops below 0.4% for I_{avg}. A mesh size of 0.9 m is hence deemed adequate to achieve the objectives of this work at a feasible computational cost.

(a) Averaged incident overpressure.
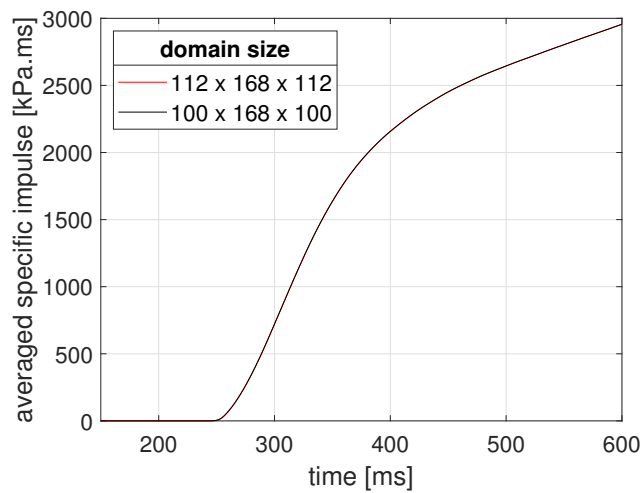
(b) Averaged specific impulse.

Figure 3.13: Far field domain size convergence - histories of P_{avg} and I_{avg} 10 m behind the building.

To ensure that the locations of the boundaries have no significant effect on the outputs of interest, the results of the simulation pertaining to a domain of $100 \times 168 \times 100$ m^3 are compared to those of a larger domain of $112 \times 168 \times 112$ m^3 for the low-porosity building

case. The same mesh fidelity is used in both simulations, with 0.9 m regular elements and 0.3 m elements inside and around the building. Figure 3.13 reveals that the models' outputs are almost indistinguishable. The smallest domain size of $100 \times 168 \times 100$ m^3 is thus retained. The specific impulse is estimated in each case by integration of the positive overpressure history up to a specific time shortly preceding the arrival of the second wave. These times are listed in Table 3.2.

Facade distance to	Integration time [ms]		
the building d [m]	Near field	Intermediate field	Far field
5	180	280	570
10	180	300	570
15	180	300	600
20	185	310	600
25	185	320	600
30	190	325	620
35	195	330	620
40	200	340	620

Table 3.2: Integration times retained for the calculation of the positive specific impulse (since the onset of the simulation).

3.3.2 Domain and mesh size retained in the intermediate field

The velocity-time profile extracted from the 1D wave-propagation model at 110 m from the charge (Figure 3.6) is applied as a boundary condition to a set of 3D models imple-
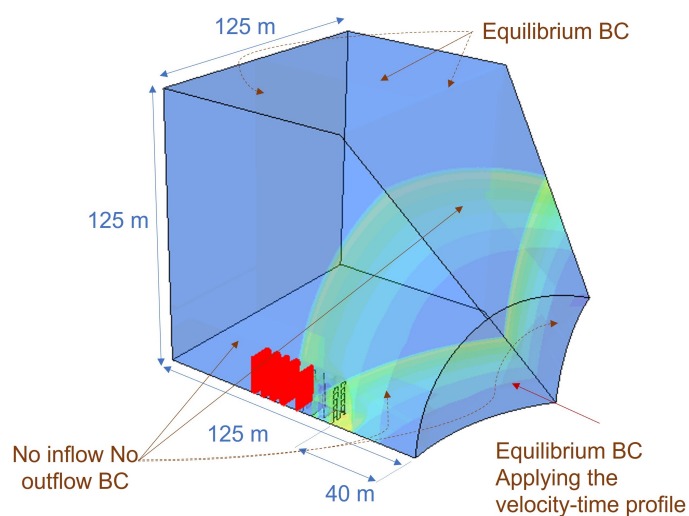
Figure 3.14: Modeling setup – 150 m standoff (intermediate field).

menting buildings in the intermediate field, at D = 150 m from the detonation point (corresponding to a scaled distance Z = 2.2 m/kg$^{\frac{1}{3}}$). The domain representing air, the building location, the virtual facades and the boundary conditions are shown in Figure 3.14. The $125 \times 125 \times 125$ m^3 size domain retained is meshed using linear cubic elements of size 0.9 m in the regular zone. The element size is reduced to 0.3 m inside and around the building. A maximum simulation time-step of 1×10^{-5} seconds is prescribed.

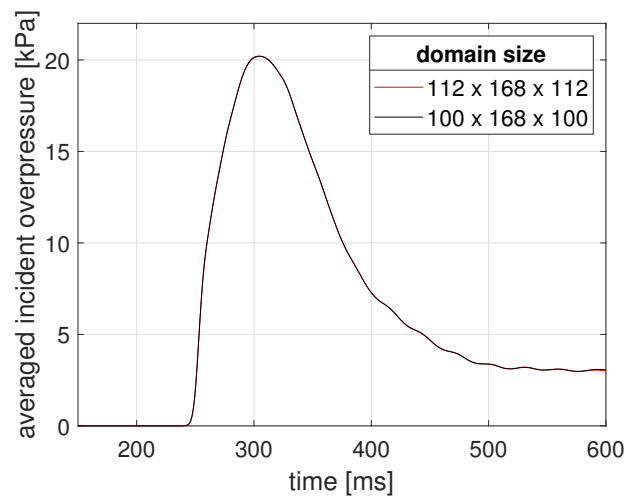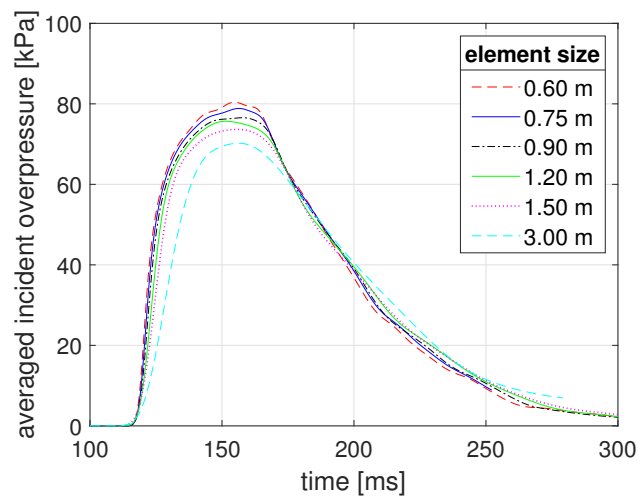(a) Averaged incident overpressure.
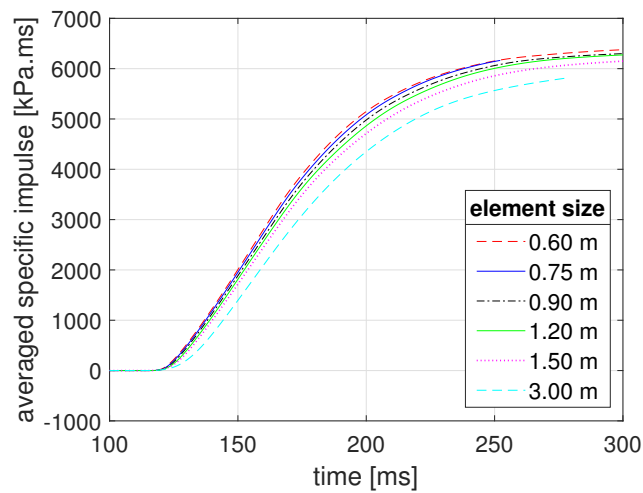
(b) Averaged specific impulse.

Figure 3.15: Mesh convergence analysis in the intermediate field - (a) P_{avg} and (b) I_{avg} over the virtual facade located 10 m behind the building.

A mesh convergence analysis conducted on the conservative case corresponding to the low-porosity building for a domain of $103 \times 110 \times 100$ m^3 reveals that the change in P_{avg} when the regular element size is decreased from 0.9 m to 0.6 m does not exceed 4.8%,

locally. The maximum change drops below 1.2% for I_{avg}. A regular mesh size of 0.9 m is hence deemed adequate for all practical purposes. Figures 3.15(a) and (b) illustrate P_{avg} and I_{avg} (respectively) determined over the virtual facade located 10 m behind the low-porosity building using global elements of 3.0, 1.5, 1.2, 0.9, 0.75 and 0.6 m size.

(a) Averaged incident overpressure.

(b) Averaged specific impulse.

Figure 3.16: Intermediate field domain size convergence - histories of P_{avg} and I_{avg} 10 m behind the building.

The model's boundaries are set such that the incident overpressures determined across the virtual facades become significantly smaller than their corresponding peak before being disturbed by any spurious reflections. The specific impulse can thus be estimated in each case by integration of the positive overpressure history up to a specific time (measured from the time of arrival of the wave at the input boundary) beyond which the re-

maining contributions are small. These times are listed in Table 3.2.

P_{avg} and I_{avg} determined at 10 m behind the low-porosity building, are compared to those extracted from a 25% larger domain, meshed using the same element sizes, in Figures 3.16(a) and (b). It can be seen that the models' outputs are fairly close, up to the specified time at which I_{avg} is determined. The largest domain size of $125 \times 125 \times 125$ m^3 is thus retained.

3.3.3 Domain and mesh size retained in the near field

A hemispherical charge of radius 4.45 m, corresponding to 300 tonnes of TNT, is represented using the JWL material model parameters retained in section 3.2.2. Leveraging symmetry, only one-quarter of the charge and one-half of the building are modeled. A rectangular domain of $60 \times 130 \times 60$ m^3 is retained. The domain is meshed using 0.45 m elements in the regular region. The mesh is refined locally with elements of 0.15 m in and around the charge, while a maximum simulation time-step of 3.5×10^{-5} seconds is prescribed. Figure 3.17 illustrates the modeling setup implementing buildings in the near field, at D = 50 m from the detonation point (corresponding to a scaled distance $Z = 0.7$ m/kg$^{\frac{1}{3}}$): building location, virtual facades and domain boundaries are shown.
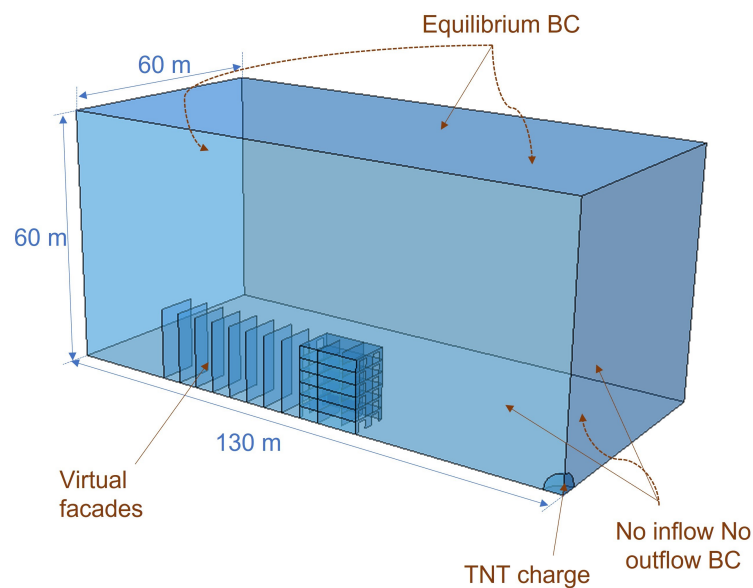
Figure 3.17: Modeling setup – 50 m standoff (near field).

Figures 3.18(a) and (b) compare P_{avg} and I_{avg}, respectively, determined over the vir-

tual facade located 10 m behind the low-porosity building for mesh sizes of 0.55, 0.50, 0.45 and 0.40 m. For all the virtual facades of interest, the change in P_{avg} when the regular element size is decreased from 0.45 m to 0.40 m does not exceed 4.1%, locally. The maximum change drops below 2.7% for I_{avg}. A regular mesh size of 0.45 m is hence deemed adequate for all practical purposes. The mesh refinement inside the charge corresponds to approximately 30 elements along the radial direction, which is consistent with that prescribed by Giam et al. (2020).
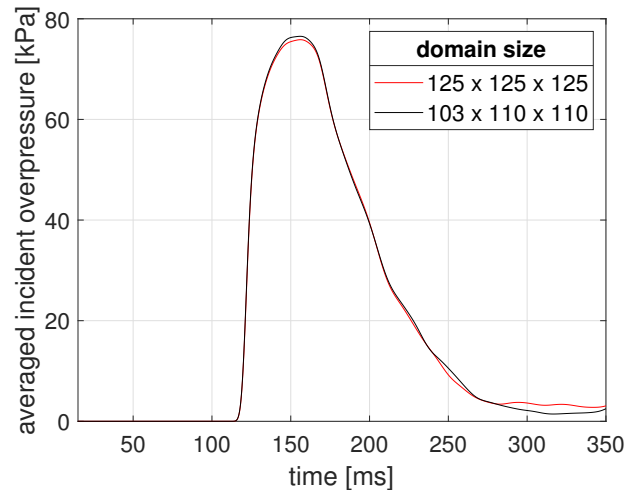

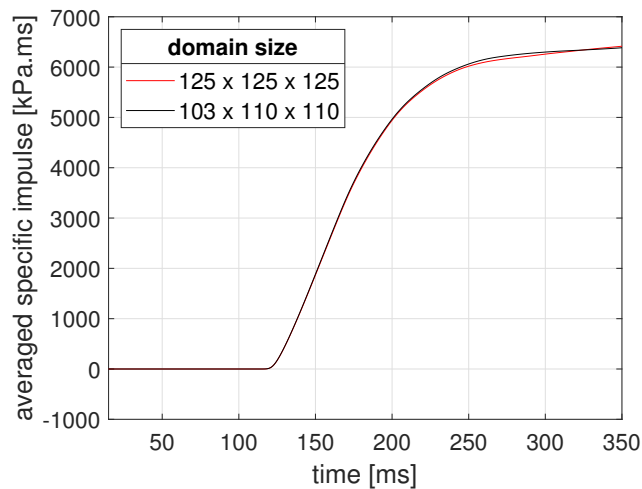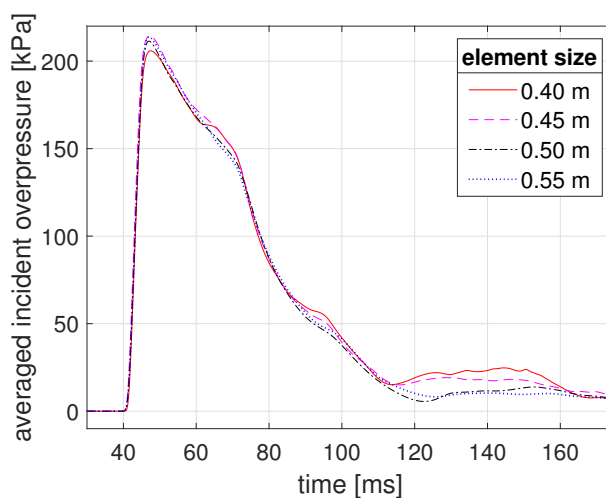(a) Averaged incident overpressure.
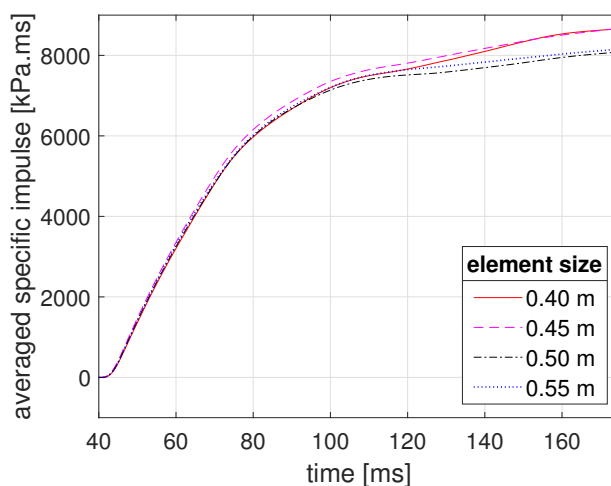
(b) Averaged specific impulse.

Figure 3.18: Mesh convergence analysis in the near field - (a) P_{avg} and (b) I_{avg} over the virtual facade located 10 m behind the building.

The specific impulse is calculated by integrating the overpressure up to the times listed in Table 3.2. These were selected to ensure suitable convergence of the impulse while

avoiding any disturbances from spurious reflections potentially occurring over equilibrium boundaries of the domain. A comparison between P_{avg} and I_{avg} evaluated for two domain sizes of $55 \times 130 \times 55$ m^3 and $60 \times 130 \times 60$ m^3 over the virtual facade located conservatively 10 m behind the low-porosity building is shown in Figure 3.19. The largest domain is retained as the models' outputs are fairly close.
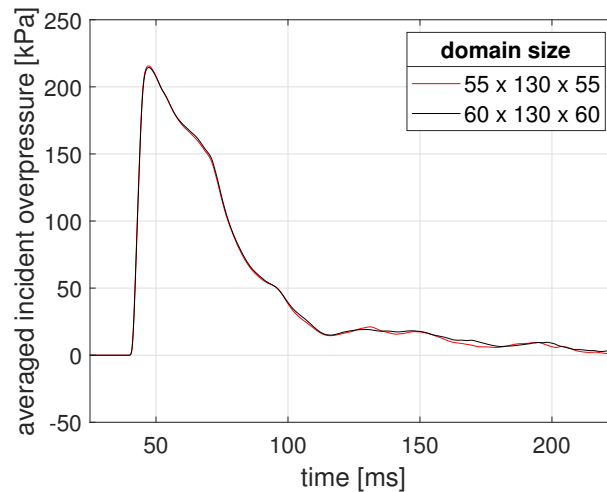
(a) Averaged incident overpressure.
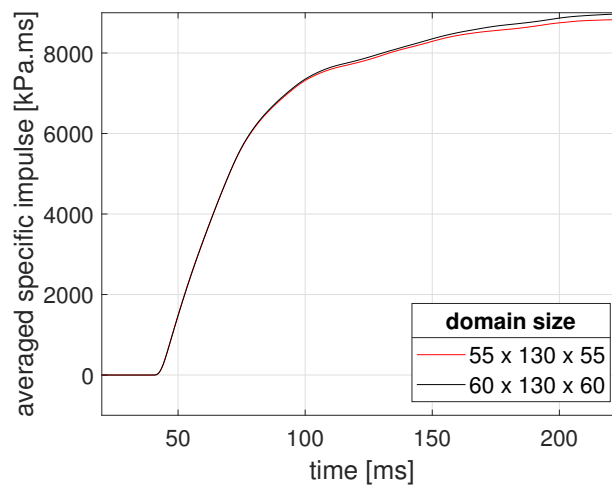
(b) Averaged specific impulse.

Figure 3.19: Domain size convergence in the near field - histories of P_{avg} and I_{avg} 10 m behind the building.

3.3.4 Results and discussion

Compiled results

Designating by d the distance between the back of the shielding structure and the virtual facade of interest, the peak facade-averaged incident overpressure P_{avg}, facade-averaged peak incident overpressure $\hat{P}_{avg}$ and facade-averaged specific impulse I_{avg} are represented versus d, in percent of the same quantities in free air (i.e. without the structure) in Figures 3.20, 3.21 and 3.22 respectively, for the three standoff distances and for the four porosity levels retained in this work. The corresponding percent free-air quantities are denoted p_{avg}, $\hat{p}_{avg}$ and i_{avg}, respectively. P_{avg} can be of interest in evaluating the overall behavior of a shielded structure, or that of its large components. Alternatively, the more conservative average of the (non-simultaneous) peak overpressures $\hat{P}_{avg}$ could be retained for the local design of smaller elements. Both p_{avg} and $\hat{p}_{avg}$ are thus provided in this work; although the discussion is held in terms of p_{avg}, mainly. The values of P_{avg}, $\hat{P}_{avg}$ and I_{avg} resulting from the CEL simulations are listed in Tables 3.9–3.11. The contour plots of percent free-air peak incident overpressure and specific impulse over the virtual facades are shown in Figures 3.36–3.41 for the standoff distances of 50, 150 and 450 m.

In the near field, p_{avg} is bounded below by the zero-porosity case, and above, by the high-porosity case, up to at least $d = 40$ m. In the intermediate and far fields however, it is mainly the low-porosity case that constitutes the lower bound of p_{avg}. Also for d greater than 30 m, the p_{avg} experienced behind the medium-porosity building becomes the highest (Figure 3.20).

Figure 3.22 reveals that i_{avg} is bounded by two envelopes, one below pertaining to the zero-porosity building and the other above, to the high-porosity building; except in the far field, where the lowest impulse occurs behind the low-porosity building. I_{avg} becomes approximately equal to that in free air at distances larger than 15 m and 20 m behind the building, at the standoff distances of 450 m and 150 m, respectively.

Overall, the shielding effect wanes as the standoff distance increases. For instance, at $D = 450$ m, the lowest p_{avg} and i_{avg} are of 74% and 95%, respectively, 5 m behind

the building. Those values drop to 38% and 68% respectively at $D = 150$ m, and to 14% and 52% respectively at $D = 50$ m. The zero-porosity and low-porosity buildings provide roughly similar shielding performances with respect to overpressure; however, the difference in the specific impulse experienced behind those buildings increases as they get closer to the charge. It is also interesting to note that the high-porosity structure can contribute to increasing the intensity of the blast wave in its wake. This effect however fades as the standoff distance to the charge increases. Overall, the shielding performance of the medium-porosity building is intermediate between that of the zero/low-porosity and high-porosity structures. Also in general, the lower the building porosity, the more it delays the rise to peak overpressure. This effect, which is clearly revealed, for example, in Figures 3.28 to 3.30, can be attributed to the longer paths that the blast wave is forced to take by the less porous structures.
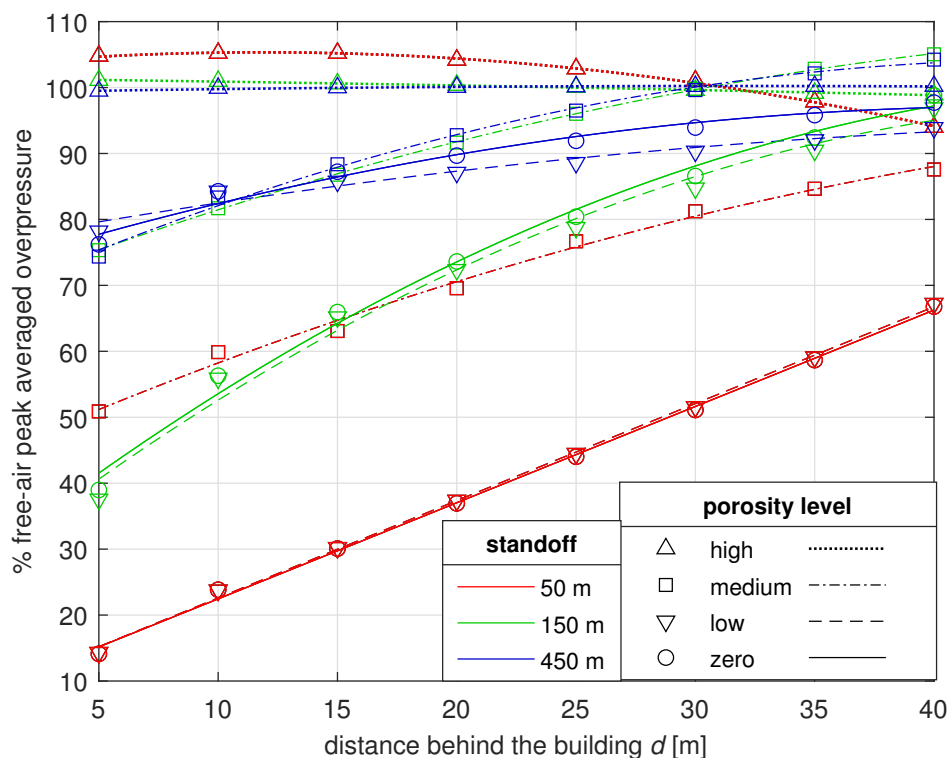
Figure 3.20: p_{avg} plotted against virtual facade distance behind the shielding structures. Markers represent numerical data while trend lines represent fitted functions.
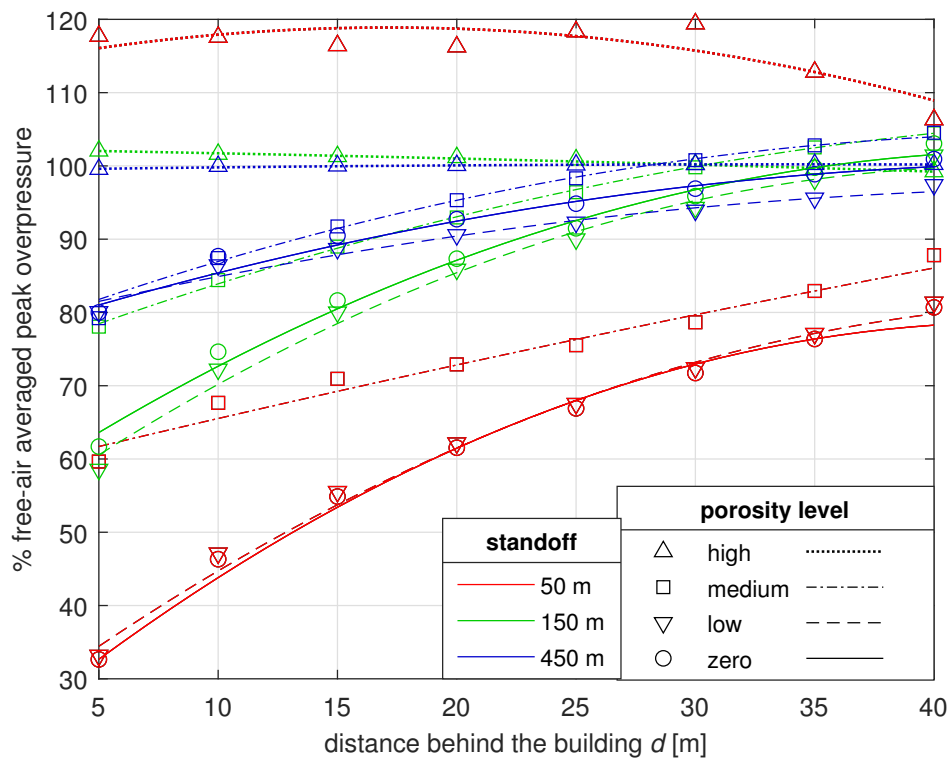
Figure 3.21: $\hat{p}_{avg}$ plotted against virtual facade distance behind the shielding structures. Markers represent numerical data while trend lines represent fitted functions.
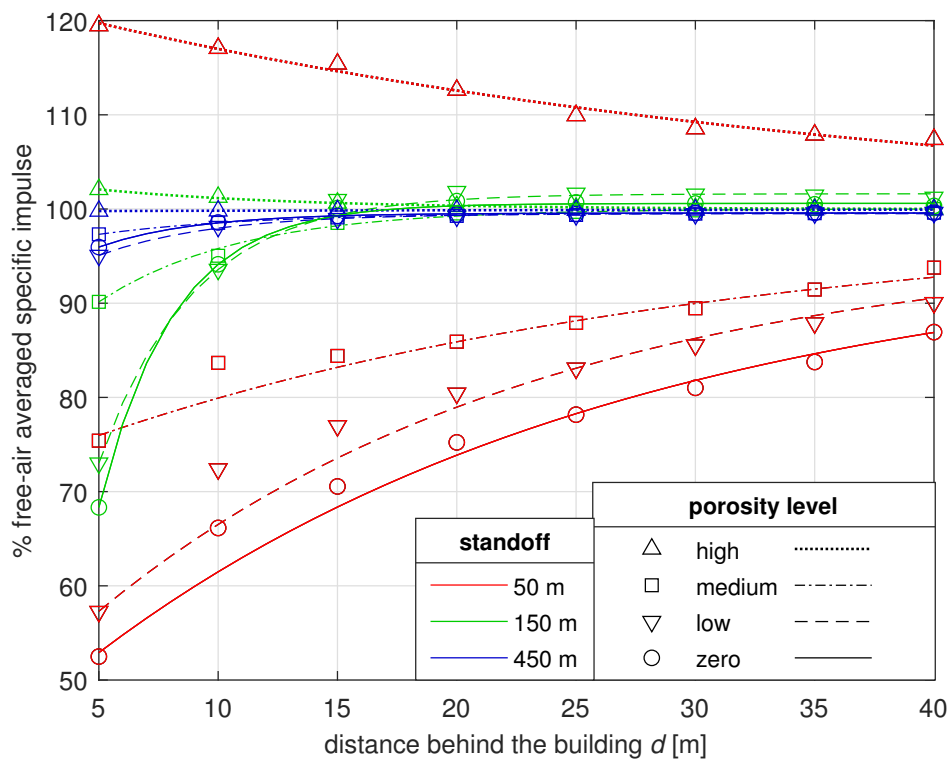
Figure 3.22: i_{avg} plotted against virtual facade distance behind the shielding structures. Markers represent numerical data while trend lines represent fitted functions.

High-porosity building

In the near and intermediate fields, the blast wave is amplified behind the high-porosity building due to an internal channeling effect taking place freely between the parallel floor slabs and side-walls, unimpeded by any partition walls. This is best illustrated in the near field by the contour plots of overpressure shown in Figures 3.23(a) and (b). The phenomenon wanes with increasing standoff distance as the blast wave over the building's height becomes increasingly planar, thus interacting less with the slabs and side-walls. For example, in the near field, both P_{avg} and I_{avg} are larger than in free air up to 30 m approximately behind the structure (Figures 3.20 and 3.22). This is the case up to no more than 20 m in the intermediate field, while in the far field the specific impulses experienced by the virtual facades are approximately equal to those in free air.

(a) Vertical cross-section at 9 m from the plane of symmetry.
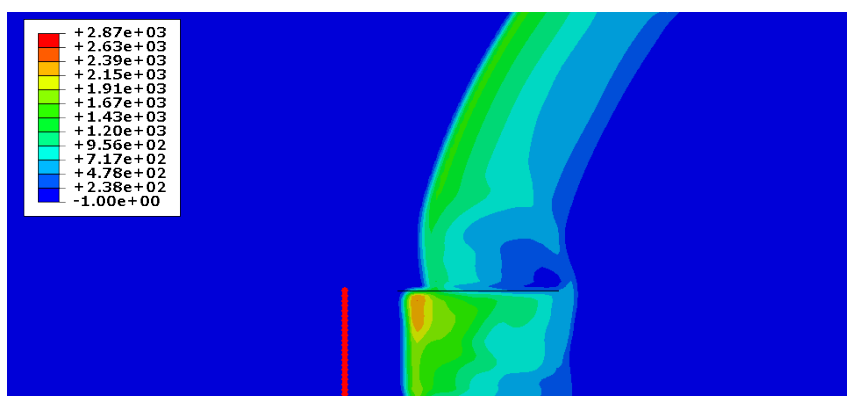
(b) Horizontal cross-section at 5 m from the ground.

Figure 3.23: Contour plots of the overpressure (in kPa) for the high-porosity building in the near field, 28.81 ms after detonation. The lines in red represent the virtual facade located 5 m behind the building.

Medium-porosity building

Overall, the medium-porosity building provides notable shielding at distances d that are roughly less than 15 and 20 m downstream in the far and intermediate fields, respectively. In this regard, it is interesting to note that, although P_{avg} remains smaller than in free air up to 30 m behind the building, I_{avg} is not affected significantly beyond half that distance. The shielding effect of the medium-porosity building extends up to at least $d = 40$ m in the near field (Figures 3.20 and 3.22). In the intermediate and far fields, P_{avg} is higher than in free air at 35 and 40 m behind the building (Figure 3.20), while the virtual facades located at distances d larger than about 15 m experience, centrally, a peak overpressure larger than that in free air (Figure 3.24(a)). This can be attributed to the interference between the wave passing through the openings in the structure and that traveling around the building's envelope before converging centrally, further downstream (Figures 3.25(a) and (b)).

(a) Far field; $d = 35$ m.   (b) Near field; $d = 5$ m.
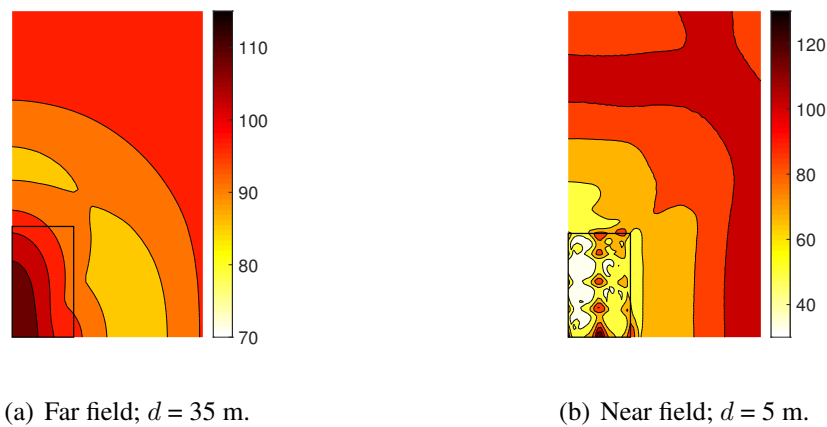
Figure 3.24: Contour plots of percent free-air peak overpressure behind the medium-porosity building. The dimensions of the cross-sections are three times those of the building whose trace corresponds to the black rectangle on the bottom left.

In the near field, the virtual facades close-in behind the medium-porosity structure (e.g. 5 m) present field patterns that are consistent with the layout of openings and experience, centrally at the ground floor, a peak overpressure higher than in free air due to the scattering of the blast wave by the three openings, followed by an interference of the scattered waves (Figures 3.24(b) and 3.26).
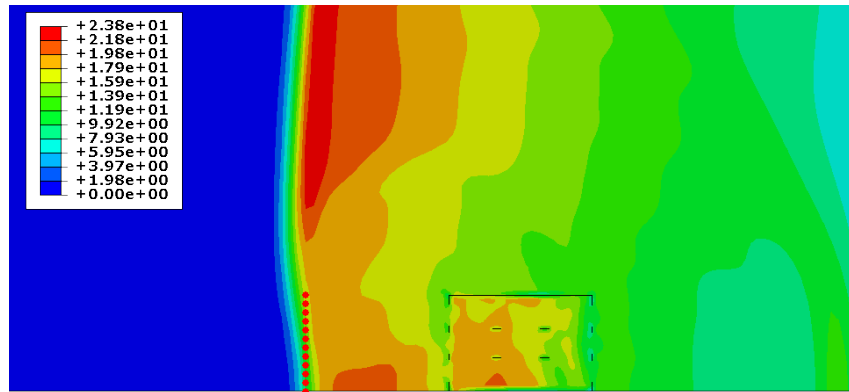
(a) Horizontal cross-section at 2 m from the ground.
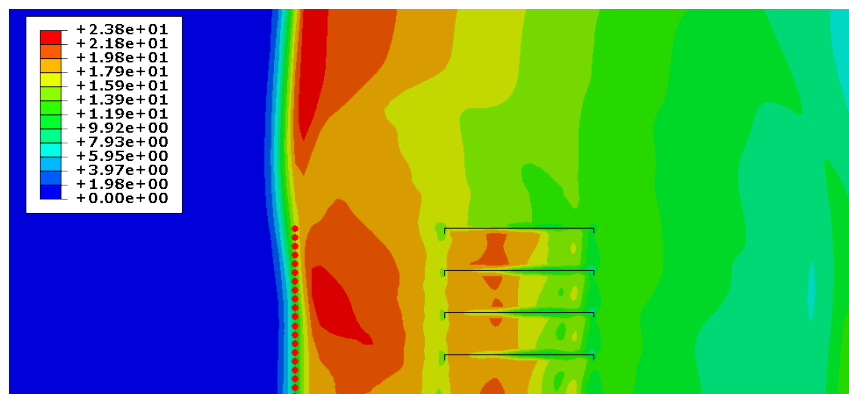
(b) Vertical cross-section at 2 m from the plane of symmetry.

Figure 3.25: Contour plots of the overpressure (in kPa) for the medium-porosity building in the far field, 268.7 ms after detonation. The dotted lines in red represent the virtual facade located 15 m behind the building.
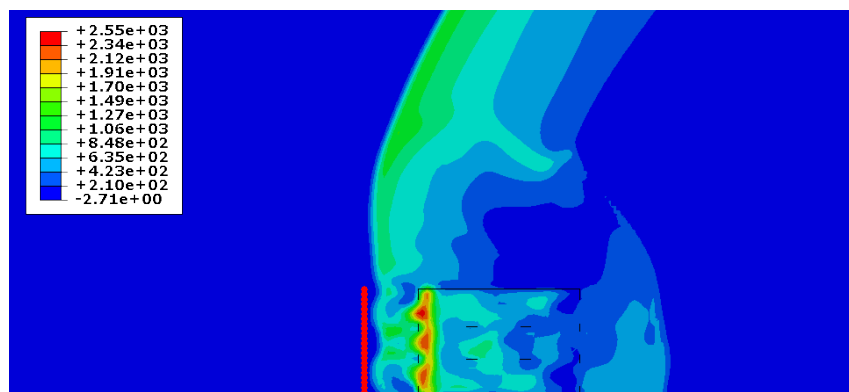
Figure 3.26: Contour plots of the overpressure (in kPa) at the ground-floor level of the medium porosity building located in the near field, 34.2 ms after detonation. The red lines represent the virtual facade located 5 m behind the building.

Low-porosity building

The near-field consequences of the interactions of the blast-wave penetrating the low-porosity building through its front openings are less significant than in the case of medium

porosity. This can be related to the smaller size of the openings and to the shielding of such interactions, at each floor, by the denser internal partitioning of the low-porosity structure. The latter also prevents an internal channeling effect from taking place, as in the high-porosity case, between the slabs and the sidewalls. The global interactions of the blast-wave with the envelope of the low-porosity structure are thus dominant. The wave mainly travels around the building, diffracts at its edges and subsequently converges centrally downstream, resulting in peak overpressures that are locally larger than in free air at distances d larger than 10 m. In the intermediate and far fields, the wave circumventing the structure also penetrates it backwards from the openings located leeward (Figures 3.27(a) and (b)). This leads to local peak overpressures (and a $\hat{p}_{avg}$) that are lower than those experienced in the zero-porosity case.
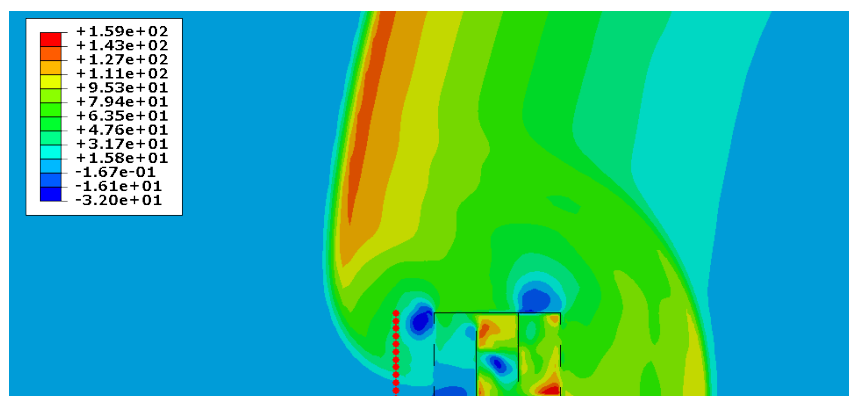
(a) Horizontal cross-section at 2 m from the ground.
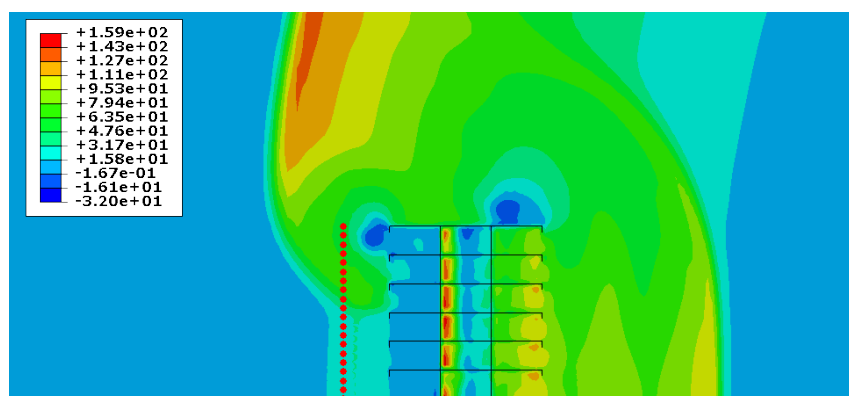
(b) Vertical cross-section at 2 m from the plane of symmetry.

Figure 3.27: Contour plots of the overpressure (in kPa) for the low-porosity building in the intermediate field, 122.7 ms after detonation. The dotted vertical lines in red represent the virtual facade located 5 m behind the building.

In the far field, the wave that penetrated the structure backwards reflects on its internal

walls and exits the building from the back early, i.e. during the positive phase of the outer circling wave, as the latter continues to progress. Their interference behind the structure leads to a p_{avg}, at d = 5 m, higher than in the zero-porosity case while i_{avg} remains lower (Figures 3.28(a) and (b)).
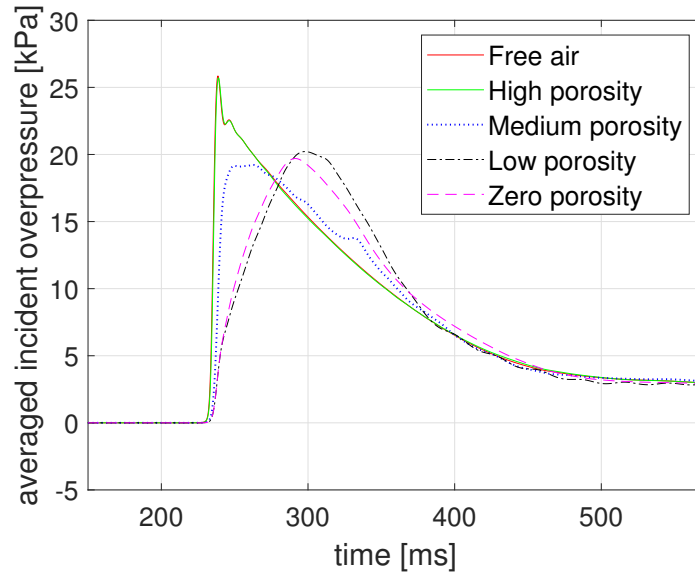
(a) Average incident overpressure.
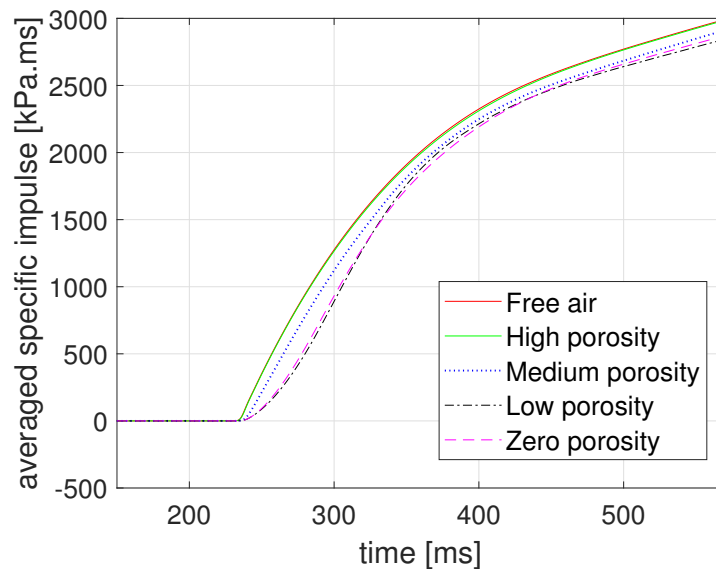
(b) Averaged specific impulse.

Figure 3.28: Average overpressure and specific impulse histories in the far field, at $d = 5$ m.

In the intermediate field however, the wave that penetrated the building from the openings at the front and the wave that penetrated the building from the back – before being

reflected by the internal walls – both exit the building from the back at a later stage, after the outer wave has passed, resulting in a higher i_{avg} than in the case of zero porosity, while p_{avg} remains lower (Figures 3.29(a) and (b)). In the near field, the wave that travels across the building exits through the openings at the back towards the end of the positive time of the outer circling wave, which results in an i_{avg} higher than in the zero-porosity case while p_{avg} remains lower (Figures 3.30(a) and (b)).
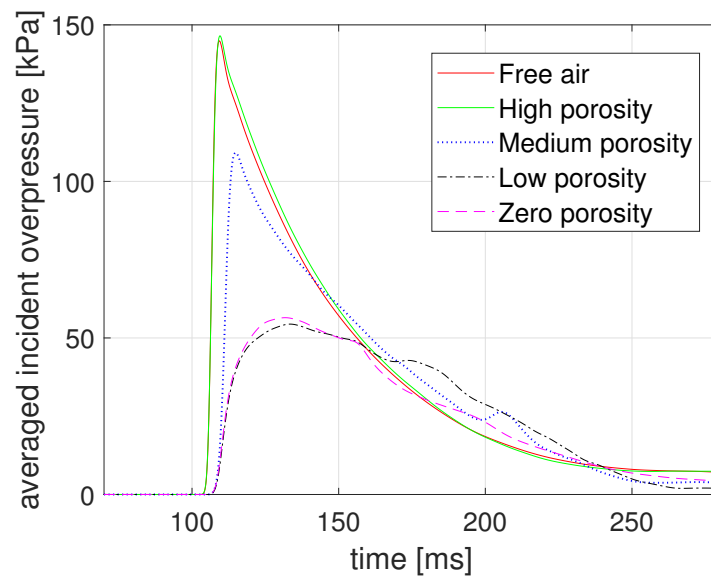
(a) Averaged incident overpressure.
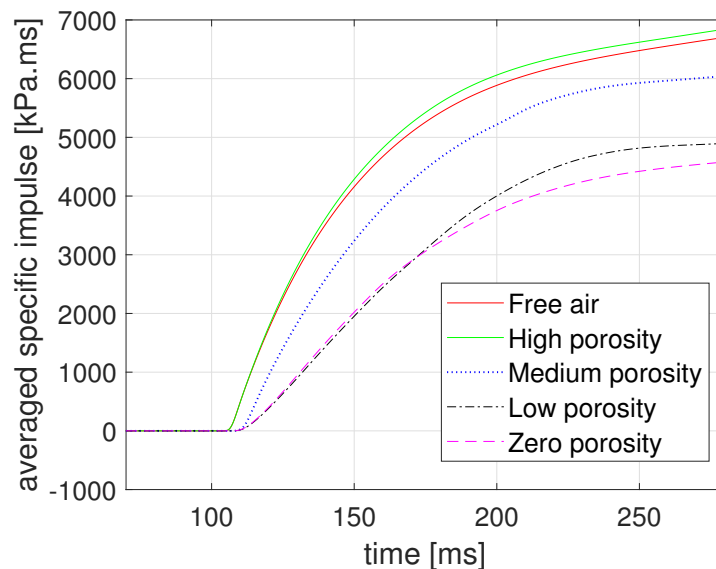
(b) Averaged specific impulse.

Figure 3.29: Average overpressure and specific impulse histories in the intermediate field, at $d = 5$ m.
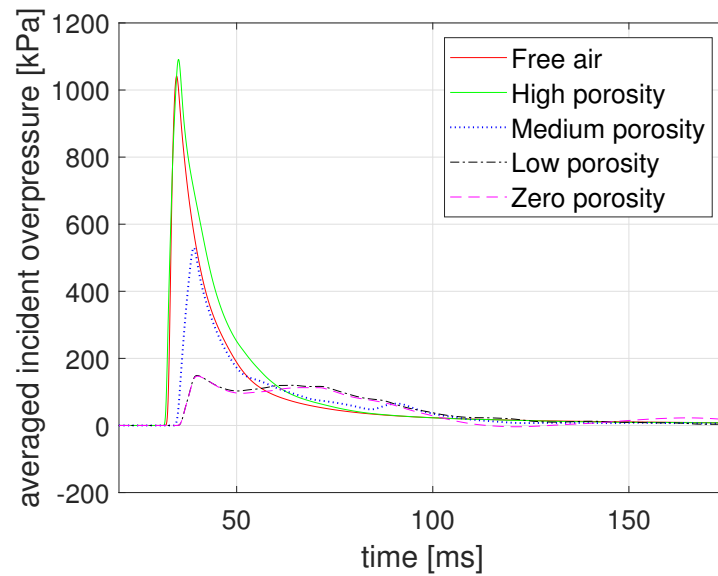
(a) Averaged incident overpressure.
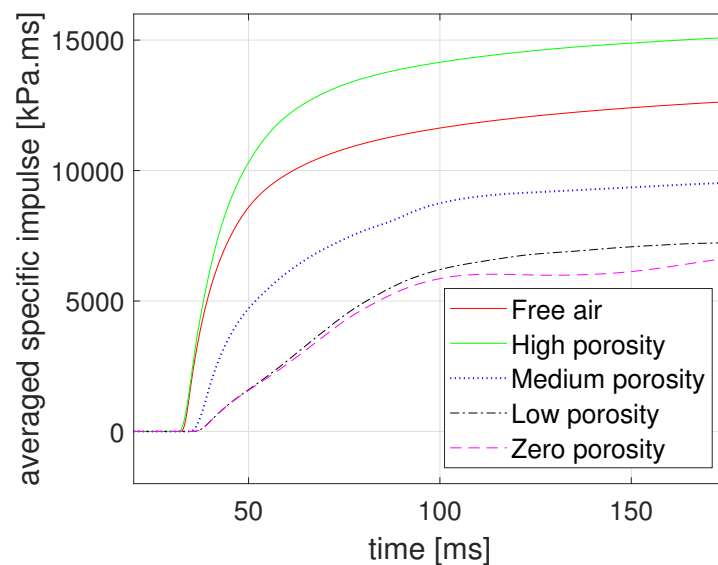
(b) Averaged specific impulse.

Figure 3.30: Average overpressure and specific impulse histories in the near field, at $d = 5$ m.

Zero-porosity building

The blast wave goes fully around the zero-porosity structure, diffracts at its edges and subsequently converges centrally in its wake, resulting in peak overpressures that are locally higher than in free air at distances d larger than 5 m in the far field, and larger than 10 m in the intermediate and near fields. It is also interesting to note that the wave circling the structure reflects on its back wall before converging centrally. Overall, the

zero-porosity building provides notable shielding up to a distance d of 40 m at least, in the near field; however, its shielding capacity decreases with the standoff distance D. For instance, in the intermediate and near fields I_{avg} is lower than in free air up to $d \approx 20$ m only (Figure 3.20 and 3.22).

3.4   Data-driven surrogate modeling

3.4.1   Scaling

The problem can also be formulated in nondimensional form, for more generality. To this aim, the variables involved can be scaled in relation to:

(i) the characteristic dimension of the shielding structure defined as L_s = min(H_s, $W_s/2$), where H_s and W_s are the structure's height and width, respectively, normal to the direction of propagation of the blast wave, and

(ii) the properties of the blast wave in free air, at the same location as the back of the shielding structure (i.e. at $D + D_s$; D_s designating the structure's depth). The wave is mainly characterized by its peak overpressure $\bar{P}$ and its estimated duration time t_d; or alternatively, by its wave 'length' $L_d = C \times t_d$, where C = 340.3 m/s designates the speed of sound in the unperturbed air of initial pressure P_o = 101.325 kPa.

Referring to the Buckingham Π theorem, the dimensionless quantities of interest p_{avg}, $\hat{p}_{avg}$ and i_{avg} can thus be expressed in terms of the four dimensionless parameters, namely: the porosity level PL, the normalized distance behind the building $d_n = d/L_s$, the normalized wave 'length' $L_{dn} = L_d/L_s$ and $\bar{P}/P_o$. It can furthermore be assumed that the influence of $\bar{P}/P_o$ is marginal, based on previous works (e.g. Geng & Thomas, 2020). For the building dimensions retained in this work, L_s = min(16.8, 20/2) = 10 m and D_s = 15 m, the normalized incident wave lengths at $D + D_s$ are summarized in Table 3.3.

Field	Standoff distance D [m]	Scaled distance Z [m/kg$^{1/3}$]	Estimated duration t_d [ms]	Wave length L_d [m]	Normalized wave length L_{dn} [-]
Near	50	0.7	40	13.6	1.36
Intermediate	150	2.2	125	42.5	4.25
Far	450	6.7	335	114.0	11.40

Table 3.3: Normalized blast wave lengths in free air, at $D + D_s$.

3.4.2 Regression analysis

The percent free-air peak facade-averaged overpressure p_{avg}, and facade-averaged peak incident overpressure $\hat{p}_{avg}$, increase with the normalized distance d_n following trends that are best fitted by quadratic functions (Figures 3.20 and 3.21):

$$p_{avg} = p_0 + p_1 d_n + p_2 d_n^2, \tag{3.4}$$

$$\hat{p}_{avg} = \hat{p}_0 + \hat{p}_1 d_n + \hat{p}_2 d_n^2, \tag{3.5}$$

where p_i and $\hat{p}_i$, $i \in \{0, 1, 2\}$ are parameters. The percent free-air facade-averaged specific impulse, i_{avg}, increases with d_n following a trend that is best fitted by a first order exponential decay function (Figure 3.22):

$$i_{avg} = 100 \times a \left(1 - b e^{-c d_n}\right), \tag{3.6}$$

where a, b and c are parameters. The functions' parameters are fitted to the numerical data for each porosity level and standoff distance to the charge. These and the corresponding mean relative errors (MRE) are given in Tables 3.4, 3.5 and 3.6, for p_{avg}, $\hat{p}_{avg}$ and i_{avg}, respectively. The MRE is defined as:

$$\text{MRE}(\%) = 100 \times \frac{1}{N} \sum_{i=1}^{N} \left| \frac{Y_p^i - Y_t^i}{Y_t^i} \right|, \tag{3.7}$$

where N is the number of fitted data points, while Y_p^i and Y_t^i correspond to the predicted and the target values, respectively.

Standoff	Porosity	p_0	p_1	p_2	MRE(%)
D = 50 m	zero	7.897	14.549	0.010	2.2
L_{dn} = 1.36	low	7.804	14.818	-0.021	1.8
Z = 0.7 m/kg$^{\frac{1}{3}}$	medium	43.510	15.923	-1.198	1.2
(near field)	high	103.363	3.342	-1.411	0.1
D = 150 m	zero	28.130	28.162	-2.723	2.5
L_{dn} = 4.25	low	27.231	28.170	-2.805	3.0
Z = 2.2 m/kg$^{\frac{1}{3}}$	medium	68.727	13.946	-1.209	0.1
(interm. field)	high	101.381	-0.425	-0.053	0.1
D = 450 m	zero	72.441	11.250	-1.280	1.0
L_{dn} = 11.40	low	76.459	6.647	-0.609	0.9
Z = 6.7 m/kg$^{\frac{1}{3}}$	medium	67.760	16.099	-1.775	0.6
(far field)	high	99.213	0.644	-0.101	0.1

Table 3.4: Equation 3.4 for p_{avg} - fitted parameters and corresponding MRE.

Standoff	Porosity	$\hat{p}_0$	$\hat{p}_1$	$\hat{p}_2$	MRE(%)
D = 50 m	zero	19.965	26.936	-3.090	1.8
L_{dn} = 1.36	low	22.873	24.396	-2.543	2.1
Z = 0.7 m/kg$^{\frac{1}{3}}$	medium	57.764	7.991	-0.229	1.7
(near field)	high	113.281	6.538	-1.906	1.5
D = 150 m	zero	53.360	21.717	-2.417	1.4
L_{dn} = 4.25	low	49.571	23.322	-2.697	1.6
Z = 2.2 m/kg$^{\frac{1}{3}}$	medium	72.450	12.607	-1.151	0.2
(interm. field)	high	102.323	-0.541	-0.059	0.1
D = 450 m	zero	76.088	10.424	-1.119	0.9
L_{dn} = 11.40	low	77.708	8.019	-0.832	0.8
Z = 6.7 m/kg$^{\frac{1}{3}}$	medium	75.927	12.368	-1.339	0.6
(far field)	high	99.381	0.488	-0.072	0.0

Table 3.5: Equation 3.5 for $\hat{p}_{avg}$ - fitted parameters and corresponding MRE.

Standoff	Porosity	a	b	c	MRE(%)
D = 50 m	zero	0.960	0.561	0.444	1.9
L_{dn} = 1.36	low	0.966	0.531	0.534	2.1
Z = 0.7 m/kg$^{\frac{1}{3}}$	medium	0.987	0.279	0.382	1.1
(near field)	high	0.991	-0.240	0.284	0.4
D = 150 m	zero	1.006	1.601	3.216	0.2
L_{dn} = 4.25	low	1.016	1.001	2.538	0.4
Z = 2.2 m/kg$^{\frac{1}{3}}$	medium	1.000	0.231	1.703	0.2
(interm. field)	high	1.000	-0.038	1.161	0.0
D = 450 m	zero	0.996	0.126	2.486	0.0
L_{dn} = 11.40	low	0.995	0.129	2.119	0.1
Z = 6.7 m/kg$^{\frac{1}{3}}$	medium	0.996	0.049	1.547	0.0
(far field)	high	1.000	0.002	0.353	0.0

Table 3.6: Equations 3.6 for i_{avg} - fitted parameters and corresponding MRE.

3.4.3   A machine learning model

The manifold of numerical data points determined by means of the computationally expensive high-fidelity CEL simulations designed and implemented in this work is leveraged further here to develop a more efficient predictive tool for p_{avg}, $\hat{p}_{avg}$ and i_{avg}. To this aim, an artificial neural network (ANN) is designed and trained on the dataset shown in Figures 3.20–3.22 scaled as described in section 3.4.1. The ANN comprises three neurons in the input layer, receiving the three input quantities corresponding to the normalized length L_{dn} of the incident wave in free air, the porosity level PL of the shielding structure, and the scaled distance d_n of the virtual facade over which the shielding effect is considered. To enable and facilitate interpolation over porosity, the input PL is considered as a continuous variable taking the integer values from 0 to 4 for the porosity levels retained in this work, in increasing order, i.e. 0 for zero porosity and 4 for free air. The output layer comprises three neurons delivering predictions of p_{avg}, $\hat{p}_{avg}$ and i_{avg}, corresponding to the inputs. The number of hidden layers, their sizes and the activation functions retained are optimized for best performance, including generalization to a testing set of data. This is achieved through random selection of 70% of the data for training, 15% for validation and the remaining 15% for testing. Following this process, two fully-connected hidden layers comprising 7 neurons each, and a sigmoid activation function h are retained. Table 3.7 illustrates this selection process by comparing the performances of a few different architectures with a sigmoid activation function.

Designating by $\mathbf{X}_1$ the 3×1 array of inputs, centered and scaled to the interval [-1,1], the 3×1 array of outputs $\mathbf{A}_3$, also centered and scaled to [-1,1], is given by:

$$\mathbf{A}_3 = \mathbf{W}_3.h\left(\mathbf{W}_2.h\left(\mathbf{W}_1.\mathbf{X}_1 + \mathbf{B}_1\right) + \mathbf{B}_2\right) + \mathbf{B}_3, \tag{3.8}$$

where $\mathbf{W}_1$ (7×3), $\mathbf{W}_2$ (7×7) and $\mathbf{W}_3$ (3×7) are arrays of network weights, while $\mathbf{B}_1$ (7×1), $\mathbf{B}_2$ (7×1), and $\mathbf{B}_3$ (3×1) are arrays of network biases. These are given in Table 3.8.

Figure 3.34 shows the training history of the ANN retained while Figures 3.35(a)–(c) compare the predictions of the ANN to the numerical data. The network trained achieves

Number of neurons in hidden layer 1	7	6	8	7	8	**7**	9	8
Number of neurons in hidden layer 2	5	6	5	6	6	**7**	6	7
Number of parameters	86	87	95	97	107	**108**	117	119
MSE train %	1.03	0.97	0.72	0.89	0.75	**0.30**	0.37	0.40
MSE test %	2.36	1.94	1.69	1.85	1.50	**0.56**	0.77	0.91
Overall MSE %	1.23	1.11	0.86	1.04	0.86	**0.34**	0.43	0.48

Table 3.7: Comparing the performances of a set of ANNs comprising two hidden layers and sigmoid activation functions.

$\mathbf{W}_1$ (7 × 3)			$\mathbf{B}_1$ (7 × 1)
0.19078	2.48667	-0.29024	-0.52860
0.53649	-0.45355	-0.54471	0.57214
4.54559	0.01049	-0.35217	4.75203
-0.37074	1.19430	-0.04487	0.80536
2.19032	0.69250	0.58383	1.85442
1.45889	0.47306	-0.09301	1.49059
0.00824	0.66284	1.32466	2.43609

$\mathbf{W}_2$ (7 × 7)							$\mathbf{B}_2$ (7 × 1)
-0.51759	1.67341	-2.58524	1.47152	-0.83477	0.58837	-2.58457	0.66612
3.85199	-1.75493	0.97955	-1.70748	0.18200	1.05788	0.19115	-1.42305
0.43406	1.96910	-0.06565	3.94725	0.38453	-4.87576	-2.83976	-0.40294
2.51191	-1.07348	0.40233	-0.73556	0.15677	0.30285	0.54688	2.26528
2.82577	-0.39264	-0.40345	1.25575	-1.13360	2.30234	-0.65178	0.71949
1.02441	-0.62178	0.34489	-0.39192	0.08891	0.10530	0.40625	1.34551
2.17814	-0.36821	-0.19223	1.14541	-1.44808	2.81217	1.83888	-2.56283

$\mathbf{W}_3$ (3 × 7)							$\mathbf{B}_3$ (3 × 1)
-0.27979	-0.08790	0.16081	1.04317	-1.15900	0.23001	1.08190	-0.33912
0.15093	-0.43170	-0.01331	-0.53831	-1.35681	3.44829	1.51845	-1.92848
-2.61750	-0.15213	1.77818	-0.57471	-0.11555	1.35046	0.21396	-1.14587

Table 3.8: Weights and biases of the data-driven ANN surrogate model for p_{avg}, $\hat{p}_{avg}$ and i_{avg}.

MREs of 0.58%, 0.45% and 0.38% over the datasets for p_{avg}, $\hat{p}_{avg}$ and i_{avg}, respectively. Figures 3.31–3.33 show the numerical dataset superimposed to the predictions of the ANN. The lines in magenta correspond to the ANN's predictions of p_{avg}, $\hat{p}_{avg}$ and i_{avg} for a normalized wave length $L_{dn} = 2.55$ (corresponding to a standoff distance $D = 100$ m), which are not included in the available dataset. The closeness between the predictions of the ANN and a couple of additional numerical solutions determined for verification with $L_{dn} = 2.55$ (which are represented by the markers in magenta) shows the possibility to determine rapid and computationally inexpensive estimates of p_{avg}, $\hat{p}_{avg}$ and i_{avg} in other configurations than those on which this data-driven surrogate model was trained.
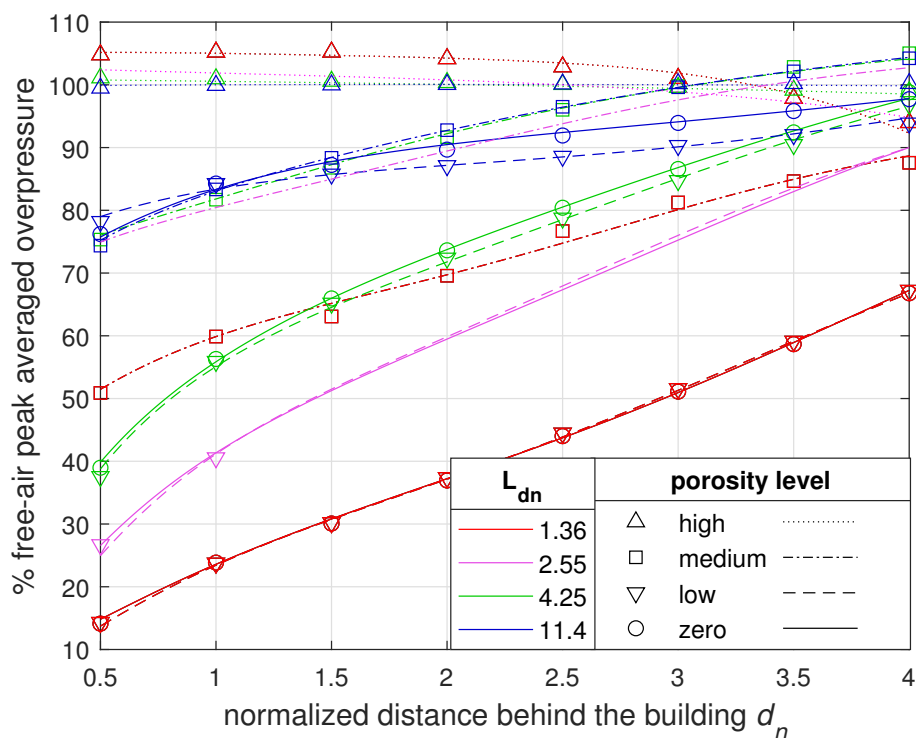
Figure 3.31: ANN predictions for p_{avg} superimposed to the scaled dataset. The additional data points in magenta were generated after the prediction for L_{dn} = 2.55.
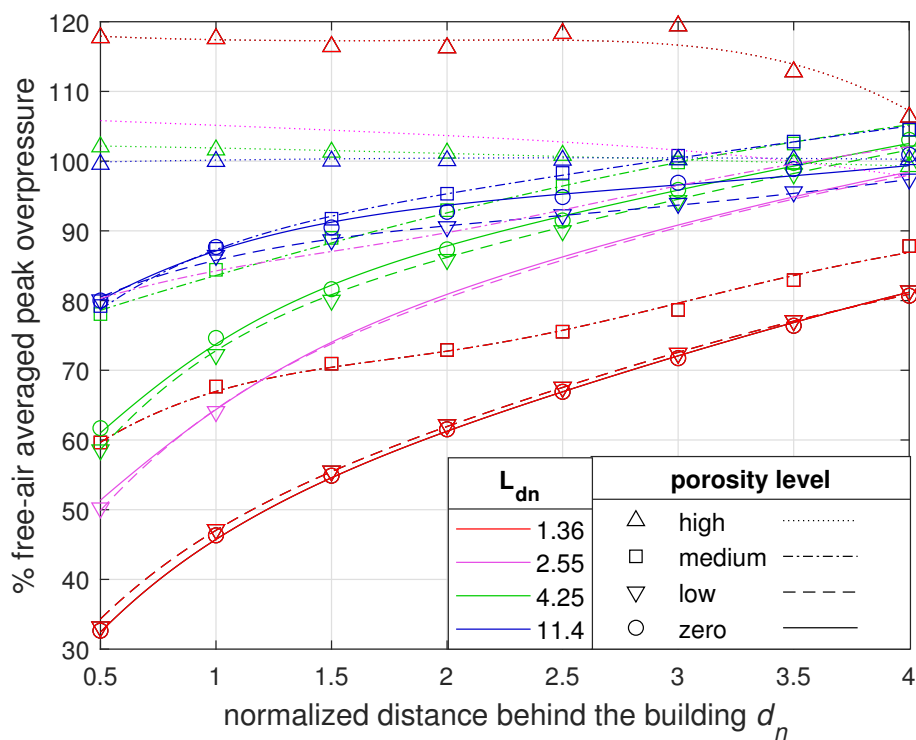
Figure 3.32: ANN predictions for $\hat{p}_{avg}$ superimposed to the scaled dataset. The additional data points in magenta were generated after the prediction for L_{dn} = 2.55.
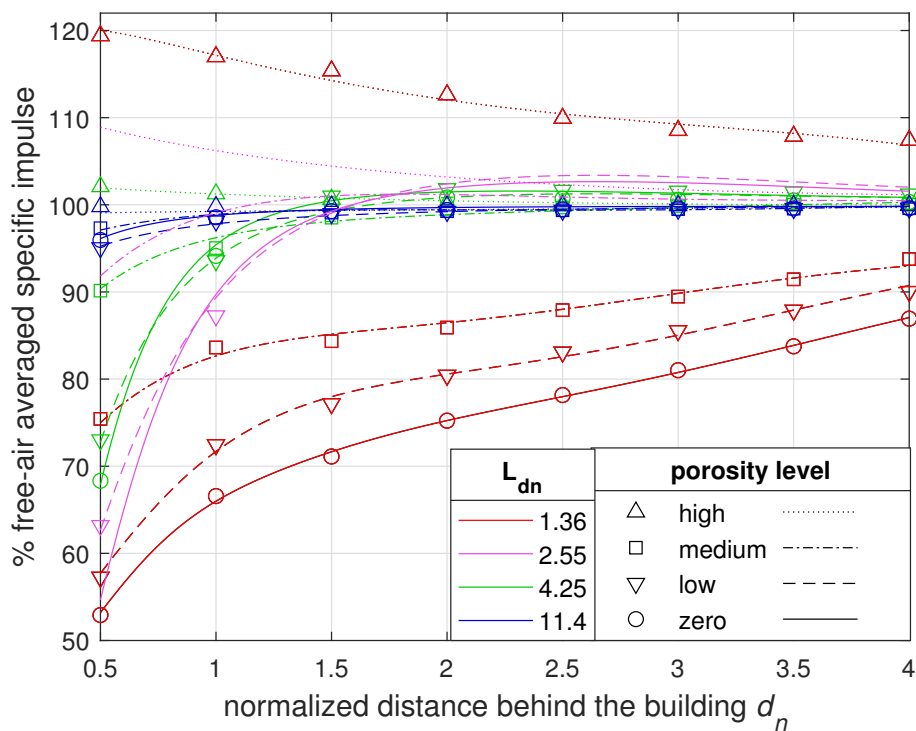
Figure 3.33: ANN predictions for i_{avg} superimposed to the scaled dataset. The additional data points in magenta were generated after the prediction for $L_{dn} = 2.55$.
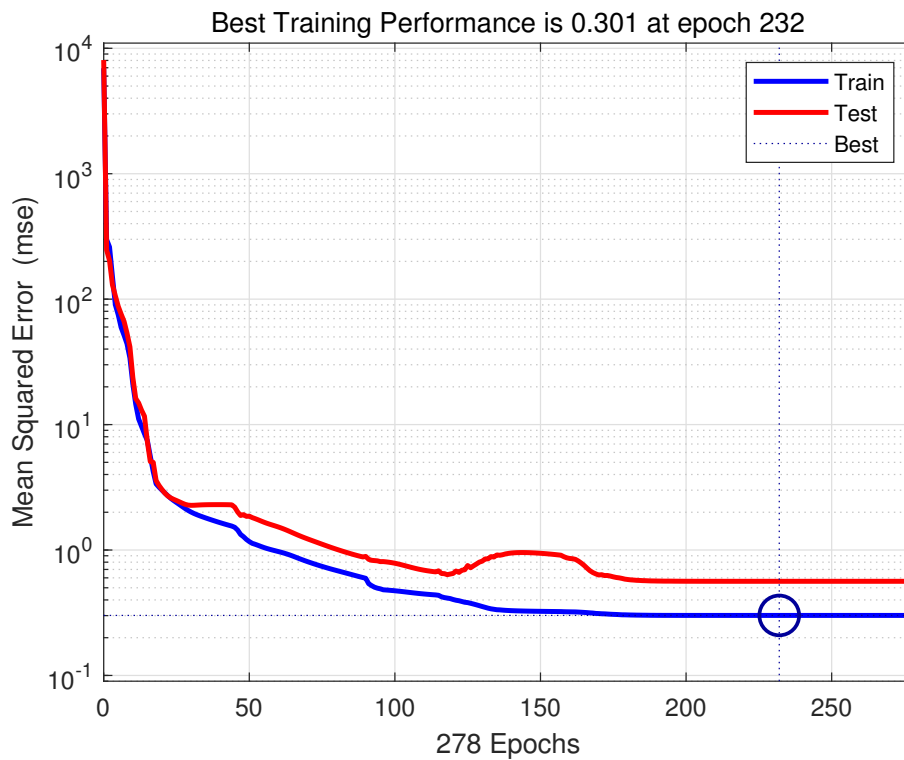
Figure 3.34: Training history of the ANN retained.
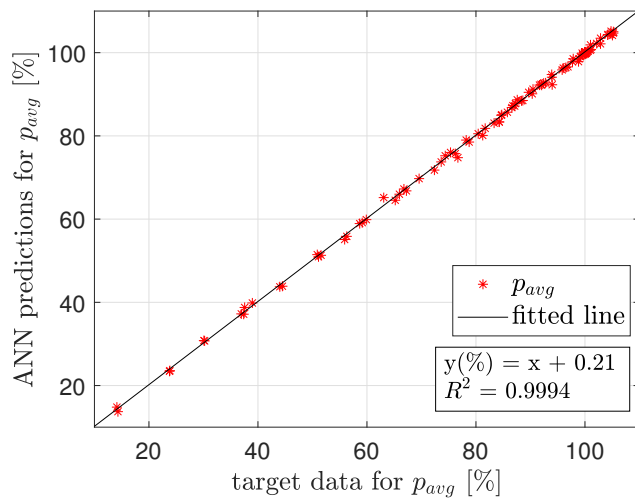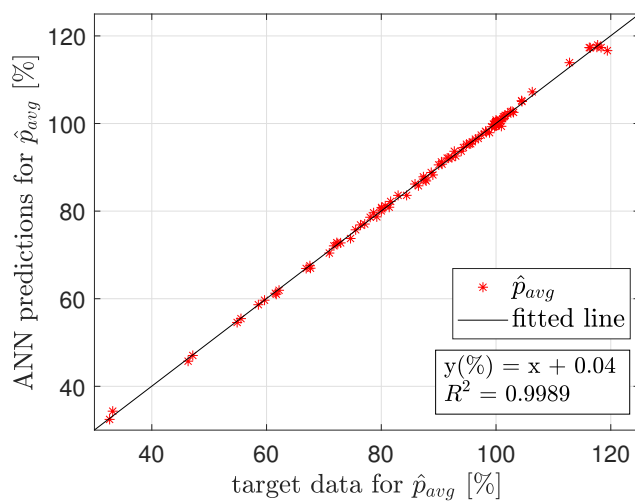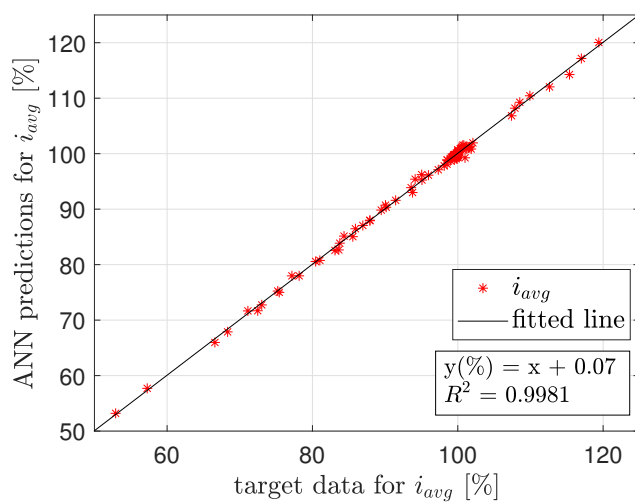
Figure 3.35: Regression of the ANN's predictions on the numerical data for (a) p_{avg}, (b) $\hat{p}_{avg}$ and (c) i_{avg}.

3.5 Conclusion

This study investigated the extent to which the porosity of a building can affect its capacity to shield other structures from a massive explosion, such as that which occurred on August 4, 2020, in the port of Beirut. To this aim, high-fidelity numerical simulations were designed and executed to determine the average incident overpressure and specific impulse developed over virtual facades shielded by buildings of typical porosity levels located at various standoff distances from a high-yield explosive charge. A valuable manifold of solutions was hence generated. This manifold mainly revealed that the effect of a building's porosity on its shielding potential can be substantial: for instance, in the near field (at $Z = 0.7$ m/kg$^{\frac{1}{3}}$), the peak facade-averaged overpressure behind a highly porous structure reaches up to seven times that behind a non-porous structure of the same size. It was also found that the shielding effect wanes with both: (i) increasing standoff and (ii) increasing distance behind the shielding structure. Overall, peak overpressure and specific impulse fall inside of envelopes delimited above by the high-porosity building and below by the zero or low-porosity building, depending on standoff. An internal channeling of the blast wave was observed inside of the high-porosity building, between the parallel slabs and side-walls, which led to an increased peak overpressure and impulse close-in behind the building. This phenomenon faded as the blast-wave became increasingly planar, in the far field. It was also noted that, in general, a lower building porosity results in the blast wave taking a longer path, which delays the rise to peak overpressure behind the building.

A suitable scaling was applied to the numerical datasets generated in this work, for broader impact. Soft computing techniques were applied to devise simple, computationally efficient and more general, data-driven, predictive tools. In particular, closed-form analytical expressions were fitted to the scaled data points, to facilitate their interpolation. An artificial neural network was also developed and trained successfully on the scaled dataset, to generate low-cost predictions corresponding to other explosive charges, standoffs, porosity levels and distances behind the shielding structure.

The outcomes of this work can provide some guidance to structural engineering prac-

titioners in estimating blast loads behind porous structures. However, these also reveal the complexity of the various phenomena taking place during the propagation of a blast wave inside and around a building. Many parameters, including the yield of the explosion, the external dimensions of the shielding structure, its standoff distance to the charge, the floor height, the properties of the internal partitioning (including density, distribution and orientation), the number of openings and their properties (including shape, size and location) contribute to determining the intensity of the blast wave behind the structure. Additional studies are thus needed to further the understanding of the influence that each parameter has on the shielding effect. This added knowledge would enable the development of more exhaustive surrogate models relating the influence of building porosity on the propagation of the blast wave. These could be incorporated subsequently into broader computational tools for the efficient prediction of blast loads on structures located in complex urban environments.
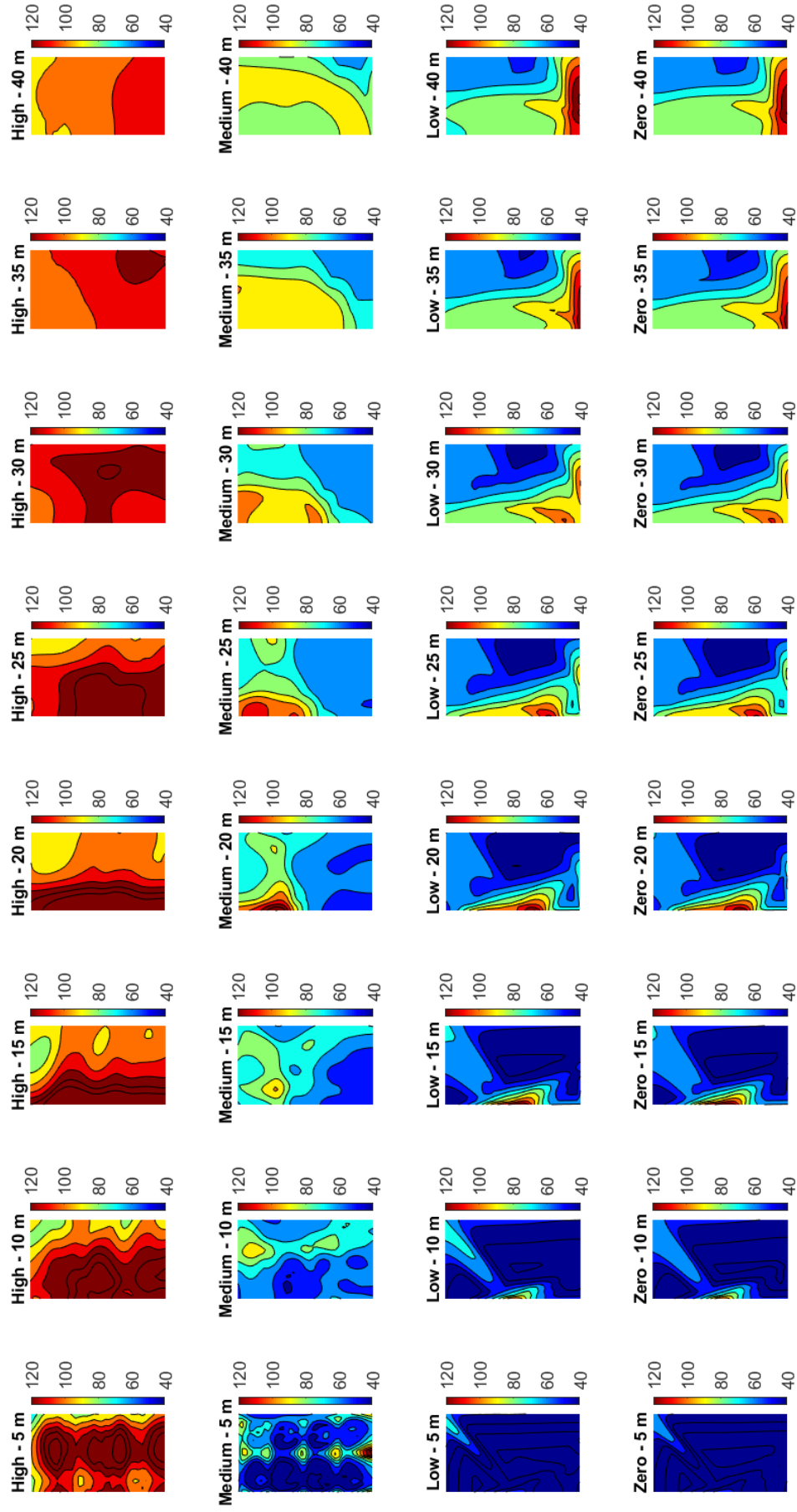
Figure 3.36: Contour plots of percent free-air peak overpressure over the virtual facades at $D = 50$ m.
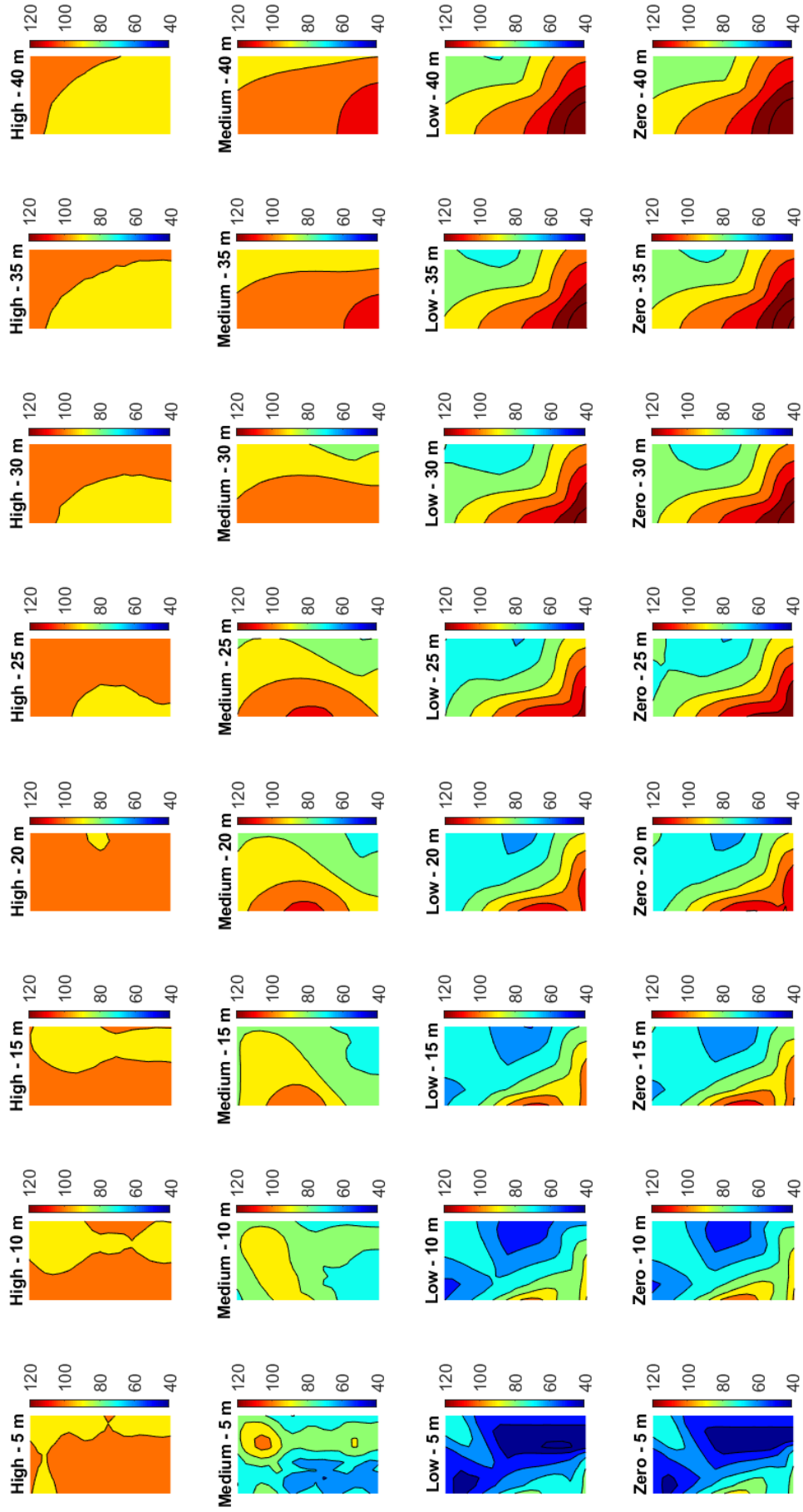
Figure 3.37: Contour plots of percent free-air peak overpressure over the virtual facades at $D = 150$ m.
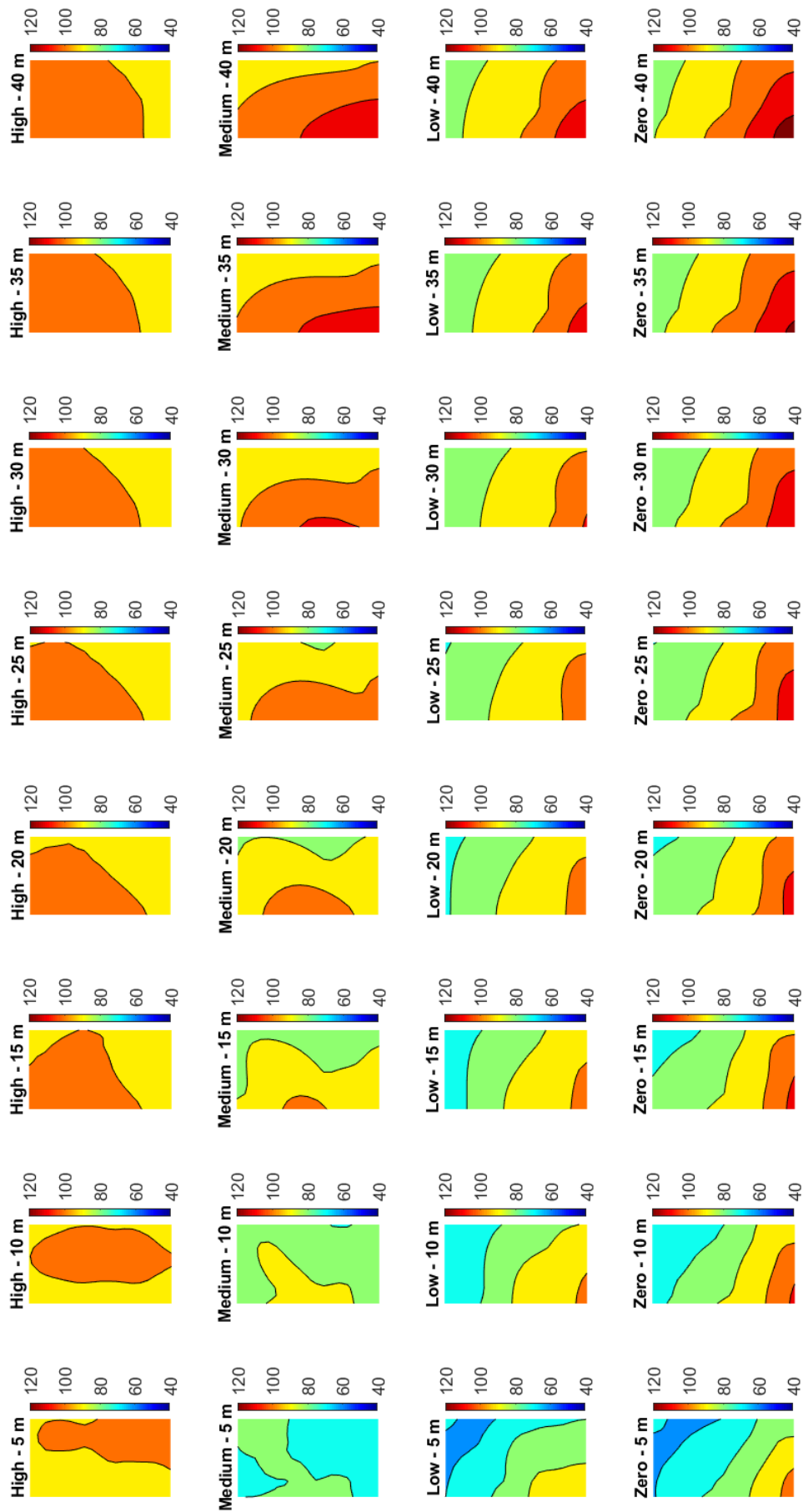
Figure 3.38: Contour plots of percent free-air peak overpressure over the virtual facades at $D = 450$ m.
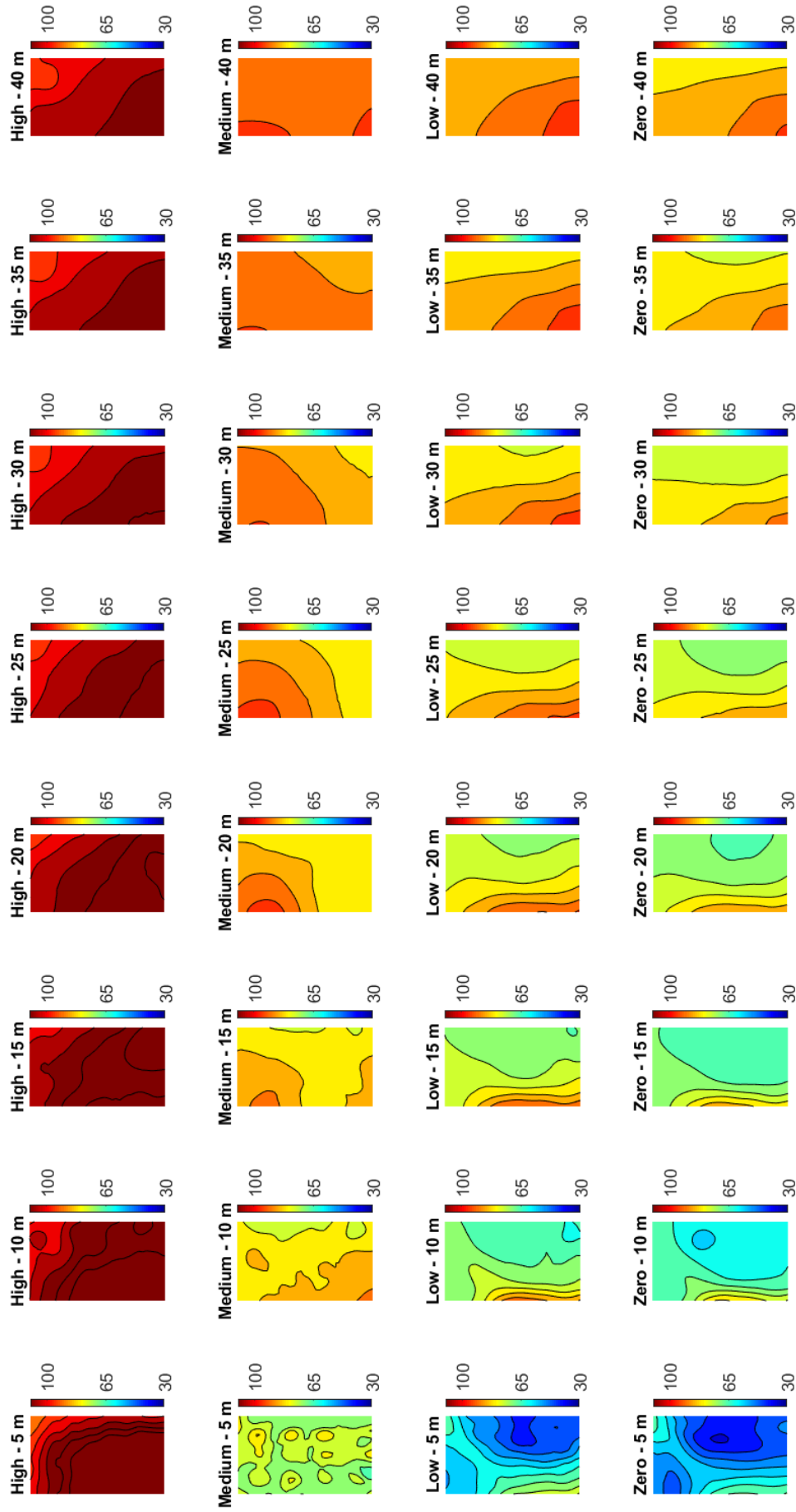
Figure 3.39: Contour plots of percent free-air specific impulse over the virtual facades at $D = 50$ m.

92
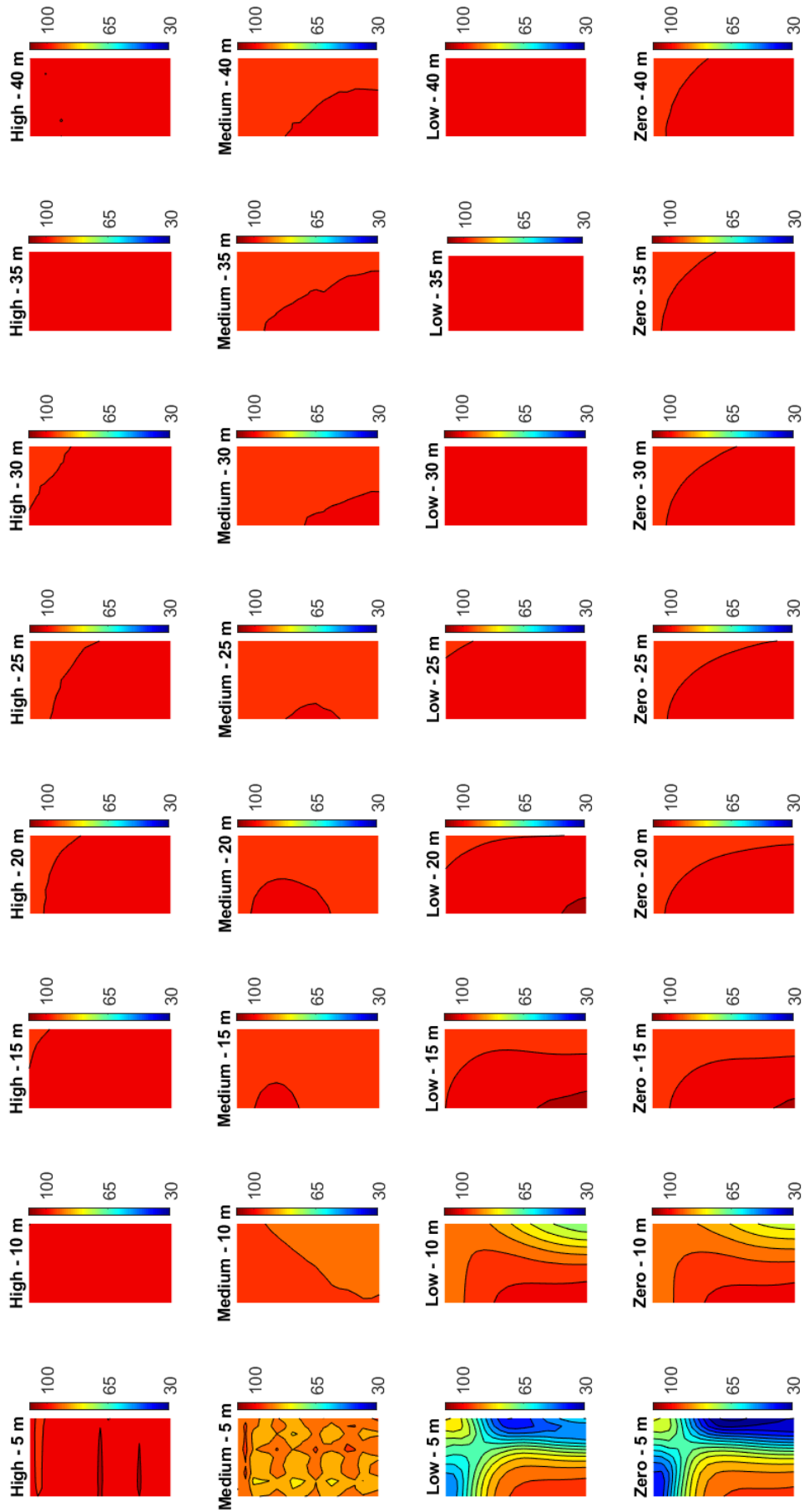
Figure 3.40: Contour plots of percent free-air specific impulse over the virtual facades at $D = 150$ m.

93
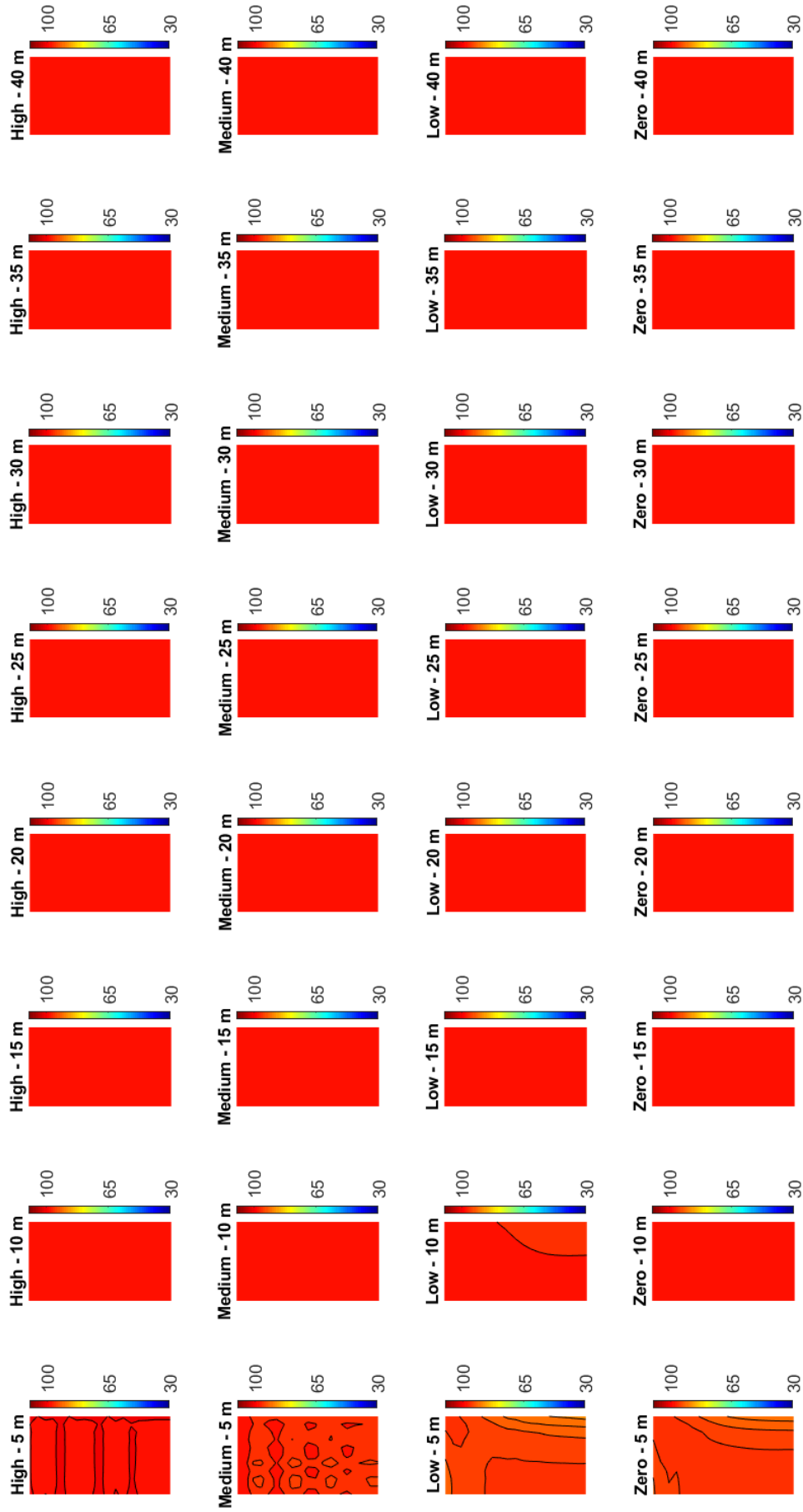
Figure 3.41: Contour plots of percent free-air specific impulse over the virtual facades at $D = 450$ m.

Near field $\left(D = 50 \text{ m}; Z = 0.7 \text{ m/kg}^{\frac{1}{3}} \right)$						
Porosity level		**Zero**	**Low**	**Medium**	**High**	**Free**
Distance d behind the building [m]	**5**	147.0	149.0	529.9	1091.1	1041.3
	10	215.1	214.4	540.2	949.2	902.1
	15	236.4	237.4	495.6	826.7	785.7
	20	254.0	257.1	478.4	716.2	687.6
	25	266.1	269.0	463.7	622.0	604.6
	30	273.0	275.5	434.0	539.6	534.1
	35	278.3	280.5	401.6	464.2	474.4
	40	282.9	284.8	370.9	398.1	423.6

Intermediate field $\left(D = 150 \text{ m}; Z = 2.2 \text{ m/kg}^{\frac{1}{3}} \right)$						
Porosity level		**Zero**	**Low**	**Medium**	**High**	**Free**
Distance d behind the building [m]	**5**	56.5	54.4	109.2	146.5	144.9
	10	76.4	75.8	110.8	137.0	135.7
	15	84.4	83.4	111.1	128.7	128.0
	20	89.0	87.5	110.8	121.3	120.9
	25	91.9	90.0	109.8	114.4	114.3
	30	93.8	91.8	108.1	107.9	108.3
	35	95.1	93.1	105.8	102.0	102.9
	40	96.4	94.5	102.5	96.5	97.5

Far field $\left(D = 450 \text{ m}; Z = 6.7 \text{ m/kg}^{\frac{1}{3}} \right)$						
Porosity level		**Zero**	**Low**	**Medium**	**High**	**Free**
Distance d behind the building [m]	**5**	19.7	20.2	19.2	25.7	25.8
	10	20.2	20.2	20.0	24.0	24.0
	15	20.5	20.1	20.8	23.5	23.5
	20	20.7	20.1	21.4	23.1	23.1
	25	20.8	20.1	21.9	22.7	22.7
	30	20.9	20.1	22.2	22.3	22.3
	35	21.0	20.2	22.4	22.0	22.0
	40	21.1	20.3	22.5	21.6	21.6

Table 3.9: Values of peak facade-averaged incident overpressure P_{avg} (in kPa), at distances d between 5 and 40 m behind shielding structures of various porosities located in the near, intermediate and far fields of a high-yield explosion.

Near field $\left(D = 50 \text{ m}; Z = 0.7 \text{ m/kg}^{\frac{1}{3}} \right)$						
Porosity level		**Zero**	**Low**	**Medium**	**High**	**Free**
Distance d behind the building [m]	**5**	389.4	395.9	711.6	1404.3	1193.0
	10	471.2	479.5	688.1	1195.8	1017.1
	15	478.1	483.9	618.1	1014.5	871.3
	20	462.1	466.9	547.5	873.0	751.0
	25	436.2	440.4	492.4	771.3	651.9
	30	408.8	412.8	448.3	680.5	569.9
	35	383.4	387.0	416.2	566.2	501.9
	40	359.4	362.5	391.1	473.5	445.4

Intermediate field $\left(D = 150 \text{ m}; Z = 2.2 \text{ m/kg}^{\frac{1}{3}} \right)$						
Porosity level		**Zero**	**Low**	**Medium**	**High**	**Free**
Distance d behind the building [m]	**5**	90.0	85.5	113.9	148.9	145.9
	10	101.7	98.4	115.0	138.4	136.2
	15	104.9	102.9	114.4	130.2	128.6
	20	106.1	104.3	112.9	122.9	121.5
	25	107.0	105.3	112.8	117.9	117.0
	30	106.3	104.6	110.7	111.1	110.9
	35	105.0	103.4	107.9	104.9	105.3
	40	103.5	101.9	104.9	99.6	100.4

Far field $\left(D = 450 \text{ m}; Z = 6.7 \text{ m/kg}^{\frac{1}{3}} \right)$						
Porosity level		**Zero**	**Low**	**Medium**	**High**	**Free**
Distance d behind the building [m]	**5**	20.7	20.7	20.5	25.8	25.9
	10	21.1	20.8	21.0	24.0	24.0
	15	21.3	20.8	21.6	23.5	23.5
	20	21.4	20.9	22.0	23.1	23.1
	25	21.5	20.9	22.3	22.7	22.7
	30	21.6	21.0	22.5	22.4	22.3
	35	21.7	21.0	22.6	22.0	22.0
	40	21.8	21.0	22.6	21.6	21.6

Table 3.10: Values of facade-averaged peak incident overpressure $\hat{P}_{avg}$ (in kPa), at distances d between 5 and 40 m behind shielding structures of various porosities located in the near, intermediate and far fields of a high-yield explosion.

Near field $\left(D = 50 \text{ m}; Z = 0.7 \text{ m/kg}^{\frac{1}{3}} \right)$						
Porosity level		**Zero**	**Low**	**Medium**	**High**	**Free**
Distance d behind the building [m]	**5**	6709.7	7260.3	9563.9	15139.5	12678.8
	10	7996.0	8704.4	10043.6	14052.7	12010.6
	15	8180.6	8877.3	9702.1	13271.2	11502.8
	20	8266.3	8839.0	9440.6	12375.4	10988.5
	25	8128.8	8641.6	9141.7	11431.1	10399.1
	30	8000.4	8448.4	8834.6	10717.2	9874.8
	35	7846.3	8234.4	8566.7	10104.3	9367.5
	40	7734.8	8012.2	8343.7	9555.6	8897.5

Intermediate field $\left(D = 150 \text{ m}; Z = 2.2 \text{ m/kg}^{\frac{1}{3}} \right)$						
Porosity level		**Zero**	**Low**	**Medium**	**High**	**Free**
Distance d behind the building [m]	**5**	4581.2	4896.0	6044.2	6844.3	6704.8
	10	6295.2	6258.2	6355.6	6771.8	6687.6
	15	6474.6	6532.3	6372.3	6509.1	6467.8
	20	6378.0	6441.6	6294.6	6341.8	6324.8
	25	6228.7	6288.1	6166.1	6192.1	6185.2
	30	6048.2	6107.2	6004.1	6017.7	6013.0
	35	5872.6	5928.9	5843.4	5846.2	5843.4
	40	5730.4	5782.0	5711.2	5712.5	5711.6

Far field $\left(D = 450 \text{ m}; Z = 6.7 \text{ m/kg}^{\frac{1}{3}} \right)$						
Porosity level		**Zero**	**Low**	**Medium**	**High**	**Free**
Distance d behind the building [m]	**5**	2872.0	2845.3	2912.4	2986.4	2992.9
	10	2878.7	2866.1	2877.6	2914.9	2920.5
	15	2914.0	2905.4	2909.3	2930.9	2935.5
	20	2845.2	2840.6	2841.6	2858.7	2862.5
	25	2774.4	2772.1	2772.1	2786.5	2789.6
	30	2765.3	2763.1	2763.6	2774.6	2777.3
	35	2694.6	2694.3	2693.9	2703.6	2705.9
	40	2624.3	2624.9	2624.4	2633.0	2634.9

Table 3.11: Values of the incident facade-averaged specific impulse I_{avg} (in kPa.ms), at distances d between 5 and 40 m behind shielding structures of various porosities located in the near, intermediate and far fields of a high-yield explosion.

Chapter 4

General conclusions and future work

High-cost high-fidelity numerical finite element simulations in the fields of computational heat conduction and computational fluid dynamics were utilized in this work, in combination with soft modeling techniques, to design fast, fairly precise and computationally efficient predictive tools for the prediction of key quantities of interest in two major areas of engineering.

Novel, accurate and computationally efficient predictive tools for the effective thermal conductivity of particulate composites, including the effects of particle contiguity and thermal contact resistance at the interface between phases, were developed in Chapter 2. These are mainly characterized by formulation simplicity and by prediction speed and accuracy over broad ranges of material properties and proportions. They can thus be readily incorporated to recursive, inverse resolution and/or optimization schemes that require the fast execution of a large number of forward simulations. The tools proposed in Chapter 2 of this work can hence be key in facilitating the design of novel, more efficient, more sustainable metamaterials with enhanced thermal properties and behaviors.

A detailed analysis of the effect of building porosity on the shielding of blast waves resulting from high-yield explosive charges was conducted in Chapter 3. Regression and machine learning techniques were applied to a manifold of solutions generated from validated high-fidelity numerical simulations to make swifter and cheaper predictions of the intensity of a blast wave behind a porous building. The work presented in Chapter 3 con-

stitutes a significant contribution to gradually developing the capacity to make fast and reliable predictions of blast loads in complex urban environments, taking into account the various governing parameters, including building porosity. This objective is key in facilitating the design of safer and more resilient cities, and the rapid evaluation of damage and planning of relief efforts in the aftermath of catastrophic explosions.

The practical performances of the simplified modeling approaches developed in this work can be illustrated by a few examples. For instance, the NC and the generalized TCG2 models proposed in Chapter 2, running on an Intel® Core™ i7-8665U CPU with 16 MB of cache memory and a clock speed of 2.11 GHz, can make predictions of the effective thermal conductivity of particulate composites with accuracies of about 0.7% and 4.5%, respectively, in a fraction of a millisecond only. This can be compared to the computational time needed to run one finite element simulation to determine the same, which is approximately 10 minutes using equivalent hardware. Also for instance, the intensity of a blast wave behind a porous building can be predicted by the artificial neural network devised in Chapter 3 with an accuracy of about 0.5% in a fraction of a millisecond only, while the time necessary to determine the same from a coupled Eulerian-Lagrangian simulation is typically measured in days.

The outcomes of the work presented in this thesis extend beyond the computational aspects that were previously highlighted here. The detailed analyses performed also resulted in interesting observations and valuable conclusions, which contribute to the improvement of our understanding of physical phenomena governing the thermal behavior of composites and the propagation of a blast wave in and around porous structures. For instance, fitting the TCG2 model (devised in Chapter 2) to experimental data in the literature revealed that the contact between inclusion particles is favored by more dispersed particle size distributions. Notable outcomes from Chapter 3 include the observed increase in the average shielding effect tighter behind a porous structure and as the latter is sited closer to the explosive charge. A lower porosity typically results in the blast wave taking a longer path, which delays the rise to peak overpressure behind the shielding structure. Some highly porous structures however can intensify the blast wave due to an internal

channeling effect taking place between parallel floor slabs and sidewalls.

Future work could be directed towards developing inverse problem resolution and optimization schemes incorporating the computational tools devised in Chapter 2 to determine the most suitable properties and proportions for the constituents of a projected composite, based on a target effective thermal conductivity. The pioneering study conducted in Chapter 3 should also be complemented by additional research work to determine both the distinct and combined effects of the various relevant parameters governing the shielding of blast waves by porous structures, such as the density and layout of internal partitions, the floor height, the layout, number, shape and size of openings, the building's envelope shape and dimensions, and the explosion yield. It is only then that a fully generalized and comprehensive data-driven surrogate model can be developed to make fast and accurate predictions of the intensity of blast loads behind any porous structure.

References

Agari, Y., & Uno, T. (1986). Estimation on thermal conductivities of filled polymers. *Journal of Applied Polymer Science*, *32*(7), 5705–5712. https://doi.org/10.1002/app.1986.070320702

Aouad, C. J., Chemissany, W., Mazzali, P., Temsah, Y., & Jahami, A. (2021). Beirut explosion: TNT equivalence from the fireball evolution in the first 170 milliseconds. *Shock Waves*, *31*(8), 813–827. https://doi.org/10.1007/s00193-021-01031-9

Assaad, J., Chakar, E., & Zéhil, G.-P. (2018). Testing and modeling the behavior of sandwich lightweight panels against wind and seismic loads. *Engineering Structures*, *175*, 457–466. https://doi.org/10.1016/j.engstruct.2018.08.041

Awad, M., & Khanna, R. (2015a). Deep neural networks. *Efficient learning machines: Theories, concepts, and applications for engineers and system designers* (pp. 127–147). Apress. https://doi.org/10.1007/978-1-4302-5990-9_7

Awad, M., & Khanna, R. (2015b). Support vector regression. *Efficient learning machines: Theories, concepts, and applications for engineers and system designers* (pp. 67–80). Apress. https://doi.org/10.1007/978-1-4302-5990-9_4

Bae, J.-W., Kim, W., Cho, S.-H., & Lee, S.-H. (2000). The properties of AlN-filled epoxy molding compounds by the effects of filler size distribution. *Journal of materials science*, *35*(23), 5907–5913. https://doi.org/10.1023/A:1026741300020

Berger, M. J., & Oliger, J. (1984). Adaptive mesh refinement for hyperbolic partial differential equations. *Journal of Computational Physics*, *53*(3), 484–512. https://doi.org/10.1016/0021-9991(84)90073-1

Borgonovo, E., & Plischke, E. (2016). Sensitivity analysis: A review of recent advances. *European Journal of Operational Research*, *248*(3), 869–887. https://doi.org/10.1016/j.ejor.2015.06.032

Boudenne, A., Ibos, L., Fois, M., Gehin, E., & Majeste, J.-C. (2004). Thermophysical properties of polypropylene/aluminum composites. *Journal of Polymer Science Part B: Polymer Physics*, *42*(4), 722–732. https://doi.org/10.1002/polb.10713

Brode, H. L. (1955). Numerical solutions of spherical blast waves. *Journal of Applied Physics*, *26*(6), 766–775. https://doi.org/10.1063/1.1722085

Carson, J. K., Lovatt, S. J., Tanner, D. J., & Cleland, A. C. (2005). Thermal conductivity bounds for isotropic, porous materials. *International Journal of Heat and Mass Transfer*, *48*(11), 2150–2158. https://doi.org/10.1016/j.ijheatmasstransfer.2004.12.032

Chen, H., Ginzburg, V. V., Yang, J., Yang, Y., Liu, W., Huang, Y., Du, L., & Chen, B. (2016). Thermal conductivity of polymer-based composites: Fundamentals and applications [Topical Volume Hybrids]. *Progress in Polymer Science*, *59*, 41–85. https://doi.org/10.1016/j.progpolymsci.2016.03.001

Chen, M., Buckmaster, J., Jackson, T., & Massa, L. (2002). Homogenization issues and the combustion of heterogeneous solid propellants. *Proceedings of the Combustion Institute*, *29*(2), 2923–2929. https://doi.org/10.1016/S1540-7489(02)80357-1

Chinesta, F., Ladeveze, P., & Cueto, E. (2011). A short review on model order reduction based on proper generalized decomposition. *Archives of Computational Methods in Engineering*, *18*(4), 395. https://doi.org/10.1007/s11831-011-9064-7

Deissler, R. G., & Boegli, J. S. (1958). An investigation of effective thermal conductivities of powders in various gases. *Transactions of the ASME*, *80*, 1417–1425.

Dennis, A. A., Pannell, J. J., Smyl, D. J., & Rigby, S. E. (2021). Prediction of blast loading in an internal environment using artificial neural networks. *International Journal of Protective Structures*, *12*(3), 287–314. https://doi.org/10.1177/2041419620970570

Dewey, J. M. (2021). The TNT and ANFO equivalences of the Beirut explosion. *Shock Waves*, *31*, 95–99. https://doi.org/10.1007/s00193-021-00992-1

Dib, N., & Zéhil, G.-P. (2021). Generalized modeling of the effective thermal conductivity of particulate composites. *Materials Today Communications*, *27*, 102283. https://doi.org/10.1016/j.mtcomm.2021.102283

Drazin, W. (2018). *Blast propagation and damage in urban topographies* (Doctoral dissertation). University of Cambridge. https://doi.org/10.17863/CAM.22051

Fang, W.-Z., Zhang, H., Chen, L., & Tao, W.-Q. (2017). Numerical predictions of thermal conductivities for the silica aerogel and its composites. *Applied Thermal Engineering*, *115*, 1277–1286. https://doi.org/10.1016/j.applthermaleng.2016.10.184

Gan, K., Brewer, T., Pope, D., & Rigby, S. (2022). Probabilistic analysis of blast–obstacle interaction in a crowded internal environment. *Probabilistic Engineering Mechanics*, *68*, 103227. https://doi.org/10.1016/j.probengmech.2022.103227

Gao, B., Xu, J., Peng, J., Kang, F., Du, H., Li, J., Chiang, S., Xu, C., Hu, N., & Ning, X. (2015). Experimental and theoretical studies of effective thermal conductivity of composites made of silicone rubber and Al_2O_3 particles. *Thermochimica Acta*, *614*, 1–8. https://doi.org/10.1016/j.tca.2015.06.005

Geng, J., & Thomas, J. K. (2020). Diffracted blast loads behind structures. *4: Fluid-Structure Interaction*. https://doi.org/10.1115/PVP2020-21514

Ghnatios, C., Zéhil, G.-P., & Habchi, C. (2021). Modeling of the vane test using a power-law fluid and model order reduction techniques: Application to the identification of cement paste properties. *Comptes Rendus. Mécanique*, *349*(3), 501–517. https://doi.org/10.5802/crmeca.97

Giam, A., Toh, W., & Tan, V. B. C. (2020). Numerical review of Jones–Wilkins–Lee parameters for trinitrotoluene explosive in free-air blast. *Journal of Applied Mechanics*, *87*(5), 051008. https://doi.org/10.1115/1.4046243

Gilbert F., K., & Kenneth J., G. (1985). *Explosive shocks in air*. Springer-Verlag Berlin Heidelberg. https://doi.org/10.1007/978-3-642-86682-1

Gong, L., Wang, Y., Cheng, X., Zhang, R., & Zhang, H. (2014). A novel effective medium theory for modelling the thermal conductivity of porous materials. *International Journal of Heat and Mass Transfer*, *68*, 295–298. https://doi.org/10.1016/j.ijheatmasstransfer.2013.09.043

Hasselman, D., & Johnson, L. F. (1987). Effective thermal conductivity of composites with interfacial thermal barrier resistance. *Journal of Composite Materials*, *21*(6), 508–515. https://doi.org/10.1177/002199838702100602

He, J., Wang, H., Qu, Q., Su, Z., Qin, T., Da, Y., & Tian, X. (2020). Construction of interconnected SiC particles attached rGO structure in epoxy composites to achieve significant thermal conductivity enhancement. *Materials Today Communications*, *25*, 101584. https://doi.org/10.1016/j.mtcomm.2020.101584

Himo, R., Zéhil, G.-P., & Ghnatios, C. (2019). 2D modeling of the thermal conductivity of XLPE-modified concrete. *Congrès Français de Thermique*. https://hal.archives-ouvertes.fr/hal-02482365

Hsu, C. T., Cheng, P., & Wong, K. W. (1995). A Lumped-Parameter Model for Stagnant Thermal Conductivity of Spatially Periodic Porous Media. *Journal of Heat Transfer*, *117*(2), 264–269. https://doi.org/10.1115/1.2822515

Huang, P., & Zhang, J. (2015). Facts related to August 12, 2015 explosion accident in Tianjin, China. *Process Safety Progress*, *34*(4), 313–314. https://doi.org/10.1002/prs.11789

Hyde, D. W. (1988). *Microcomputer programs CONWEP and FUNPRO, applications of TM 5-855-1, fundamentals of protective design for conventional weapons (user's guide)* (tech. rep.). Army engineer waterways experiment station Vicksburg MS structures lab.

Jin, Z., Chen, X., Wang, Y., & Wang, D. (2015). Thermal conductivity of PTFE composites filled with graphite particles and carbon fibers. *Computational Materials Science*, *102*, 45–50. https://doi.org/10.1016/j.commatsci.2015.02.019

Jolliffe, I. T., & Cadima, J. (2016). Principal component analysis: A review and recent developments. *Philosophical Transactions of the Royal Society A: Mathematical, Physical and Engineering Sciences*, *374*(2065), 20150202. https://doi.org/10.1098/rsta.2015.0202

Kambouchev, N., Noels, L., & Radovitzky, R. (2007). Numerical simulation of the fluid–structure interaction between air blast waves and free-standing plates [Fourth MIT Conference on Computational Fluid and Solid Mechanics]. *Computers and Structures*, *85*(11), 923–931. https://doi.org/10.1016/j.compstruc.2006.11.005

Khan, K. A., Hajeri, F. A., & Khan, M. A. (2019). Analytical and numerical assessment of the effect of highly conductive inclusions distribution on the thermal conductivity of particulate composites. *Journal of Composite Materials*, *53*(25), 3499–3514. https://doi.org/10.1177/0021998319843329

Khoury, N., Maalouf, Y., Ghanimeh, S., & Zéhil, G.-P. (2016). Computer-aided measurements of the electrical resistivity fields in concrete mixtures with and without polyethylene terephthalate. *2016 3rd International Conference on Advances in Computational Tools for Engineering Applications (ACTEA)*, 67–71. https://doi.org/10.1109/ACTEA.2016.7560114

Kim, W., Taya, M., & Nguyen, M. (2009). Electrical and thermal conductivities of a silver flake/thermosetting polymer matrix composite [The Special Issue in Honor of Leon M. Keer]. *Mechanics of Materials*, *41*(10), 1116–1124. https://doi.org/10.1016/j.mechmat.2009.05.009

Kingery, C. N., & Bulmash, G. (1984). *Airblast parameters from spherical air burst and hemispherical surface burst*. US Army Armament; Development Center, Ballistic Research Laboratory.

Koo, S., Shin, D., & Kim, C. (2021). Application of principal component analysis approach to predict shear strength of reinforced concrete beams with stirrups. *Materials*, *14*(13). https://doi.org/10.3390/ma14133471

Krupa, I., & Chodák, I. (2001). Physical properties of thermoplastic/graphite composites. *European Polymer Journal*, *37*(11), 2159–2168. https://doi.org/10.1016/S0014-3057(01)00115-X

Landauer, R. (1952). The electrical resistance of binary metallic mixtures. *Journal of Applied Physics*, *23*(7), 779–784. https://doi.org/10.1063/1.1702301

Lee, E. L., Hornig, H. C., & Kury, J. W. (1968). *Adiabatic expansion of high explosive detonation products* (tech. rep.). University of California – Lawrence Radiation Laboratory. https://doi.org/10.2172/4783904

Levy, F. (1981). A modified Maxwell-Eucken equation for calculating the thermal conductivity of two-component solutions or mixtures. *International Journal of Refrigeration*, *4*(4), 223–225. https://doi.org/10.1016/0140-7007(81)90053-0

Li, W., Bazant, M. Z., & Zhu, J. (2021). A physics-guided neural network framework for elastic plates: Comparison of governing equations-based and energy-based approaches. *Computer Methods in Applied Mechanics and Engineering*, *383*, 113933. https://doi.org/10.1016/j.cma.2021.113933

Lord Rayleigh, S. R. (1892). Lvi. on the influence of obstacles arranged in rectangular order upon the properties of a medium. *The London, Edinburgh, and Dublin Philosophical Magazine and Journal of Science*, *34*(211), 481–502. https://doi.org/10.1080/14786449208620364

Ma, Y., Yu, B., Zhang, D., & Zou, M. (2003). A self-similarity model for effective thermal conductivity of porous media. *Journal of Physics D: Applied Physics*, *36*(17), 2157–2164. https://doi.org/10.1088%2F0022-3727%2F36%2F17%2F321

Matar, P., & Zéhil, G.-P. (2019). Effects of polypropylene fibers on the physical and mechanical properties of recycled aggregate concrete. *Journal of Wuhan University of Technology-Mater. Sci. Ed.*, *34*(6), 1327–1344. https://doi.org/10.1007/s11595-019-2196-6

Maxwell, J. (1954). *A treatise on electricity and magnetism*. Dover Publications Inc.

Nan, C.-W., Birringer, R., Clarke, D. R., & Gleiter, H. (1997). Effective thermal conductivity of particulate composites with interfacial thermal resistance. *Journal of Applied Physics*, *81*(10), 6692–6699. https://doi.org/10.1063/1.365209

Pannell, J., Rigby, S., Panoutsos, G., Tyas, A., SB, C., & Pope, D. (2019). Predicting near-field specific impulse distributions using machine learning. *Proceedings of The 18th International Symposium for the Interaction of Munitions with Structures (18th ISIEMS)*.

Parrish, M., Borden, M., Staten, M., & Benzley, S. (2008). A selective approach to conformal refinement of unstructured hexahedral finite element meshes. In M. L. Brewer & D. Marcum (Eds.), *Proceedings of the 16th international meshing roundtable* (pp. 251–268). Springer Berlin Heidelberg. https://doi.org/10.1007/978-3-540-75103-8_15

Pasolli, L., Notarnicola, C., & Bruzzone, L. (2011). Estimating soil moisture with the support vector regression technique. *IEEE Geoscience and Remote Sensing Letters*, *8*(6), 1080–1084. https://doi.org/10.1109/LGRS.2011.2156759

Ram, O., Nof, E., & Sadot, O. (2016). Dependence of the blast load penetrating into a structure on initial conditions and internal geometry. *Experimental Thermal and Fluid Science*, *78*, 65–74. https://doi.org/10.1016/j.expthermflusci.2016.05.012

Ram, O., & Sadot, O. (2015). Analysis of the pressure buildup behind rigid porous media impinged by shock waves in time and frequency domains. *Journal of Fluid Mechanics*, *779*, 842–858. https://doi.org/10.1017/jfm.2015.463

Remennikov, A. M., & Rose, T. A. (2005). Modelling blast loads on buildings in complex city geometries. *Computers and Structures*, *83*(27), 2197–2205. https://doi.org/10.1016/j.compstruc.2005.04.003

Rigby, S. E., & Gitterman, Y. (2016). Secondary shock delay measurements from explosive trials. *24th Military aspects of blast and shock*.

Rigby, S. E., Lodge, T. J., Alotaibi, S., Barr, A. D., Clarke, S. D., Langdon, G. S., & Tyas, A. (2020). Preliminary yield estimation of the 2020 Beirut explosion using video footage from social media. *Shock Waves*, *30*, 671–675. https://doi.org/10.1007/s00193-020-00970-z

Rigby, S. E., & Sielicki, P. W. (2015). An investigation of TNT equivalence of hemispherical PE4 charges. *Engineering Transactions*, *62*(4). https://et.ippt.gov.pl/index.php/et/article/view/266

Rong, Q., Wei, H., Huang, X., & Bao, H. (2019). Predicting the effective thermal conductivity of composites from cross sections images using deep learning methods. *Composites Science and Technology*, *184*, 107861. https://doi.org/10.1016/j.compscitech.2019.107861

Rose, T., & Smith, P. (2002). Influence of the principal geometrical parameters of straight city streets on positive and negative phase blast wave impulses. *International Journal of Impact Engineering*, *27*(4), 359–376. https://doi.org/10.1016/S0734-743X(01)00060-4

Shahmansouri, A. A., Yazdani, M., Ghanbari, S., Akbarzadeh Bengar, H., Jafari, A., & Farrokh Ghatte, H. (2021). Artificial neural network model to predict the compressive strength of eco-friendly geopolymer concrete incorporating silica fume and natural zeolite. *Journal of Cleaner Production*, *279*, 123697. https://doi.org/10.1016/j.jclepro.2020.123697

Shin, J., Whittaker, A. S., & Cormie, D. (2015). Incident and normally reflected overpressure and impulse for detonations of spherical high explosives in free air. *Journal of Structural Engineering*, *141*(12), 04015057. https://doi.org/10.1061/(ASCE)ST.1943-541X.0001305

Smith, M. (2009). *Abaqus/standard user's manual, version 6.9*. Dassault Systèmes Simulia Corp.

Smith, P. D., Rose, T. A., Krahe, S. L., & Franks, M. A. (2003). Façade failure effects on blast propagation along city streets. *Proceedings of the Institution of Civil Engineers - Structures and Buildings*, *156*(4), 359–365. https://doi.org/10.1680/stbu.2003.156.4.359

Smith, P. D., Rose, T. A., & Ng, S. H. (2004). The influence of areal density on the shielding and channelling of blast by buildings. *18th International Symposium on Military Aspects of Blast and Shock. Bad Reichenhall, Germany 27th September-1st October.*

Subramaniam, K. V., Nian, W., & Andreopoulos, Y. (2009). Blast response simulation of an elastic structure: Evaluation of the fluid–structure interaction effect. *International Journal of Impact Engineering*, *36*(7), 965–974. https://doi.org/10.1016/j.ijimpeng.2009.01.001

Sundstrom, D. W., & Lee, Y.-D. (1972). Thermal conductivity of polymers filled with particulate solids. *Journal of Applied Polymer Science*, *16*(12), 3159–3167. https://doi.org/10.1002/app.1972.070161210

Tekce, H. S., Kumlutas, D., & Tavman, I. H. (2007). Effect of particle shape on thermal conductivity of copper reinforced polymer composites. *Journal of Reinforced Plastics and Composites*, *26*(1), 113–121. https://doi.org/10.1177/0731684407072522

Temsah, Y., Jahami, A., & Aouad, C. (2021). Silos structural response to blast loading. *Engineering Structures*, *243*, 112671. https://doi.org/10.1016/j.engstruct.2021.112671

TM5-1300. (1990). *Structures to resist the effects of accidental explosions*. Department of the Army, Washington DC, USA.

Tyas, A., Warren, J. A., Bennett, T., & Fay, S. (2011). Prediction of clearing effects in far-field blast loading of finite targets. *Shock Waves*, *21*, 111–119. https://doi.org/10.1007/s00193-011-0308-0

USDOE. (1980). *Manual for the prediction of blast and fragment loadings on structures* (tech. rep.). USDOE Albuquerque Operations Office, NM; Southwest Research Inst., San Antonio, TX. https://doi.org/10.2172/5892901

Wang, J., Carson, J. K., North, M. F., & Cleland, D. J. (2006). A new approach to modelling the effective thermal conductivity of heterogeneous materials. *International Journal of Heat and Mass Transfer*, *49*(17), 3075–3083. https://doi.org/10.1016/j.ijheatmasstransfer.2006.02.007

Wang, J., Carson, J. K., North, M. F., & Cleland, D. J. (2008). A new structural model of effective thermal conductivity for heterogeneous materials with co-continuous phases. *International Journal of Heat and Mass Transfer*, *51*(9), 2389–2397. https://doi.org/10.1016/j.ijheatmasstransfer.2007.08.028

Wang, M., & Pan, N. (2008). Predictions of effective physical properties of complex multiphase materials. *Materials Science and Engineering: R: Reports*, *63*(1), 1–30. https://doi.org/10.1016/j.mser.2008.07.001

Weidenfeller, B., Höfer, M., & Schilling, F. R. (2004). Thermal conductivity, thermal diffusivity, and specific heat capacity of particle filled polypropylene. *Composites Part A: Applied Science and Manufacturing*, *35*(4), 423–429. https://doi.org/10.1016/j.compositesa.2003.11.005

Xu, J., Gao, B., Du, H., & Kang, F. (2016a). A statistical model for effective thermal conductivity of composite materials. *International Journal of Thermal Sciences*, *104*, 348–356. https://doi.org/10.1016/j.ijthermalsci.2015.12.023

Xu, J., Gao, B., & Kang, F. (2016b). A reconstruction of Maxwell model for effective thermal conductivity of composite materials. *Applied Thermal Engineering*, *102*, 972–979. https://doi.org/10.1016/j.applthermaleng.2016.03.155

Yan, B., Cheng, L., Li, B., Liu, P., Wang, X., Gao, R., Yang, Z., Xu, S., Ding, X., & Zhang, P. (2020). Bi-directional prediction of structural characteristics and effective thermal conductivities of composite fuels through learning from finite element simulation results. *Materials and Design*, *189*, 108483. https://doi.org/10.1016/j.matdes.2020.108483

Yang, W., Peng, K., Zhou, L., Zhu, J., & Li, D. (2014). Finite element simulation and experimental investigation on thermal conductivity of diamond/aluminium composites with imperfect interface. *Computational Materials Science*, *83*, 375–380. https://doi.org/10.1016/j.commatsci.2013.11.059

Zéhil, G.-P. (2016). A combined analytical and computational approach to the structural behavior of composite tubes. *2016 3rd International Conference on Advances in Computational Tools for Engineering Applications (ACTEA)*, 146–151. https://doi.org/10.1109/ACTEA.2016.7560129

Zéhil, G.-P. (2019). Efficient modeling of the thermal-cracking of a cylindrical shell encapsulating a cylinder inclusion. *2019 Fourth International Conference on Advances in Computational Tools for Engineering Applications (ACTEA)*, 1–6. https://doi.org/10.1109/ACTEA.2019.8851113

Zéhil, G.-P. (2020). Efficient modeling of the thermal-cracking of a spherical shell encapsulating a round inclusion. *Frontiers of Composite Materials IV*, *995*, 214–221. https://doi.org/10.4028/www.scientific.net/MSF.995.214

Zéhil, G.-P., & Assaad, J. J. (2019). Feasibility of concrete mixtures containing cross-linked polyethylene waste materials. *Construction and Building Materials*, *226*, 1–10. https://doi.org/10.1016/j.conbuildmat.2019.07.285

Zéhil, G.-P., & Gavin, H. P. (2013a). Simple algorithms for solving steady-state frictional rolling contact problems in two and three dimensions. *International Journal of Solids and Structures*, *50*(6), 843–852. https://doi.org/10.1016/j.ijsolstr.2012.11.021

Zéhil, G.-P., & Gavin, H. P. (2013b). Simplified approaches to viscoelastic rolling resistance. *International Journal of Solids and Structures*, *50*(6), 853–862. https://doi.org/10.1016/j.ijsolstr.2012.09.025

Zéhil, G.-P., & Gavin, H. P. (2013c). Three-dimensional boundary element formulation of an incompressible viscoelastic layer of finite thickness applied to the rolling resistance of a rigid sphere. *International Journal of Solids and Structures*, *50*(6), 833–842. https://doi.org/10.1016/j.ijsolstr.2012.11.020

Zéhil, G.-P., & Gavin, H. P. (2014a). Rolling resistance of a rigid sphere with viscoelastic coatings. *International Journal of Solids and Structures*, *51*(3), 822–838. https://doi.org/10.1016/j.ijsolstr.2013.11.009

Zéhil, G.-P., & Gavin, H. P. (2014b). Two and three-dimensional boundary element formulations of compressible isotropic, transversely isotropic and orthotropic viscoelastic layers of arbitrary thickness, applied to the rolling resistance of rigid cylinders and spheres. *European Journal of Mechanics - A/Solids*, *44*, 175–187. https://doi.org/10.1016/j.euromechsol.2013.10.015

Zéhil, G.-P., Ghnatios, C., & Himo, R. (2020). Soft computing approaches to homogenized properties of inclusion-modified concrete mixtures: Application to xlpe-modified concrete. *Journal of Building Engineering*, *29*, 101161. https://doi.org/10.1016/j.jobe.2019.101161

Zéhil, G.-P., & Saba, D. (2018). Exploring XLPE-concrete as a novel sustainable construction material. *AIP Conference Proceedings*, *2004*(1), 030005. https://doi.org/10.1063/1.5051105

Zhang, H., Fang, W.-Z., Li, Y.-M., & Tao, W.-Q. (2017). Experimental study of the thermal conductivity of polyurethane foams. *Applied Thermal Engineering*, *115*, 528–538. https://doi.org/10.1016/j.applthermaleng.2016.12.057

Zhang, R., Liu, Y., & Sun, H. (2020). Physics-guided convolutional neural network (phycnn) for data-driven seismic response modeling. *Engineering Structures*, *215*, 110704. https://doi.org/10.1016/j.engstruct.2020.110704

Zhou, F., & Cheng, G. (2014). Lattice boltzmann model for predicting effective thermal conductivity of composite with randomly distributed particles: Considering effect of interactions between particles and matrix. *Computational Materials Science*, *92*, 157–165. https://doi.org/10.1016/j.commatsci.2014.05.039

Zhou, W., Qi, S., Li, H., & Shao, S. (2007a). Study on insulating thermal conductive BN/HDPE composites. *Thermochimica Acta*, *452*(1), 36–42. https://doi.org/10.1016/j.tca.2006.10.018

Zhou, W., Qi, S., Tu, C., Zhao, H., Wang, C., & Kou, J. (2007b). Effect of the particle size of Al_2O_3 on the properties of filled heat-conductive silicone rubber. *Journal of Applied Polymer Science*, *104*(2), 1312–1318. https://doi.org/10.1002/app.25789

Zhu, H., & Menq, C. (2002). B-rep model simplification by automatic fillet/round suppressing for efficient automatic feature recognition. *Computer-Aided Design*, *34*(2), 109–123. https://doi.org/10.1016/S0010-4485(01)00056-2